Surface Waves Guided by Anisotropic Dielectric Materials in the Grating-Coupled Configuration

Kiran Mujeeb

Electronics

Quaid-i-Azam University, Islamabad, Pakistan.

A Thesis Submitted in Partial Fulfillment of the Requirements for the Degree

of

Doctor of Philosophy

in

Electronics

2022

Quaid- I- Azam University

Department of Electronics

Author's Declaration

I, **Kiran Mujeeb** hereby state that my PhD thesis titled " **Surface Waves Guided by**

Anisotropic Dielectric Materials in the Grating-Coupled Configuration" is my own

work and has not been submitted previously by me for taking degree from the **Department**

of Electronics, Quaid- i- Azam University or anywhere else in the country/world.

At any time, if my statement is found to be incorrect even after my graduation, the university
has the right to withdraw my PhD degree.

Kiran Mujeeb

Kiran Mujeeb

Date:

Quaid- I- Azam University

Department of Electronics

Plagiarism Undertaking

I, solemnly declare that the research work presented in this thesis titled
Surface Waves Guided by Anisotropic Dielectric Materials in the Grating-Coupled Configuration" is solely my research work with no significant contribution from any other person. Small contribution/help wherever taken has been fully acknowledged and that complete thesis has been written by me.

I understand the zero-tolerance policy of the HEC and Quaid- i- Azam University towards plagiarism. Therefore, I as an author of the above titled thesis, declare that no portion of my thesis has been plagiarized and any material used as reference is properly referred/cited.

I undertake that if I am found guilty of any formal plagiarism in the above titled thesis even after award of PhD degree, the university reserves the rights to withdraw/revoke my PhD degree and that HEC and the university has the right to publish my name on the HEC/university website on which names of students are placed who submitted plagiarized thesis.

Kiran Mujeeb

Date:

QUAID-I-AZAM UNIVERSITY
Department of Electronics

Certificate of Approval

This is to certify that the research work presented in this thesis, entitled "**Surface Waves Guided by Anisotropic Dielectric Materials in the Grating-Coupled Configuration.**" was conducted by **Ms. Kiran Mujeeb** under the supervision of **Dr. Muhammad Faryad** and under the co-supervision of **Prof. Dr. Qaisar A. Naqvi.** No part of this thesis has been submitted anywhere else for any other degree. This thesis is submitted to the **Department of Electronics, Quaid-i-Azam University** in partial fulfilment of the requirements for the degree of Doctor of Philosophy in Field of **Electronics,** Department of Electronics, Quaid-i-Azam University.

Student Name: **Ms. Kiran Mujeeb**   Signature: _Kiran Mujeeb_

Examination Committee:

A. Dr. Akhtar Hussain   Signature: _____
   Deputy Chief Manager
   P.O.Box 1702
   National Development Complex (NDC), Islamabad

B. Dr. Shakeel Ahmed   Signature: _____
   Deputy Director NESCOM, Islamabad.

C. Dr. Muhammad Faryad   Signature: _____
   Associate Professor & Supervisor
   SSE-Physics, Lahore University of Management
   Sciences (LUMS).

D. Prof. Dr. Qaisar A. Naqvi   Signature: _____
   Chairman & Co-supervisor
   Department of Electronics
   Quaid-i-Azam University, Islamabad

Supervisor Name: **Dr. Muhammad Faryad**   Signature: _____

Co-Supervisor Name: **Prof. Dr. Qaisar A. Naqvi**   Signature: _____
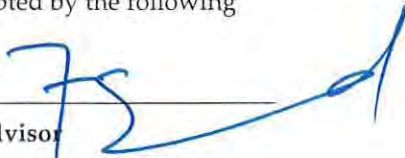
Name of Chairman: **Prof. Dr. Qaisar A. Naqvi**   Signature: _____

DEPARTMENT OF ELECTRONICS
QUAID-I-AZAM UNIVERSITY
ISLAMABAD

A thesis titled "Surface Waves Guided by Anisotropic Dielectric Materials in the Grating-Coupled Configuration" by Kiran Mujeeb in partial fulfilment of the requirements for the degree of Doctor of Philosophy, has been approved and accepted by the following

Advisor
Dr. Muhammad Faryad
Associate Professor
Department of Physics
Lahore University of Management Sciences (LUMS), Lahore
Pakistan

Co-Advisor
Dr. Qaisar Abbas Naqvi
Professor
Department of Electronics
Quaid-i-Azam University, Islamabad
Pakistan

Chairman
Dr. Qaisar Abbas Naqvi
Professor
Department of Electronics
Quaid-i-Azam University, Islamabad
Pakistan

Dedication

"ابا کے نام"

جنہوں نے ماں اور باپ، دونوں کا پیار دیا

"To my father"
Who also compensated mother′s love and care.

List of Publications

- K. Mujeeb, M. Faryad, J. V. Urbina, and A. Lakhtakia. Effect of orientation on excitation of surface plasmon-polariton waves guided by a columnar thin film deposited on a metal grating. Optical Engineering, 59(5): 055103, 2020; errata: 59(6): 069801, 2020.

- K. Mujeeb, M. Faryad, A. Lakhtakia, and J. V. Urbina. Theory of grating coupled excitation of Dyakonov surface waves. Optical Engineering, 59(7): 070503, 2020; errata: 60(6): 069801, 2021.

- K. Mujeeb, M. Faryad, A. Lakhtakia, and J. V. Urbina. Surface-plasmonic sensor using a columnar thin film in the grating-coupled configuration. Chinese Optics Letters, 19(8): 083601, 2021.

- K. Mujeeb, M. Faryad, A. Lakhtakia, and J. V. Urbina. Morphological effects on the excitation of surface waves in the grating-coupled configuration. Proceedings of the SPIE, 11802: 1180202, 2021.

- K. Mujeeb, M. Faryad, A. Lakhtakia, and J. V. Urbina. Grating-coupled excitation of high-phase-speed Dyakonov surface waves. Journal of the Optical Society of America B, 39(2): 474–480, 2022.

Acknowledgements

I am grateful to almighty Allah who enabled me to accomplish this dissertation. However, this project would not have been possible without the support of many people.

Many thanks to my primary supervisor, Dr. Muhammad Faryad, who guided me throughout this project. I am extremely grateful to Dr. Qaisar Abbas Naqvi (Co-Supervisor) who encouraged me to pursue PhD studies, took me on as a student and continued to have faith in me over the years.

I would like to express my gratitude to Dr. Akhlesh Lakhtakia, for his patience, guidance, and support. He read my numerous revisions and helped greatly during my stay in Pennsylvania State University. I have benefited greatly from his wealth of knowledge and meticulous proofreading. Thanks to the Pennsylvania State University, USA for hosting me as a guest researcher and giving me an opportunity to work with my favorite mentor, Dr. Akhlesh Lakhtakia. I am indebted also to Dr. Julio V. Urbina for his kind support before, during and after the trip. I would also like to acknowledge the Higher Education Commission (HEC) Pakistan for awarding me fellowship under IRSIP (International Research Support Initiative Program).

Special thanks to the Lahore University Management Sciences (LUMS), Pakistan for hosting me as a guest researcher, providing me on campus accommodation and financial support.

Tayyab H. Malik has been a great colleague and mentor, offering advice and encouragement with a perfect blend of insight and humor. Thank you, Mr. Malik, for constantly motivating me, for discussion and proofreading, for cracking jokes when things became too serious. I am proud of, and grateful for, my time working with you.

Lastly, my family deserves endless gratitude: my father for supporting me and believing in me. My brothers (Ahmed Nadeem and Muhammad Naeem) for their continuous financial and moral support, my brother (Muhammad Wasim) to encourage me to take career in STEM, and my sisters for their love and care. To my family, I owe everything, including this.

Abstract

Surface waves are electromagnetic waves that are guided by an interface of two dissimilar materials. If one of the two partnering materials is a metal, the surface waves are called surface-plasmon-polariton (SPP) waves. If both partnering materials are dielectric with at least one being anisotropic, the surface waves are called Dyakonov surface waves. In this thesis, the excitation of both the SPP waves and Dyakonov surface waves was studied when the partnering dielectric material is either uniaxial or biaxial. The biaxial material used here is a columnar thin film (CTF). CTFs are porous and have a columnar morphology with columns lying in a plane called the morphologically significant plane. The excitation of surface waves guided by a CTF deposited on either a one-dimensional metallic surface-relief grating, or a one-dimensional isotropic dielectric surface-relief grating was studied, when the grating plane, the plane of incidence, and the morphologically significant plane of the CTF are all different. The incident plane wave in this grating-coupled configuration can be either p- or s-polarized. The absorptances were plotted against the polar angle of incidence at a fixed value of the free-space wavelength and absorptance peaks were correlated with the solution of the dispersion equation of the underlying canonical boundary-value problem for the identification of surface waves. Both the p-polarized and s-polarized plane waves can excite surface waves, provided that either the plane of incidence and/or the morphologically significant plane of the CTF do not coincide with the grating plane. No, one, or multiple surface-wave excitations are possible, depending on the orientations of the grating plane and the morphologically significant plane with respect to the plane of incidence. The direction of propagation of surface wave thus excited may not wholly lie in the plane of incidence.

The excitation of SPP waves guided by a CTF deposited on a one-dimensional metallic surface-relief grating was investigated for sensing the refractive index of a fluid infiltrating that CTF. The Bruggemann homogenization formalism was used to determine the relative permittivity scalars of the CTF infiltrated by the fluid. Change in the refractive index of the fluid was sensed by determining the change in the incidence angle for which an SPP wave is excited on illumination by a p-polarized plane wave, when the plane of incidence is taken to coincide with the grating plane but not with the morphologically significant plane of the CTF. Multiple excitations of the same SPP wave were found to be possible depending on the

i

refractive index of the fluid, which could help increase the reliability of the results by sensing the same fluid with more than one excitations of the SPP wave.

Also, the excitation of the high-phase-speed Dyakonov surface waves guided by a surface-relief grating of a uniaxial dielectric material and an isotropic dielectric material was theoretically studied for illumination by p- and s-polarized plane waves. Both p- and s-polarized plane waves can excite the high-phase-speed Dyakonov surface waves. No, one, or multiple excitations of high-phase-speed Dyakonov surface waves are also possible, depending upon the choice of the partnering materials and the period of the surface-relief grating. Excitation of a high-phase-speed Dyakonov surface wave as a specular Floquet harmonic was also conjectured.

The purpose of this research was to study the propagation and excitation of the surface waves. It was found that (i) the excitation of surface waves is dependent on the orientation of the grating plane, morphologically significant plane of the CTF, and the plane of incidence; (ii) multiple surface waves can be excited for p-polarized and s-polarized incidence, depending on the orientation of different planes; (iii) for certain orientations of the grating plane, morphologically significant plane, and plane of incidence, no surface wave may be excited; (iv) no, one, or multiple excitations of high-phase-speed Dyakonov surface wave are possible with the phase speed higher than the phase speed of light in the partnering bulk materials; (v) the excitation of high-phase-speed Dyakonov surface waves as a specular Floquet harmonics is also possible; and (vi) multiple excitations of an SPP wave can be used for sensing the refractive index of a fluid infiltrating the CTF.

Contents

Bibliography

List of Symbols and Abbreviations

List of Symbols

$a_{\mathrm{s}}^{(n)}$	scalar amplitude of the s-polarized nth Floquet harmonic
$a_{\mathrm{p}}^{(n)}$	scalar amplitude of the p-polarized nth Floquet harmonic
A_{p}	absorptance for p-polarized incidence
A_{s}	absorptance for s-polarized incidence
$k_{\mathrm{x}}^{(n)}$	x-component of the wave vector of the nth Floquet harmonic
k_0	wavenumber in free space
L	period of surface-relief grating
L_1	width of the bump in the surface-relief grating
L_{g}	depth of the surface-relief grating
L_{m}	thickness of the metal film in grating-coupled configuration
L_{d}	thickness of the dielectric film in grating-coupled configuration
N_{d}	number of slices in the dielectric material
N_{m}	number of slices in the metal
N_{g}	number of slices in the grating region
$\pm N_{\mathrm{s}}$	ending and starting indexes in summations in RCWA
$[\underline{\underline{P}}]$	coefficient matrix of matrix ordinary differential equation
q	wavenumber of a surface wave in the canonical problem along the direction of propagation
$r_{\mathrm{p}}^{(n)}$	reflection amplitude of the p-polarized nth Floquet harmonic
$r_{\mathrm{s}}^{(n)}$	reflection amplitude of the s-polarized nth Floquet harmonics
$t_{\mathrm{p}}^{(n)}$	transmission amplitude of the p-polarized nth Floquet harmonic
$t_{\mathrm{s}}^{(n)}$	transmission amplitude of the s-polarized nth Floquet harmonic
$\hat{\mathbf{u}}_{\mathrm{x}}, \hat{\mathbf{u}}_{\mathrm{y}}, \hat{\mathbf{u}}_{\mathrm{z}}$	unit vectors along x, y and z axis
γ	angle between the grating plane and the morphologically significant plane of a CTF
ε_{d}	relative permittivity of dielectric material
ε_{m}	relative permittivity of metal
ε_0	permittivity of free space
$\varepsilon_{\mathrm{a}}, \varepsilon_{\mathrm{b}}, \varepsilon_{\mathrm{c}}$	relative permittivity scalars
$\underline{\underline{\varepsilon}}_{CTF}$	relative permittivity dyadic of the CTF
θ	incidence angle with the z axis

λ_0	wavelength of free space
μ_0	permeability of free space
χ_v	vapor incidence angle
ψ	angle between the incidence plane and the morphologically significant plane of a CTF
ω	angular frequency

List of Abbreviations

SPP	surface plasmon-polariton
CTF	columnar thin film
Re	real part
Im	imaginary part
RCWA	rigorous coupled-wave approach
TKR	Turbadar–Kretschmann–Raether
AED	angular existence domain
SPR	surface plasmon resonance
PVD	physical vapor deposition

List of Tables

List of Figures

Chapter 1

Introduction

Surface waves are electromagnetic waves guided by an interface of two dissimilar materials. The energy of a surface wave is confined to the vicinity of the interface. This localization property of the surface waves is exploited in designing extremely sensitive sensors of the change in the refractive index of the partnering material near the interface [1, 2]. The electromagnetic surface waves guided by the planar interface of a metal and a dielectric material are called surface plasmon-polariton (SPP) waves [3, 4]. The partnering dielectric material can be either isotropic [3, 4] or anisotropic [4, 5], and either homogeneous [3, 4] or nonhomogeneous [6]. Surface waves can also be supported by the interface of two dielectric materials if at least one of them is lossy or anisotropic. If both partnering materials are lossless dielectric, with at least one being anisotropic, the surface waves are called Dyakonov surface waves. The SPP waves decay along the direction of propagation, whereas Dyakonov surface waves propagate with negligible losses.

If one of the partnering materials is anisotropic, the propagation of surface waves can be engineered with greater flexibility than with isotropic partnering dielectric materials. Also, the presence of an anisotropic partnering dielectric material gives rise to direction-dependent properties of surface waves such as the angular existence domain (AED) in the interface plane. Although we have many naturally occurring anisotropic materials that are homogeneous continuums at macroscopic length scales, the degree of anisotropy of these natural anisotropic materials tends to be very small. Composite materials such as columnar thin films (CTFs) [3, 4] can be designed and manufactured artificially with specific anisotropy. This thesis concerns the excitation of surface waves with uniaxial and biaxial anisotropic materials. The biaxial material chosen for numerical results in this thesis was taken to be a CTF. The physical vapour deposition (PVD) of a bulk material results the formation of CTFs. During the PVD, a collimated vapor flux is directed at an angle χ_v to the substrate to grow a CTF with columns tilted at an angle $\chi \geq \chi_v$ [7]. The plane containing the tilt of the columns is called the morphologically significant plane of the CTF. CTFs of diverse materials can be grown over topologically

decorated substrates for a wide range of tilt angles [8–11].

The effect of the morphology of the CTF on the propagation of surface waves was considered in 2008 by Polo *et al.* [12] for a canonical boundary-value problem. In a canonical boundary-value problem, both partnering materials occupy half spaces. In this thesis, practical configuration is taken up to delineate the effect of morphology. The practical configuration chosen in this thesis is the grating-coupled configuration as opposed to the more common prism-coupled configuration. The main objective of this thesis is to study the effect of orientation of the morphologically significant plane of the CTF on the excitation of surface waves in the grating-coupled configuration. In the grating-coupled configuration, both partnering materials are of finite thickness but their interface is an undulating surface. The excitation of SPP waves at the CTF/metal interface in the grating-coupled configuration has been studied previously [13]. In that work, the grating plane was kept congruent with the morphologically significant plane of the CTF [13]. The SPP waves were found to be excited as a Floquet harmonic of different orders by p-polarized light incident from different directions. However, incident s-polarized light could not excite SPP waves.

In this thesis, the excitation of surface waves guided by a CTF deposited on one-dimensional surface-relief grating (metal and dielectric) was studied, provided that either the plane of incidence and/or the morphologically significant plane of the CTF do not coincide with the grating plane. The plane wave of either p- or s-polarization state was made incident on the CTF backed by a surface-relief grating. The absorptance was calculated using rigorous coupled-wave approach (RCWA) [14, 15]. The RCWA is very suitable for the grating-coupled configuration as it is based on Fourier series representation of permittivity dyadics and electromagnetic fields.

Electromagnetic fields of surface waves are strong on and in the proximity of the interface but decay away from the interface. The most widely studied type of the surface waves is the SPP wave. The energy density of an SPP wave far away from the interface is essentially negligible. Therefore, the properties of surface waves do not depend upon the thickness (after a certain thickness threshold has been achieved) of the partnering dielectric material. Surface waves are equipped with a localization property that makes them prolific for optical sensors. They are highly responsive to minor changes in the electromagnetic properties of the material near the interface. Keeping in view this fact, SPP-wave-based sensors are more proficient in detecting molecules in pollutants, analytes, and proteins that are in small concentrations in a given solution [1, 2, 16]. A CTF is used as the partnering dielectric material because of its porosity that can be used in sensing. The inter-columnar void regions of a CTF have to be infiltrated with the fluid to be sensed [17, 18].

Surface-wave propagation guided by the planar interface of a uniaxial dielectric material and anisotropic dielectric material was also studied in this thesis. The phase speed of the surface wave is inversely proportional to the real part of the wavenumber, and is usually smaller than the phase speed of a plane wave propagating in either of the two partnering materials.

However, the phase speed of the surface wave can be sometime higher than the phase speed of the plane wave in the bulk medium, especially when one of the partnering dielectric mediums is periodically nonhomogeneous [19]. High-phase-speed Dyakonov surface waves have also recently been found to exist at the interface of a dissipative uniaxial dielectric medium and a nondissipative isotropic dielectric medium [20]. In that work, both partnering mediums were taken to occupy adjacent half spaces, which is clearly a physically unrealizable configuration. The excitation of these high-phase-speed Dyakonov surface waves in grating-coupled configuration was also examined for air/uniaxial-dielectric interface, since this problem is a special case of the isotropic-dielectric/CTF interface for Dyakonov surface waves studied in this thesis.

In the remainder of this chapter, basic concepts and mathematical formulations for the canonical boundary-value problems are provided: surface waves and their types in Sec. 1.1, fabrication and applications of CTFs in Sec. 1.2, mathematical formulation of the canonical boundary-value problem of surface waves for metal/isotropic dielectric interface and metal/CTF interface in Sec. 1.3 and Sec. 1.4, respectively, different practical configurations used for the excitation of surface waves in Sec. 1.5, and applications of surface waves in Sec. 1.6. Finally, the objectives and plan of this thesis are presented in Sec. 1.7.

Throughout the thesis, $\exp(-i\omega t)$ dependency on time t is used with angular frequency ω and $i = \sqrt{-1}$. The free-space wavenumber is denoted by $k_0 = \omega\sqrt{\mu_0\varepsilon_0}$ and the free-space wavelength by $\lambda_0 = 2\pi/k_0$, where ε_0 is the permittivity and μ_0 is the permeability of free space. All vectors are in boldface, dyadics are underlined twice, and column vectors are in boldface and enclosed within square brackets. The unit vectors in the Cartesian coordinate system are identified by $\hat{\mathbf{u}}_x$, $\hat{\mathbf{u}}_y$ and $\hat{\mathbf{u}}_z$.

1.1 Surface Waves

More than a century ago, a special type of electromagnetic wave was explored by Uller [21] in 1903 and Zenneck in 1907 [22]. They explored the possibility of electromagnetic surface waves guided by the interface of air and water [21] and interface of air and ground [22], respectively, for radio transmission. An electromagnetic surface wave is localized to the interface and decays away from the interface, and propagates in a direction parallel to the interface. The surface waves are categorized on the basis of partnering materials. Usually, at least one partnering material is a dielectric material. Surface waves usually have phase speed lower than the speed of light in the bulk partnering materials. Therefore, these waves cannot be excited by impinging light on planar interface. Different practical configurations are used to excite surface waves. These practical configurations involve prisms [23, 24], waveguides [25, 26], or surface-relief gratings [3, 27]. Grating-coupled configuration is particularly attractive since direct illumination of the partnering dielectric material can be used to excite surface waves.

The surface waves investigated in this thesis are SPP waves and Dyakonov surface waves.

1.1.1 Surface Plasmon-Polariton (SPP) Waves

The non-radiative electromagnetic surface waves that propagate in a direction parallel to the interface guided by a negative permittivity material and a dielectric are said to be the SPP waves [3, 4]. The SPP waves have the longest history of theoretical development and applications [28, 29]. In general, the partnering material that contributes a negative real value of permittivity is considered to be a metal [3, 4]; however, the metal may be substituted by a semiconductor material [31], or an alloy [30]. The energy losses of electrons taking place at the metal film's surfaces [32] due to striking of electrons on metal film can be described in terms of electronic-plasma oscillations, the quantum of these oscillations is called the surface plasmon (SP). These surface plasmon propagate along the interface of metal and vacuum and can be treated classically as a surface plasmon (SP) wave. If the partnering vacuum is replaced by a dielectric material, then the quasi-particles are called surface plasmon-polaritons with a polariton component in the dielectric material and a plasmonic component in the metal. A plasmon is the quantum of plasma oscillations and polariton is the quantum of polarization in dielectric material [33].

The choice for the partnering material with positive real permittivity has a wide range due to the availability of many different types of dielectric materials. The partnering dielectric material can be either isotropic or anisotropic [3–5], and either homogeneous or nonhomogenous [3, 4, 6]. The choice of an anisotropic homogeneous dielectric partnering material and periodically nonhomogeneous dielectric material has been considered and studied by many researchers [2, 5, 34–40]. Excitation of multiple SPP waves is one of the remarkable properties of the SPP waves guided by the interface of metal and a periodically nonhomogeneous dielectric material [41, 42]. The behaviour of the SPP wave is explained graphically in Fig. 1.1 where the dielectric material is either isotropic or anisotropic, but homogeneous [3–5].

1.1.2 Dyakonov Surface Waves

A Dyakonov surface wave is guided by the planar interface of two homogeneous dielectric materials of which at least one is anisotropic. Theoretical predictions of this surface wave were made in the 1980s for one partnering material being isotropic and the other a uniaxial dielectric material [43], both being lossless. Since then, Dyakonov surface waves have been predicted for the planar interfaces of several combinations of dielectric materials [3, 44]: isotropic/biaxial [12, 45], uniaxial/uniaxial [46, 47], biaxial/biaxial [48], and gyrotropic/gyrotropic [49]. The Dyakonov surface wave was first observed in 2009 [50], and a confirmatory experimental result was reported in 2014 [51]. In these experiments, the interface of an isotropic dielectric material and a biaxial dielectric material was incorporated in a prism-coupled configuration [3, 23, 24]. The incident light made to enter a high-refractive-index coupling material on its interface with the isotropic dielectric material, this second interface being parallel to the guiding interface. When dissipation in both partnering materials is negligibly small, theory predicts
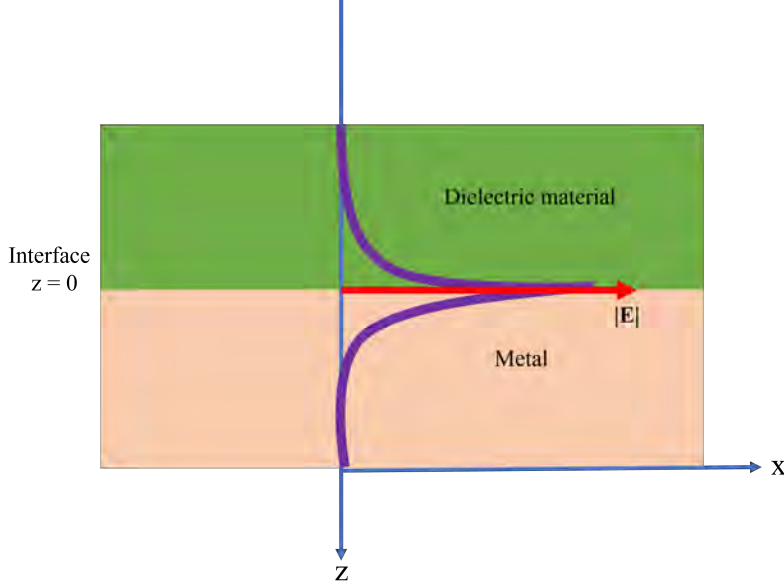
Figure 1.1: Schematic variation of the amplitude of the electric field phasor $|\mathbf{E}|$ of an SPP wave as a function of distance from the interface plane at $z = 0$.

and experiments have confirmed that Dyakonov surface waves can propagate in very narrow ranges of directions in the interface plane [44, 50, 52]. In other words, the AED of Dyakonov surface waves in the interface plane is tiny. Enlargement of AED is possible when at least one of the partnering dielectric materials is either active or dissipative [53–57]. Theory indicates that the combination of dissipative and active dielectric materials can support amplifying Dyakonov surface waves in certain directions and attenuating in other directions [58]. Parenthetically, the use of partnering materials with magnetic properties [59–61] can also deliver larger AED, but the focus of the research conducted here is on dielectric partnering materials. Whether dissipation in the partnering dielectric materials is significant or negligible, the characteristics of a Dyakonov surface wave are always strongly dependent upon the direction of propagation in the interface plane. This superdirectivity combined with sharp absorption peaks indicative of the excitation of these surface waves offer new possibilities for applications in light transmission, sensing, and waveguiding [62–66]. The behaviour of Dyakonov surface waves along the interface is given in Fig. 1.2.

Certain constraints have to be satisfied by the constitutive parameters of the two partnering materials for the existence of the Dyakonov surface wave; however, different set of constraints are obtained that allow the propagation of surface waves of a new type. The fields of the Dyakonov surface waves only decay exponentially in the anisotropic medium, whereas the fields of this novel form of surface waves decay as the product of a linear and an exponential function of the distance from the interface in the anisotropic medium. When the corresponding propagation matrix cannot be diagonalized, the behaviour of the surface wave fields is
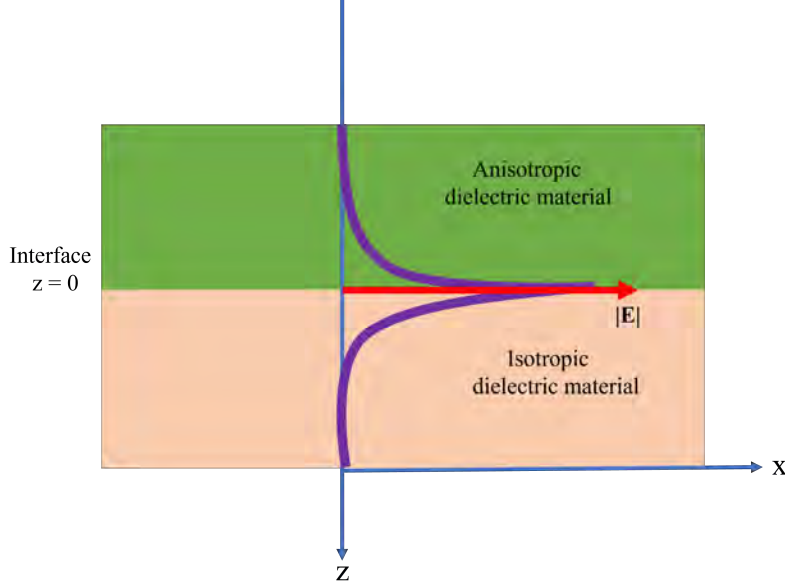
Figure 1.2: Schematic variation of the amplitude of the electric field phasor $|\mathbf{E}|$ of Dyakonov surface wave as a function of distance from the interface plane at $z = 0$.

very similar to the Voigt wave that propagates in an unbounded anisotropic medium [67, 68]. The amplitude of a Voigt wave is the product of a linear function and an exponential function of the propagation distance. Due to the similarity with Dyakonov surface waves and Voigt waves, these new type of surface waves are called Dyakonov—Voigt surface waves [69]. Dyakonov surface wave and Dyakonov–Voigt surface wave both are guided by the planar interface of non-dissipative dielectric mediums, one of which is anisotropic. But, unlike the Dyakonov surface waves, Dyakonov–Voigt surface waves propagate only in one direction in each quadrant of the interface plane [70]. Also the wavenumber of a Dyakonov–Voigt surface wave can be found analytically, but not of Dyakonov surface waves.

1.1.3 Other Types of Surface Waves

The surface waves guided by the interface of two dielectric materials, at least one of which is periodically nonhomogeneous in the direction normal to the interface are called Tamm waves [71]. These surface waves have been experimentally observed [72, 73] and can be exploited for optical biosensing [74]. Several *p*-polarized as well as *s*-polarized Tamm–wave modes can be obtained with proper choice of the two partnering dielectric materials [19, 75]. The partnering periodically nonhomogeneous dielectric material can be either continuously nonhomogeneous [19, 75], or it can be piecewise homogeneous [71–74, 76, 77].

A surface wave that is guided by the interface of two dielectric materials, of which at least one is both anisotropic and periodically nonhomogeneous in the direction normal to the inter-

face is called Dyakonov–Tamm wave [78–81]. Multiple Dyakonov–Tamm waves are routinely observed [79, 80, 82, 83]. The AED for Tamm–waves is 360° showing that these surface waves can propagate along any direction in the interface plane. The SPP waves decay along the direction of propagation, whereas Tamm waves and Dyakonov–Tamm waves propagate with negligible losses.
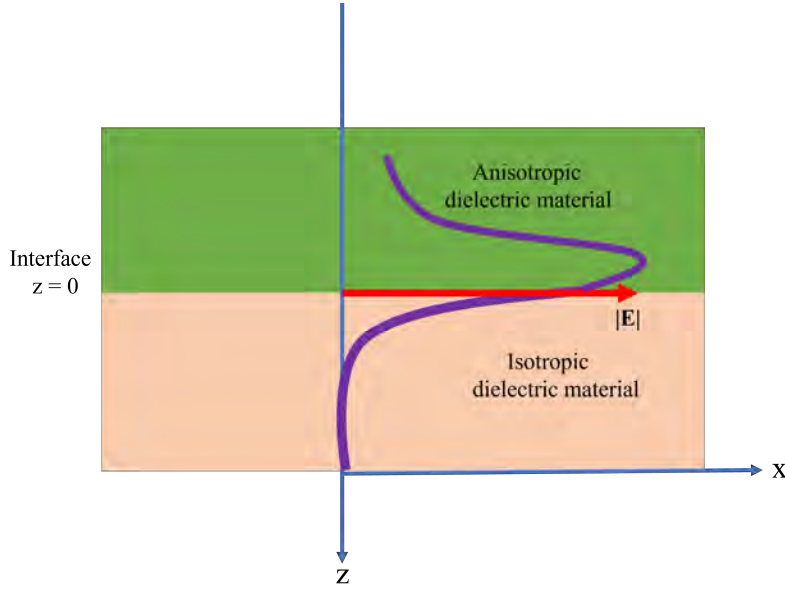
Figure 1.3: Schematic variation of the amplitude of the electric field phasor $|\mathbf{E}|$ of Dyakonov-voigt wave as a function of distance from the interface plane at $z = 0$.

1.2 Columnar Thin Films (CTFs)

A CTF is a biaxial material that can be utilised to excite SPP waves as well as Dyakonov surface waves. A CTF is fabricated when a well-collimated vapor flux is directed towards a planar substrate in a low-pressure chamber at a suitable temperature and pressure [84, 85]. In this process, the deposited material is organized in parallel columns as shown in Fig. 1.4, where χ is the angle between the axis of columns and the substrate plane and χ_{v} is the angle between the direction of the vapor flux and the substrate plane. By proper selection of χ_{v}, the columns can be tilted at any angle $\chi \in [20°, 90°]$ to the substrate plane. The value of angle χ depends on angle χ_{v}, lower values of χ_{v} are anticipated to lead lower values of χ. There are a few materials for which empirically proven relationships between the tilt angle χ and the vapour flux angle χ_{v} are available [86], however, these relationships are most likely dependent on the specific CTF production apparatus.
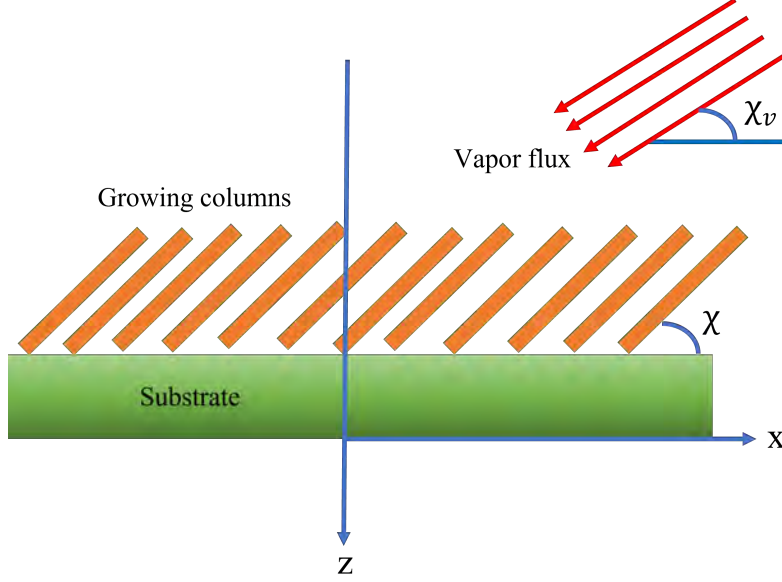
Figure 1.4: Schematic of the physical vapor deposition of the CTF. The xz plane is the morphologically significant plane of the CTF.

At optical frequencies, a CTF appears as a homogeneous continuum. The CTF can only be 10 μm thick, but for polymeric materials, the CTF might be several times thicker and its columnar diameter would be proportionally larger [87].

Columnar growth is inherently anisotropic. The relative permittivity dyadic of a CTF can be written as [13]

$$\underline{\underline{\varepsilon}}_{\mathrm{CTF}} = \underline{\underline{S}}_{\mathrm{y}} \cdot \left(\varepsilon_{\mathcal{A}_{\mathrm{a}}} \, \hat{\mathbf{u}}_{\mathrm{z}}\hat{\mathbf{u}}_{\mathrm{z}} + \varepsilon_{\mathcal{A}_{\mathrm{b}}} \, \hat{\mathbf{u}}_{\mathrm{x}}\hat{\mathbf{u}}_{\mathrm{x}} + \varepsilon_{\mathcal{A}_{\mathrm{c}}} \, \hat{\mathbf{u}}_{\mathrm{y}}\hat{\mathbf{u}}_{\mathrm{y}} \right) \cdot \underline{\underline{S}}_{\mathrm{y}}^{-1} \,, \tag{1.1}$$

where $\varepsilon_{\mathcal{A}_{\mathrm{a}}}$, $\varepsilon_{\mathcal{A}_{\mathrm{b}}}$, and $\varepsilon_{\mathcal{A}_{\mathrm{c}}}$ are three principal relative permittivity scalars. The dyadic

$$\underline{\underline{S}}_{\mathrm{y}} = (\hat{\mathbf{u}}_{\mathrm{x}}\hat{\mathbf{u}}_{\mathrm{x}} + \hat{\mathbf{u}}_{\mathrm{z}}\hat{\mathbf{u}}_{\mathrm{z}}) \cos\chi + (\hat{\mathbf{u}}_{\mathrm{z}}\hat{\mathbf{u}}_{\mathrm{x}} - \hat{\mathbf{u}}_{\mathrm{x}}\hat{\mathbf{u}}_{\mathrm{z}}) \sin\chi + \hat{\mathbf{u}}_{\mathrm{y}}\hat{\mathbf{u}}_{\mathrm{y}} \tag{1.2}$$

involves $\chi \in (0°, 90°]$. Decreasing χ_{v} from $90°$ increases the porosity and exacerbates anisotropy. Thus, a CTF's optical response characteristics are greatly influenced by the choice of χ_{v} during fabrication.

The ability to choose $\varepsilon_{\mathcal{A}_{\mathrm{a}}}$, $\varepsilon_{\mathcal{A}_{\mathrm{b}}}$, $\varepsilon_{\mathcal{A}_{\mathrm{c}}}$, and χ over a continuous range should allow a greater degree of flexibility in designing interfaces for surface wave propagation. This is one reason for choosing the CTF for this thesis. CTFs of diverse materials can be grown over topologically decorated substrates for a wide range of tilt angles [8–11], making the theoretical investigations amenable to experimental implementation. The porous structure of a CTF can be embedded with a material to alter its optical properties [88, 89]. The CTF growth process is amenable to the study of SPP waves and Dyakonov surface waves because the substrate can

be chosen as anisotropic dielectric material or a metal. As CTFs are porous, they can be used for optical sensing of infiltrant analytes [17, 18]. Macroscopically, CTFs are biaxial dielectric continuums with orthorhombic symmetry [88–91].

The CTF used in this thesis was taken to be made of tantalum oxide (Ta_2O_5) with [7, 86]

$$\left.\begin{aligned}
\varepsilon_{\mathcal{A}_a} &= [1.1961 + 1.5439\nu - 0.7719\nu^2]^2 \\
\varepsilon_{\mathcal{A}_b} &= [1.4600 + 1.0400\nu - 0.5200\nu^2]^2 \\
\varepsilon_{\mathcal{A}_c} &= [1.3532 + 1.2296\nu - 0.6148\nu^2]^2 \\
\chi &= \tan^{-1}(3.1056 \tan \chi_v)
\end{aligned}\right\}, \tag{1.3}$$

at $\lambda_0 = 633$ nm, where $\nu = 2\chi_v/\pi$ and χ_v is in radian. These expressions emerged from optical measurements on CTFs fabricated by directing a collimated vapor flux of Ta_2O_5 at an angle $\chi_v \in (20°, 90°)$ with respect to a substrate inside a low-pressure chamber designed to implement the electron-beam evaporation technique [86].

1.3 Canonical Boundary-Value Problem for Metal/Dielectric Interface
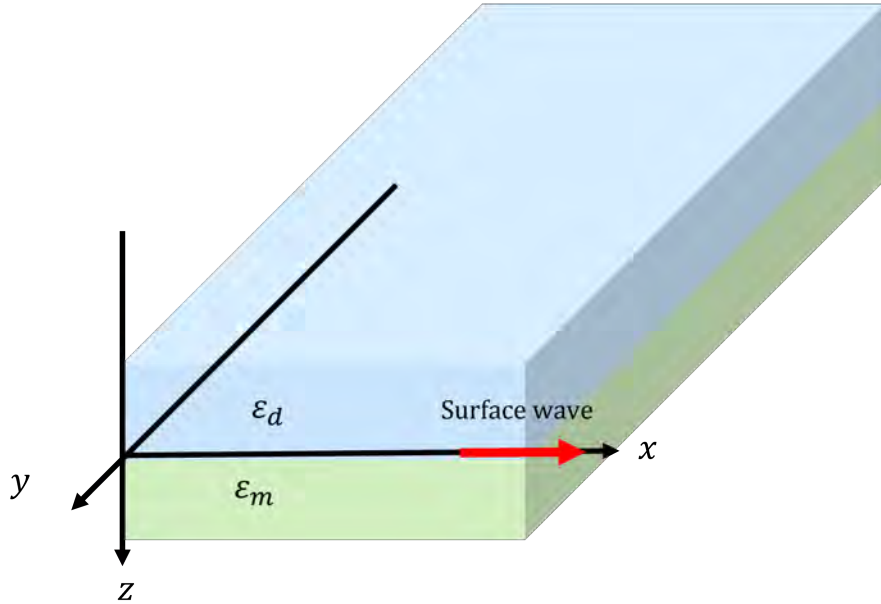
Figure 1.5: Schematic of the canonical boundary-value problem of two dissimilar materials with relative permittivities ε_m and ε_d.

In the canonical boundary-value problem, a planar interface is considered between two half spaces filled with two different materials. The only waves that could propagate are surface waves if we require the electromagnetic waves to have decaying amplitude away from the interface. Therefore, all existing solutions of this problem represent surface waves. Here, the interface of an isotropic homogeneous dielectric material and a metal is considered. The dielectric material is considered lossless with relative permittivity $\varepsilon_d = \varepsilon'_d$ and the metal is considered lossy with $\varepsilon_m = \varepsilon'_m + i\varepsilon''_m$. Here, the relative permittivity ε_m is complex-valued with non zero imaginary part ε''_m that shows the losses. Let the half space $z < 0$ be filled with the lossless dielectric material with relative permittivity ε_d and the half space $z > 0$ be filled with the metal. Both materials are non-magnetic. The source-free Maxwell curl postulates in the frequency domain are:

$$\left.\begin{aligned} \nabla \times \mathbf{H}(\mathbf{r}) + i\omega\varepsilon_0\varepsilon_d \mathbf{E}(\mathbf{r}) = 0 \\ \nabla \times \mathbf{E}(\mathbf{r}) - i\omega\mu_0 \mathbf{H}(\mathbf{r}) = 0 \end{aligned}\right\}, \qquad z < 0, \tag{1.4}$$

and

$$\left.\begin{aligned} \nabla \times \mathbf{H}(\mathbf{r}) + i\omega\varepsilon_0\varepsilon_m \mathbf{E}(\mathbf{r}) = 0 \\ \nabla \times \mathbf{E}(\mathbf{r}) - i\omega\mu_0 \mathbf{H}(\mathbf{r}) = 0 \end{aligned}\right\}, \qquad z > 0. \tag{1.5}$$

Without loss of generality, assume that the SPP wave propagates parallel to x axis in the xz plane. The Maxwell curl postulates give six differential equations in each half space that can be grouped into two sets of coupled equations as s- and p-polarized fields. For the p-polarization state, the Maxwell equations can be written as:

$$\left.\begin{aligned} \frac{\partial H_y}{\partial z} &= i\omega\varepsilon_0\varepsilon_d E_x \\ \frac{\partial E_x}{\partial z} - \frac{\partial E_z}{\partial x} &= i\omega\mu_0 H_y \\ \frac{\partial H_y}{\partial x} &= -i\omega\varepsilon_0\varepsilon_d E_z \end{aligned}\right\}, \qquad z < 0, \tag{1.6}$$

and

$$\left.\begin{aligned} \frac{\partial H_y}{\partial z} &= i\omega\varepsilon_0\varepsilon_m E_x \\ \frac{\partial E_x}{\partial z} - \frac{\partial E_z}{\partial x} &= i\omega\mu_0 H_y \\ \frac{\partial H_y}{\partial x} &= -i\omega\varepsilon_0\varepsilon_m E_z \end{aligned}\right\}, \qquad z > 0. \tag{1.7}$$

Similarly for the *s*-polarization state,

$$\left.\begin{aligned}\frac{\partial E_y}{\partial z} &= -i\omega\mu_0 H_x \\ \frac{\partial H_x}{\partial z} - \frac{\partial H_z}{\partial x} &= -i\omega\varepsilon_0\varepsilon_d E_y \\ \frac{\partial E_y}{\partial x} &= i\omega\mu_0 H_z\end{aligned}\right\}, \qquad z < 0, \tag{1.8}$$

and

$$\left.\begin{aligned}\frac{\partial E_y}{\partial z} &= -i\omega\mu_0 H_x \\ \frac{\partial H_x}{\partial z} - \frac{\partial H_z}{\partial x} &= -i\omega\varepsilon_0\varepsilon_m E_y \\ \frac{\partial E_y}{\partial x} &= i\omega\mu_0 H_z\end{aligned}\right\}, \qquad z > 0. \tag{1.9}$$

1.3.1 *s*-Polarization State

For the *s*-polarization state, the electric and magnetic field in the dielectric material can be written as:

$$\left.\begin{aligned}\mathbf{E}^{(d)} &= \hat{\mathbf{u}}_y E_0^d \exp\left[i(qx + k_z^{(d)}z)\right] \\ \mathbf{H}^{(d)} &= \frac{E_0^d}{\omega\mu_0}(q\hat{\mathbf{u}}_z - k_z^{(d)}\hat{\mathbf{u}}_x)\exp\left[i(qx + k_z^{(d)}z)\right]\end{aligned}\right\}, \qquad z < 0, \tag{1.10}$$

where

$$[q]^2 + \left[k_z^{(d)}\right]^2 = \varepsilon_d k_0^2. \tag{1.11}$$

The electric and magnetic fields on the metal side can be written as:

$$\left.\begin{aligned}\mathbf{E}^{(m)} &= \hat{\mathbf{u}}_y E_0^m \exp\left[i(qx + k_z^{(m)}z)\right] \\ \mathbf{H}^{(m)} &= \frac{E_0^m}{\omega\mu_0}(q\hat{\mathbf{u}}_z - k_z^{(m)}\hat{\mathbf{u}}_x)\exp\left[i(qx + k_z^{(m)}z)\right]\end{aligned}\right\}, \qquad z > 0, \tag{1.12}$$

where

$$q^2 + \left[k_z^{(m)}\right]^2 = \varepsilon_m k_0^2. \tag{1.13}$$

The decay of field away from the interface requires $\text{Im}[k_z^{(d)}] < 0$ and $\text{Im}[k_z^{(m)}] > 0$. The boundary conditions at the interface $z = 0$ require that

$$\hat{\mathbf{u}}_y \cdot \mathbf{E}^{(d)}(z = 0) = \hat{\mathbf{u}}_y \cdot \mathbf{E}^{(m)}(z = 0), \tag{1.14}$$

$$\hat{\mathbf{u}}_x \cdot \mathbf{H}^{(d)}(z = 0) = \hat{\mathbf{u}}_x \cdot \mathbf{H}^{(m)}(z = 0). \tag{1.15}$$

The boundary conditions for *s*-polarization state cannot be satisfied by surface waves when both partnering materials are homogeneous. So, *s*-polarized SPP waves do not exist.

1.3.2 p-Polarization State

For the p-polarization state, the electric and magnetic fields in the dielectric material can be written as:

$$\left.\begin{aligned}\mathbf{E}^{(\mathrm{d})} &= \frac{H_0^{\mathrm{d}}}{\omega\varepsilon_0\varepsilon_{\mathrm{d}}}(k_{\mathrm{z}}^{(\mathrm{d})}\hat{\mathbf{u}}_{\mathrm{x}} - q\hat{\mathbf{u}}_{\mathrm{z}})\exp\left[i(qx + k_{\mathrm{z}}^{(\mathrm{d})}z)\right]\\ \mathbf{H}^{(\mathrm{d})} &= \hat{\mathbf{u}}_{\mathrm{y}}H_0^{\mathrm{d}}\exp\left[i(qx + k_{\mathrm{z}}^{(\mathrm{d})}z)\right]\end{aligned}\right\}, \qquad z < 0, \tag{1.16}$$

and on the metal side the fields can be written as:

$$\left.\begin{aligned}\mathbf{E}^{(\mathrm{m})} &= \frac{H_0^{\mathrm{m}}}{\omega\varepsilon_0\varepsilon_{\mathrm{m}}}(k_{\mathrm{z}}^{(\mathrm{m})}\hat{\mathbf{u}}_{\mathrm{x}} - q\hat{\mathbf{u}}_{\mathrm{z}})\exp\left[i(qx + k_{\mathrm{z}}^{(\mathrm{m})}z)\right]\\ \mathbf{H}^{(\mathrm{m})} &= \hat{\mathbf{u}}_{\mathrm{y}}H_0^{\mathrm{m}}\exp\left[i(qx + k_{\mathrm{z}}^{(\mathrm{m})}z)\right]\end{aligned}\right\}, \qquad z > 0. \tag{1.17}$$

The decay of field away from the interface requires $\mathrm{Im}[k_{\mathrm{z}}^{(\mathrm{d})}] < 0$ and $\mathrm{Im}[k_{\mathrm{z}}^{(\mathrm{m})}] > 0$. The boundary conditions at the interface $z = 0$ require that

$$\hat{\mathbf{u}}_{\mathrm{x}} \cdot \mathbf{E}^{(\mathrm{d})}(z=0) = \hat{\mathbf{u}}_{\mathrm{x}} \cdot \mathbf{E}^{(\mathrm{m})}(z=0), \tag{1.18}$$

$$\hat{\mathbf{u}}_{\mathrm{y}} \cdot \mathbf{H}^{(\mathrm{d})}(z=0) = \hat{\mathbf{u}}_{\mathrm{y}} \cdot \mathbf{H}^{(\mathrm{m})}(z=0). \tag{1.19}$$

Using Eqs. (1.16)-(1.17) in Eqs. (1.18) and (1.19), the following equation emerges

$$\frac{k_{\mathrm{z}}^{(\mathrm{d})}}{\varepsilon_{\mathrm{d}}} = \frac{k_{\mathrm{z}}^{(\mathrm{m})}}{\varepsilon_{\mathrm{m}}}. \tag{1.20}$$

Substituting Eq. (1.20) in Eqs. (1.11) and (1.13), $k_{\mathrm{z}}^{(\mathrm{d})}$ and $k_{\mathrm{z}}^{(\mathrm{m})}$ can be eliminated and the surface wavenumber q is obtained as

$$q = k_0\sqrt{\frac{\varepsilon_{\mathrm{d}}\varepsilon_{\mathrm{m}}}{\varepsilon_{\mathrm{d}} + \varepsilon_{\mathrm{m}}}}. \tag{1.21}$$

After finding q, the z component of the surface wave vector can easily be found as

$$[k_{\mathrm{z}}^{(\mathrm{d})}]^2 = \varepsilon_{\mathrm{d}}k_0^2 - q^2 = \frac{\varepsilon_{\mathrm{d}}^2 k_0^2}{\varepsilon_{\mathrm{m}} + \varepsilon_{\mathrm{d}}}, \qquad z < 0, \tag{1.22}$$

$$[k_{\mathrm{z}}^{(\mathrm{m})}]^2 = \varepsilon_{\mathrm{d}}k_0^2 - q^2 = \frac{\varepsilon_{\mathrm{m}}^2 k_0^2}{\varepsilon_{\mathrm{m}} + \varepsilon_{\mathrm{d}}}, \qquad z > 0. \tag{1.23}$$

1.4 Canonical Boundary-Value Problem for Isotropic Material/CTF Interface

To confirm the excitation of surface waves, the wavenumbers of the surface wave excited in the grating-coupled configuration should be matched with the wavenumber of the canonical boundary-value problem. Therefore, the underlying canonical boundary-value problem for

isotropic dielectric/CTF interface has been presented for the planar interface between a CTF and an isotropic material. When the isotropic partnering material is a metal, the surface waves are called SPP waves; when isotropic partnering material is a dielectric material, the surface waves are called Dyakonov surface waves. The mathematical formulation for the canonical boundary-value problem given here is used in next chapters for the confirmation of surface wave in the grating-coupled configurations.

Let me now consider the schematic of the boundary-value problem given in Fig. 1.6. The
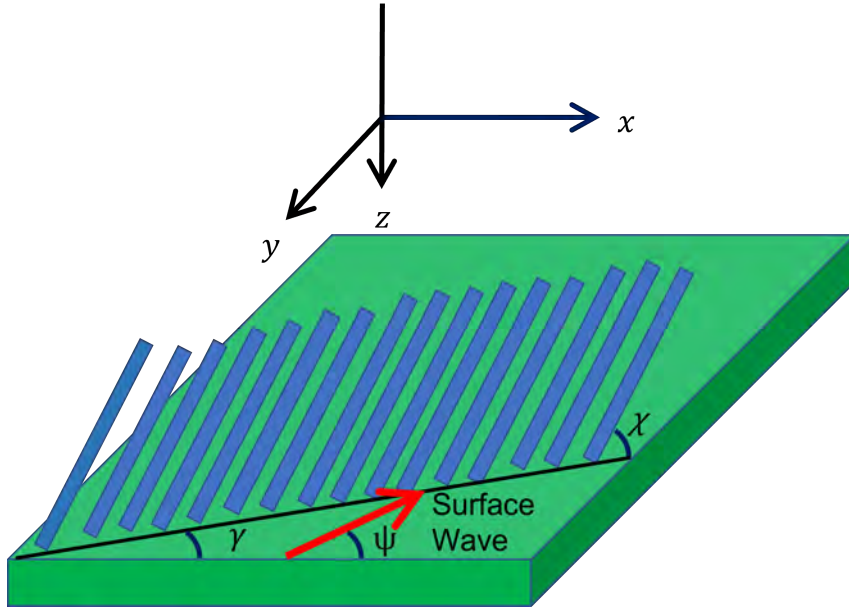
Figure 1.6: Schematic of the boundary-value problem solved for the canonical problem. The CTF is symbolically represented by a single row of columns.

region $z > 0$ is occupied by an isotropic material $\mathcal{B}$ (could be a metal) with refractive index $n_\mathcal{B} = \sqrt{\varepsilon_\mathcal{B}}$ and the region $z \leq 0$ is occupied by an anisotropic medium $\mathcal{A}$ with relative permittivity dyadic [13]

$$\underline{\underline{\varepsilon}}_{CTF} = \underline{\underline{S}}_z(\gamma) \cdot \underline{\underline{S}}_y \cdot \left(\varepsilon_{\mathcal{A}_a} \, \hat{\mathbf{u}}_z \hat{\mathbf{u}}_z + \varepsilon_{\mathcal{A}_b} \, \hat{\mathbf{u}}_x \hat{\mathbf{u}}_x + \varepsilon_{\mathcal{A}_c} \, \hat{\mathbf{u}}_y \hat{\mathbf{u}}_y \right) \cdot \underline{\underline{S}}_y^{-1} \cdot \underline{\underline{S}}_z^{-1}(\gamma), \qquad (1.24)$$

where $\varepsilon_{\mathcal{A}_a}$, $\varepsilon_{\mathcal{A}_b}$, and $\varepsilon_{\mathcal{A}_c}$ are the principal relative permittivity scalars, the dyadic $\underline{\underline{S}}_y$ is given in Eq. (1.2) and the dyadic

$$\underline{\underline{S}}_z = (\hat{\mathbf{u}}_x \hat{\mathbf{u}}_x + \hat{\mathbf{u}}_y \hat{\mathbf{u}}_y) \cos \gamma + (\hat{\mathbf{u}}_y \hat{\mathbf{u}}_x - \hat{\mathbf{u}}_x \hat{\mathbf{u}}_y) \sin \gamma + \hat{\mathbf{u}}_z \hat{\mathbf{u}}_z \qquad (1.25)$$

involves the angle $\gamma \in [0°, 360°)$ between the grating plane and the morphologically significant plane, the latter plane being jointly defined by the unit vectors $\underline{\underline{S}}_z \cdot \hat{\mathbf{u}}_x$ and $\hat{\mathbf{u}}_z$. Let the surface wave propagates parallel to $\hat{\mathbf{u}}_x \cos \psi + \hat{\mathbf{u}}_y \sin \psi$ in the interface plane $z = 0$. The elec-

tromagnetic field phasors can be written for all z as

$$\mathbf{E}(\mathbf{r}) = [E_x(z)\hat{\mathbf{u}}_x + E_y(z)\hat{\mathbf{u}}_y + E_z(z)\hat{\mathbf{u}}_z]\exp[iq(x\cos\psi + y\sin\psi)], \tag{1.26}$$

$$\mathbf{H}(\mathbf{r}) = [H_x(z)\hat{\mathbf{u}}_x + H_y(z)\hat{\mathbf{u}}_y + H_z(z)\hat{\mathbf{u}}_z]\exp[iq(x\cos\psi + y\sin\psi)]. \tag{1.27}$$

The source-free, frequency-domain Maxwell curl postulates are

$$\left.\begin{array}{r} \nabla \times \mathbf{H}(\mathbf{r}) + i\omega\varepsilon_0\underline{\underline{\varepsilon}}_{CTF} \cdot \mathbf{E}(\mathbf{r}) = \mathbf{0} \\ \nabla \times \mathbf{E}(\mathbf{r}) - i\omega\mu_0\mathbf{H}(\mathbf{r}) = \mathbf{0} \end{array}\right\}, \qquad z < 0, \tag{1.28}$$

and

$$\left.\begin{array}{r} \nabla \times \mathbf{H}(\mathbf{r}) + i\omega\varepsilon_0\varepsilon_{\mathcal{B}}\mathbf{E}(\mathbf{r}) = \mathbf{0} \\ \nabla \times \mathbf{E}(\mathbf{r}) - i\omega\mu_0\mathbf{H}(\mathbf{r}) = \mathbf{0} \end{array}\right\}, \qquad z > 0. \tag{1.29}$$

The substitution of Eqs. (1.26) and (1.27) in Eqs. (1.28) and (1.29) results in a set four first-order differential equations and two algebraic equations. The four differential equations can be rearranged in a matrix equation as

$$\frac{d}{dz}[\mathbf{f}(z)] = i[\underline{\underline{P}}_{\mathcal{A}}(q,\psi)] \cdot [\mathbf{f}(z)], \qquad z < 0, \tag{1.30}$$

$$\frac{d}{dz}[\mathbf{f}(z)] = i[\underline{\underline{P}}_{\mathcal{B}}(q,\psi)] \cdot [\mathbf{f}(z)], \qquad z > 0, \tag{1.31}$$

where $[\mathbf{f}(z)] = [E_x(z), E_y(z), H_x(z), H_y(z)]^T$ is a column vector, $[\underline{\underline{P}}_{\mathcal{A}}(q,\psi)]$ and $[\underline{\underline{P}}_{\mathcal{B}}(q,\psi)]$ are given as

$$[\underline{\underline{P}}_{\mathcal{A}}(q,\psi)] = \begin{bmatrix} P_{11} & P_{12} & P_{13} & P_{14} \\ P_{21} & P_{22} & P_{23} & P_{24} \\ P_{31} & P_{32} & P_{33} & P_{34} \\ P_{41} & P_{42} & P_{43} & P_{44} \end{bmatrix}, \tag{1.32}$$

where

$$P_{11} = q \cos \psi \frac{(\varepsilon_{\mathcal{A}_a} - \varepsilon_{\mathcal{A}_b}) \cos \gamma \cos \chi \sin \chi}{\varepsilon_{\mathcal{A}_a} \cos^2 \chi + \varepsilon_{\mathcal{A}_b} \sin^2 \chi}, \tag{1.33}$$

$$P_{12} = q \cos \psi \frac{(\varepsilon_{\mathcal{A}_a} - \varepsilon_{\mathcal{A}_b}) \sin \gamma \cos \chi \sin \chi}{\varepsilon_{\mathcal{A}_a} \cos^2 \chi + \varepsilon_{\mathcal{A}_b} \sin^2 \chi}, \tag{1.34}$$

$$P_{13} = \frac{q^2 \cos \psi \sin \psi}{\omega \varepsilon_0 (\varepsilon_{\mathcal{A}_a} \cos^2 \chi + \varepsilon_{\mathcal{A}_b} \sin^2 \chi)}, \tag{1.35}$$

$$P_{14} = \omega \mu_0 - \frac{q^2 \cos^2 \psi}{\omega \varepsilon_0 (\varepsilon_{\mathcal{A}_a} \cos^2 \chi + \varepsilon_{\mathcal{A}_b} \sin^2 \chi)} \tag{1.36}$$

$$P_{21} = q \sin \psi \frac{(\varepsilon_{\mathcal{A}_a} - \varepsilon_{\mathcal{A}_b}) \cos \gamma \cos \chi \sin \chi}{\varepsilon_{\mathcal{A}_a} \cos^2 \chi + \varepsilon_{\mathcal{A}_b} \sin^2 \chi}, \tag{1.37}$$

$$P_{22} = q \sin \psi \frac{(\varepsilon_{\mathcal{A}_a} - \varepsilon_{\mathcal{A}_b}) \sin \gamma \cos \chi \sin \chi}{\varepsilon_{\mathcal{A}_a} \cos^2 \chi + \varepsilon_{\mathcal{A}_b} \sin^2 \chi}, \tag{1.38}$$

$$P_{23} = -\omega \mu_0 + \frac{q^2 \sin^2 \psi}{\omega \varepsilon_0 (\varepsilon_{\mathcal{A}_a} \cos^2 \chi + \varepsilon_{\mathcal{A}_b} \sin^2 \chi)}, \tag{1.39}$$

$$P_{24} = -\frac{q^2 \cos \psi \sin \psi}{\omega \varepsilon_0 (\varepsilon_{\mathcal{A}_a} \cos^2 \chi + \varepsilon_{\mathcal{A}_b} \sin^2 \chi)}, \tag{1.40}$$

$$P_{31} = \frac{\omega \varepsilon_0 \cos \gamma \left[\varepsilon_{\mathcal{A}_b} \varepsilon_{\mathcal{A}_c} + \varepsilon_{\mathcal{A}_a} (\varepsilon_{\mathcal{A}_c} - 2 \varepsilon_{\mathcal{A}_b}) + (\varepsilon_{\mathcal{A}_a} - \varepsilon_{\mathcal{A}_b}) \varepsilon_{\mathcal{A}_c} \cos 2\chi \right] \sin \gamma}{2 (\varepsilon_{\mathcal{A}_a} \cos^2 \chi + \varepsilon_{\mathcal{A}_b} \sin^2 \chi)} \tag{1.41}$$

$$- \frac{q^2 \cos \psi \sin \psi}{\omega \mu_0},$$

$$P_{32} = -\omega \varepsilon_0 \varepsilon_{\mathcal{A}_c} \cos^2 \gamma + \frac{q^2 \cos^2 \psi}{\omega \mu_0} - \omega \varepsilon_0 \sin^2 \gamma (\varepsilon_{\mathcal{A}_b} \cos^2 \chi + \varepsilon_{\mathcal{A}_a} \sin^2 \chi) \tag{1.42}$$

$$+ \frac{\omega \varepsilon_0 (\varepsilon_{\mathcal{A}_a} - \varepsilon_{\mathcal{A}_b})^2 \cos^2 \chi \sin^2 \gamma \sin^2 \chi}{\varepsilon_{\mathcal{A}_a} \cos^2 \chi + \varepsilon_{\mathcal{A}_b} \sin^2 \chi},$$

$$P_{33} = q \sin \psi \frac{(\varepsilon_{\mathcal{A}_a} - \varepsilon_{\mathcal{A}_b}) \sin \gamma \cos \chi \sin \chi}{\varepsilon_{\mathcal{A}_a} \cos^2 \chi + \varepsilon_{\mathcal{A}_b} \sin^2 \chi}, \tag{1.43}$$

$$P_{34} = q \cos \psi \frac{(\varepsilon_{\mathcal{A}_b} - \varepsilon_{\mathcal{A}_a}) \sin \gamma \cos \chi \sin \chi}{\varepsilon_{\mathcal{A}_a} \cos^2 \chi + \varepsilon_{\mathcal{A}_b} \sin^2 \chi}, \tag{1.44}$$

$$P_{41} = \omega \varepsilon_0 \varepsilon_{\mathcal{A}_c} \sin^2 \gamma + \frac{\omega \varepsilon_0 \varepsilon_{\mathcal{A}_a} \varepsilon_{\mathcal{A}_b} \cos^2 \gamma}{\varepsilon_{\mathcal{A}_a} \cos^2 \chi + \varepsilon_{\mathcal{A}_b} \sin^2 \chi} - \frac{q^2 \sin^2 \psi}{\omega \mu_0}, \tag{1.45}$$

$$P_{42} = \frac{\omega \varepsilon_0 \cos \gamma \left[-\varepsilon_{\mathcal{A}_b} \varepsilon_{\mathcal{A}_c} - \varepsilon_{\mathcal{A}_a} (\varepsilon_{\mathcal{A}_c} - 2\varepsilon_{\mathcal{A}_b}) - (\varepsilon_{\mathcal{A}_a} - \varepsilon_{\mathcal{A}_b}) \varepsilon_{\mathcal{A}_c} \cos 2\chi \right] \sin \gamma}{2(\varepsilon_{\mathcal{A}_a} \cos^2 \chi + \varepsilon_{\mathcal{A}_b} \sin^2 \chi)} \tag{1.46}$$

$$+ \frac{q^2 \cos \psi \sin \psi}{\omega \mu_0},$$

$$P_{43} = q \sin \psi \frac{(\varepsilon_{\mathcal{A}_b} - \varepsilon_{\mathcal{A}_a}) \cos \gamma \sin \chi \cos \chi}{\varepsilon_{\mathcal{A}_a} \cos^2 \chi + \varepsilon_{\mathcal{A}_b} \sin^2 \chi}, \tag{1.47}$$

$$P_{44} = q \cos \psi \frac{(\varepsilon_{\mathcal{A}_a} - \varepsilon_{\mathcal{A}_b}) \cos \gamma \cos \chi \sin \chi}{\varepsilon_{\mathcal{A}_a} \cos^2 \chi + \varepsilon_{\mathcal{A}_b} \sin^2 \chi}. \tag{1.48}$$

Similarly, the 4×4 matrix $[\underline{\underline{P}}_{\mathcal{B}}(q, \psi)]$ is

$$[\underline{\underline{P}}_{\mathcal{B}}(q, \psi)] = \begin{bmatrix} 0 & 0 & \frac{q^2 \sin 2\psi}{2\omega \varepsilon_0 \varepsilon_{\mathcal{B}}} & \frac{k_0^2 \varepsilon_{\mathcal{B}} - q^2 \cos^2 \psi}{\omega \varepsilon_0 \varepsilon_{\mathcal{B}}} \\ 0 & 0 & \frac{-k_0^2 \varepsilon_{\mathcal{B}} + q^2 \cos^2 \psi}{\omega \varepsilon_0 \varepsilon_{\mathcal{B}}} & -\frac{q^2 \sin 2\psi}{2\omega \varepsilon_0 \varepsilon_{\mathcal{B}}} \\ -\frac{q^2 \sin 2\psi}{2\omega \mu_0} & \frac{-k_0^2 \varepsilon_{\mathcal{B}} + q^2 \cos^2 \psi}{\omega \mu_0} & 0 & 0 \\ \frac{k_0^2 \varepsilon_{\mathcal{B}} - q^2 \cos^2 \psi}{\omega \mu_0} & \frac{q^2 \sin 2\psi}{2\omega \mu_0} & 0 & 0 \end{bmatrix}. \tag{1.49}$$

The matrix $[\underline{\underline{P}}_{\mathcal{B}}(q, \psi)]$ has two eigenvalues

$$\alpha_{\mathcal{B}} = \pm i \sqrt{q^2 - k_0^2 \varepsilon_{\mathcal{B}}}. \tag{1.50}$$

In Eq. (1.50), the $\text{Im}\{\alpha_{\mathcal{B}}\} > 0$ is selected for surface-wave propagation, keeping in mind that the electromagnetic field of surface wave should decay away from the interface. The corresponding eigenvectors of $[\underline{\underline{P}}_{\mathcal{B}}(q, \psi)]$ are

$$[\boldsymbol{\nu}_{\mathcal{B}1}] = \begin{bmatrix} \frac{k_0^2 \varepsilon_{\mathcal{B}} - q^2 \cos^2 \psi}{k_0^2 \varepsilon_{\mathcal{B}}} \\ -\frac{q^2 \cos \psi \sin \psi}{k_0^2 \varepsilon_{\mathcal{B}}} \\ 0 \\ \frac{\alpha_{\mathcal{B}}}{\omega \mu_0} \end{bmatrix}, \tag{1.51}$$

$$[\boldsymbol{\nu}_{\mathcal{B}2}] = \begin{bmatrix} \frac{q^2 \cos \psi \sin \psi}{k_0^2 \varepsilon_{\mathcal{B}}} \\ \frac{q^2 \cos^2 \psi - k_0^2 \varepsilon_{\mathcal{B}}}{k_0^2 \varepsilon_{\mathcal{B}}} \\ \frac{\alpha_{\mathcal{B}}}{\omega \mu_0} \\ 0 \end{bmatrix}. \tag{1.52}$$

The solutions of the Eqs. (1.30) and (1.31) for the decaying fields as $z \longrightarrow \pm\infty$ in term of

unknowns $\mathcal{G}_{\mathcal{A}1,\mathcal{A}2}$ and $\mathcal{G}_{\mathcal{B}1,\mathcal{B}2}$ are:

$$\left[\mathbf{f}(z)\right] = \mathcal{G}_{\mathcal{A}1}[\boldsymbol{v}_{\mathcal{A}1}]\exp(i\alpha_{\mathcal{A}1}z) + \mathcal{G}_{\mathcal{A}2}[\boldsymbol{v}_{\mathcal{A}2}]\exp(i\alpha_{\mathcal{A}2}z), \qquad z < 0, \tag{1.53}$$

$$\left[\mathbf{f}(z)\right] = \left(\mathcal{G}_{\mathcal{B}1}[\boldsymbol{v}_{\mathcal{B}1}] + \mathcal{G}_{\mathcal{B}2}[\boldsymbol{v}_{\mathcal{B}2}]\right)\exp(i\alpha_{\mathcal{B}}z), \qquad z > 0, \tag{1.54}$$

where $[\boldsymbol{v}_{\mathcal{A}1}]$ and $[\boldsymbol{v}_{\mathcal{A}2}]$ are the eigenvectors, and $\alpha_{\mathcal{A}1}$ and $\alpha_{\mathcal{A}2}$ are the corresponding eigenvalues of $[\underline{\underline{P}}_{\mathcal{A}}(q,\psi)]$. In order for solution to correspond to the electromagnetic surface waves, the inequalities $\text{Im}\{\alpha_{\mathcal{A}1,2}\} < 0$ must be satisfied. Coefficients $\mathcal{G}_{\mathcal{A}1}$ and $\mathcal{G}_{\mathcal{A}2}$ are determined by applying the boundary conditions at $z = 0$. Four conditions are imposed by the continuity of tangential components of the electric and magnetic field phasors across the interface at $z = 0$. These conditions are compactly written as:

$$\left[\mathbf{f}(0^-)\right] = \left[\mathbf{f}(0^+)\right], \tag{1.55}$$

with

$$\left[\mathbf{f}(0^-)\right] = \begin{bmatrix} \boldsymbol{v}_{\mathcal{A}1} & \boldsymbol{v}_{\mathcal{A}2} \end{bmatrix} \cdot \begin{bmatrix} \mathcal{G}_{\mathcal{A}1} \\ \mathcal{G}_{\mathcal{A}2} \end{bmatrix}, \tag{1.56}$$

and

$$\left[\mathbf{f}(0^+)\right] = \begin{bmatrix} \boldsymbol{v}_{\mathcal{B}1} & \boldsymbol{v}_{\mathcal{B}2} \end{bmatrix} \cdot \begin{bmatrix} \mathcal{G}_{\mathcal{B}1} \\ \mathcal{G}_{\mathcal{B}2} \end{bmatrix}. \tag{1.57}$$

Using Eqs. (1.56) and (1.57) in Eq. (1.55) results in

$$[\underline{\underline{M}}(q,\psi)] \cdot \begin{bmatrix} \mathcal{G}_{\mathcal{A}1} \\ \mathcal{G}_{\mathcal{A}2} \\ \mathcal{G}_{\mathcal{B}1} \\ \mathcal{G}_{\mathcal{B}2} \end{bmatrix} = \begin{bmatrix} 0 \\ 0 \\ 0 \\ 0 \end{bmatrix}. \tag{1.58}$$

The matrix $[\underline{\underline{M}}(q,\psi)]$ has four column vectors. Two columns are eigenvectors of a 4×4 matrix $[\underline{\underline{P}}_{\mathcal{A}}(q,\psi)]$ and the remaining two are eigenvectors of matrix $[\underline{\underline{P}}_{\mathcal{B}}(q,\psi)]$. The matrix $[\underline{\underline{M}}(q,\psi)]$ must be singular for surface-wave propagation i.e.,

$$\det\{[\underline{\underline{M}}(q,\psi)]\} = 0. \tag{1.59}$$

Equation (1.59) is the dispersion equation for the electromagnetic surface-wave propagation that can be solved numerically for surface wave number q. The most practical way to solve Eq. (1.59) is to use the Newton–Raphson technique. Since the function

$$\zeta(q,\psi) = \det\{[\underline{\underline{M}}(q,\psi)]\}. \tag{1.60}$$

Although $\zeta(q,\psi)$ cannot be determined analytically, its derivative with respect to q can be

calculated by using the forward difference formula

$$F(q, \psi) = \frac{\zeta(q + \delta q, \psi) - \zeta(q, \psi)}{\delta q},$$ (1.61)

where δ is a real number and magnitude of $\delta \ll 1$. Then,

$$q \leftarrow q - \frac{\zeta(q, \psi)}{F(q, \psi)}.$$ (1.62)

Equation (1.62) can be quantitatively solved using the initial guess for the solution of Eq. (1.59). After finding q from Eq. (1.59) for a specific ψ and replacing that q by a numerical value in Eq. (1.58), the field phasors corresponding to a particular solution can be determined. Then, Eq. (1.58) has three algebraic equations that are linearly independent and can only be solved for determining the three coefficients. Therefore, $\mathcal{G}_{\mathcal{A}1}$ or $\mathcal{G}_{\mathcal{A}2}$ should be set equal to unity, and by the solution of any three of the four algebraic equations, the remaining three coefficients are then found.

1.5 Excitation of Surface Waves

Excitation of a surface wave with $\text{Re}(q) > k_0$ is not possible by direct coupling of the beam of light due to the mismatch in wavelengths of the surface wave $2\pi/\text{Re}(q)$ and the wavelength of plane waves in the bulk partnering materials. This is due to the fact that surface waves usually have phase speed $\omega/\text{Re}(q)$ smaller than the phase speed in the bulk partnering materials. Therefore, some coupling configurations have to be used to excite surface wave. These configurations include prism-coupled configurations, grating-coupled configuration, and waveguide-coupled configuration. These configurations are suitable for different applications.

1.5.1 Prism-Coupled Configurations

In 1959, Turbadar [92] used a thin aluminium film deposited on a glass prism to study the reflectance of a p-polarized plane wave and concluded that the reflectance of the p-polarized plane wave exhibited a sharp dip where the magnitude of dip in the reflectance could be controlled by changing the thickness of the metal film and could be made null by a proper choice of the metal film thickness [93]. Turbadar [92, 93] observed the dependence of the reflectance on the thickness of the metallic film but did not connect the reflectance dip with the excitation of SPP waves. This connection was made by Otto in 1969 [23]. Their configuration is known as Turbadar–Otto configuration and is shown in Fig. 1.7. Kretschmann and Raether [24] proposed the excitation of SPP waves in an inverted geometry. This is called Turbadar-Kretschmann-Rather (TKR) configurations and is shown in Fig. 1.8. Both configurations are considered as practical methods to excite the SPP waves using evanescent waves generated by

total internal reflection. Energy from the evanescent wave is absorbed causing a reduction in the intensity of reflected light in a process known as frustrated total reflection or attenuated total reflection [94].

1.5.1.1 Turbadar–Otto Configuration
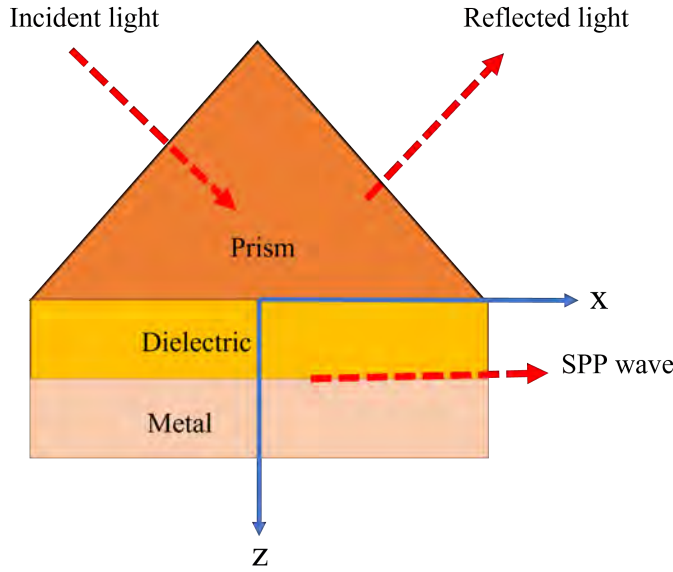
Figure 1.7: Schematic for the Turbadar–Otto configuration.

In the Turbadar–Otto configuration, a thin metal film having refractive index $n_\mathrm{m} = \sqrt{\varepsilon_\mathrm{m}}$ with the partnering dielectric material with refractive index $n_\mathrm{d} = \sqrt{\varepsilon_\mathrm{d}}$ is deposited on the base of a prism made of refractive index n_p [1, 23], as shown in Fig. 1.7. The partnering dielectric material with refractive index n_d is selected that satisfies the condition $n_\mathrm{p} > n_\mathrm{d}$. When light is incident on the prism/dielectric interface at an angle greater than the critical angle for the total internal reflection, an evanescent wave appears in the partnering dielectric material. If the dielectric film is sufficiently thin, an SPP wave is guided by the metal/dielectric interface when the component of the wavenumber parallel to the interface is same as $\mathrm{Re}(q)$. The Turbadar–Otto configuration can be used to excite Dyakonov surface waves by replacing the metal thin film by an isotropic or anisotropic dielectric material just like Dyakonov–Tamm waves [95].

1.5.1.2 Turbadar–Kretschmann–Raether (TKR) Configuration

If the metal and dielectric thin films in the Turbadar–Otto configuration are interchanged, the new configuration is known as TKR configuration [24], as shown in Fig. 1.8. The partnering dielectric material with refractive index n_d is still selected that satisfies the condition $n_\mathrm{p} > n_\mathrm{d}$. When light is incident on the prism/metal interface, a part of the light is reflected back into
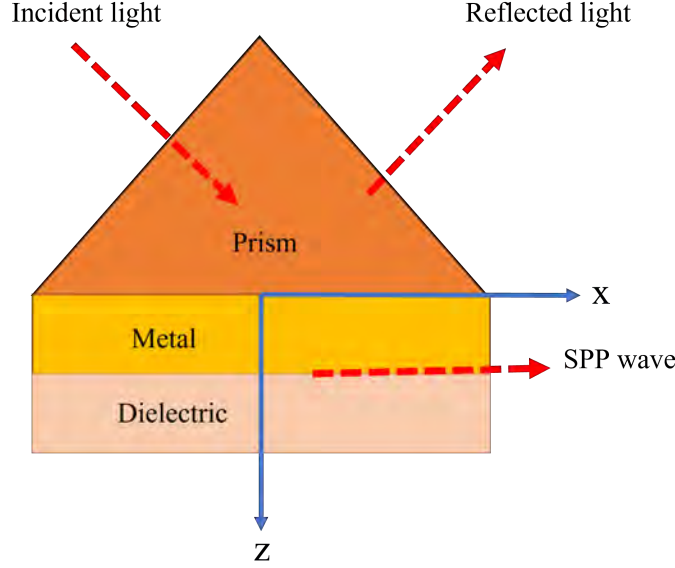
Figure 1.8: Schematic for the TKR configuration.

the prism and a part is refracted into the metal. The refracted wave travel perpendicular to the prism/metal interface and decays exponentially. If the metal film is thin, the refracted wave penetrates through the metal and couples with the surface-plasmon of the metal at the metal/dielectric interface. At a certain incidence angle, the electromagnetic boundary conditions are satisfied to excite the SPP wave. The TKR and Turbadar–Otto configurations essentially become the same for the excitation of Dyakonov surface waves since both partnering materials are dielectric.

1.5.2   Grating-Coupled Configuration

The excitation of any surface wave requires the matching of the wavenumber q of that surface wave with the magnitude of the component of the wave vector of the incident light parallel to the interface plane. In the prism-coupled configuration [3, 4, 96], this can happen for a very narrow range of the incidence angle, when both partnering materials have either small or negligible dissipation. However, in the grating-coupled configuration [1, 3], the matching can happen at more than one value of the incidence angle [13] since diffraction from a grating involves a multiplicity of non-specular Floquet harmonics [97]. Additionally, the grating-coupled configuration removes the need for a high-refractive-index material to couple incident light to surface waves. The SPP waves, which are normally nonradiative, can be efficiently coupled with light in the reverse process using the grating-coupled configuration [98] and allows better incorporation of SPP wave-based chemical sensors [99]. In the grating-coupled configuration, both partnering materials are of finite thickness but their interface is an undulating surface
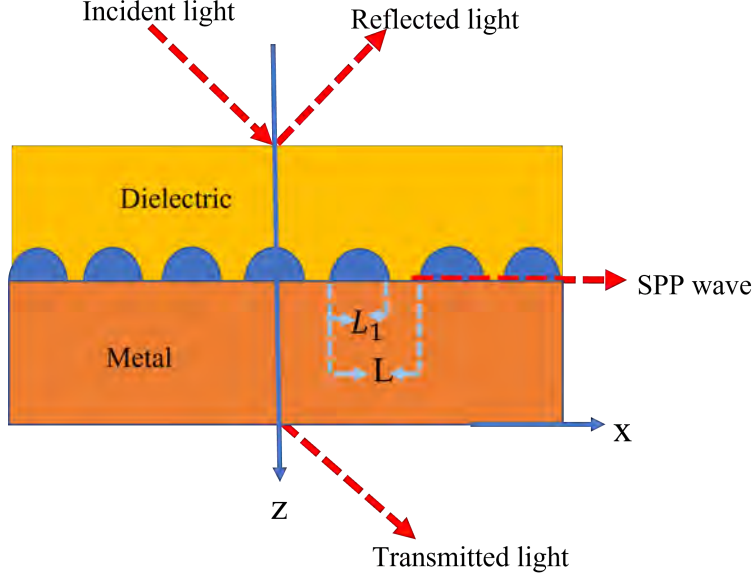
Figure 1.9: Schematic for the grating-coupled configuration.

$z = g(x, y) = g(x \pm L)$, where L is the period along the x axis instead of plane. The schematic of the grating-coupled configuration is presented in Fig. 1.9. By illuminating the periodic corrugations of a metallic surface-relief grating coupled with the dielectric material, SPP waves can be excited in grating-coupled configuration. The electromagnetic fields in grating-coupled configuration must be represented as linear superpositions of Floquet harmonics. If the component of the wave vector of a Floquet harmonic in the grating plane is same as that of the SPP wave, then SPP wave of that Floquet harmonic is excited. In this thesis, a CTF [13, 84, 91] or a uniaxial [20] material is partnered with an isotropic material in the grating-coupled configuration.

1.5.3 Waveguide-Coupled Configuration

A less common technique for exciting SPP waves is through an optical dielectric waveguide. Typically, a dielectric waveguide is integrated with a metal/dielectric interface, as shown schematically in Fig. 1.10. When a waveguide mode propagating in the dielectric waveguide has the same phase speed $\omega / \mathrm{Re}(q)$ as that of an SPP wave guided by the metal/dielectric interface, the electromagnetic energy from the waveguide mode in the dielectric waveguide couples with the SPP wave guided by the metal/dielectric interface. This configuration has the advantage of exciting SPP waves directly into the metal/dielectric interface. The waveguide-coupled configuration can potentially be used for the excitation of Dyakonov surface waves as well.

Waveguide modes
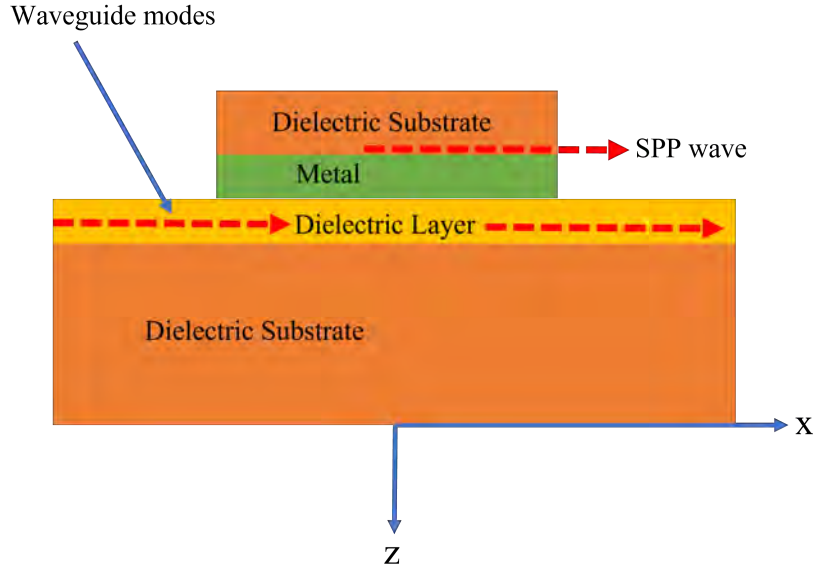
Figure 1.10: Schematic of the waveguide-coupled configuration.

1.6 Applications of Surface Waves

Out of the various types of surface waves, the SPP waves are widely used in practical applications. Researchers are focused on applications of these waves for optical sensing [1], imaging [100, 101], communications [102, 103], and harvesting light in solar cells [104]. The characteristics of the SPP waves are sensitive to the refractive index of the partnering dielectric material and can detect a small change in refractive index of partnering dielectric material near the interface [105–108]. Due to this property, surface plasmon resonance (SPR) can detect the change as low as 3×10^{-7} in the refractive index of the partnering dielectric material [2]. For sensing molecules and analytes near the interface, the prism-coupled configuration is suitable; however, TKR is used more than Turbadar–Otto configuration due to ease of implementation.

Two different techniques are used in sensing: angular interrogation technique and frequency interrogation technique. In angular interrogation, the free space wavelength of the incident light is fixed and the shift in angle of incidence caused by the analyte's presence in the partnering dielectric material is observed at which the external light couples to the SPP wave. In frequency interrogation technique, the wavelength that couples to the SPP wave shifts when a light source with a variable free-space wavelength is oriented at a fixed angle. Sensors based on Tamm waves have also been exploited for optical sensing [74]. Virus, bacteria and explosives can be sensed using the SPR-based sensors. The SPP waves can also be used in microscopic imaging [109] as two-dimensional [110] as well as three-dimensional SPR microscopes. Other applications include, imaging techniques used for lithography [4]; screening

of bioaffinity interactions with carbohydrates, DNA, and proteins using sensing technologies [111]; and high-speed communication of information on computer chips [112].

In order to obtain an image all at once, some researchers employ scanning method [113], while others prefer to use wide-field microscopy [114]. In both cases, SPR microscopy has an additive advantage with capabilities of capturing images of objects with extremely low contrast without the usage of markers or dyes. This is mainly because the SPP wave is highly sensitive and has strong field in the region near to the interface. Consequently, SPR microscopy is a good candidate for monitoring living organisms with lateral resolution of order less than a micrometer and a line of sight resolution in nanometers. SPR microscopy is often used in conjunction with fluorescent methods to achieve better results [115].

Applications of SPP waves in communications are on the horizon [99, 102]. In recent decades, optical fibres have revolutionised communications by providing greater bandwidth and transfer speeds than electrical currents over cables. The use of SPP waves have the potential to extend the advantages of optical fibres to the nanoscale and beyond when used for signal transmission and processing. While optical fibres are fast, diffraction limits downsizing to half a wavelength, which is enormous in contrast to today's nanoscale technologies. Using plasmonic waveguides with significantly smaller diameters, signals can be delivered both within and between components on a chip [116]. Recent research suggests that active plasmonic devices [117] and on-chip generators of SPP waves [118] may be feasible in the near future. In near future, a shift to photonic/plasmonic communication technology may be conceivable. Hence, plasmonics is a hot topic among many researchers these days. The SPP waves driven by subwavelength-scale structures are seen as a way to create dense, high-speed electronics by several researchers. Some suggested designs [119] aim to increase field intensity in the dielectric material while minimising it in the metal, thereby lowering dissipation. Surface waves steered by dielectric/dielectric interfaces may further minimise dissipation, supporting long-range communication.

In the optical regime, the technical exploitation of surface waves other than SPP waves is still in its early stages. Tamm waves have only lately been used for optical bio-sensing [74], despite the fact that they were discovered more than three decades ago [72]. Only recently have Dyakonov surface waves been experimentally observed for the first time [50]. The Dyakonov-Tamm wave [78] has yet to be exploited for applications. There are few instances of non-SPP surface wave applications in practice, there are many interesting ideas for prospective applications. Over 30 years had passed from the discovery [92] of optical methods to generate SPP waves before a commercial SPR sensor was introduced in 1990. Forecasting scientific and technological growth is always dangerous, but it appears that surface-wave applications are on the verge of becoming commonplace, especially given the present rapid advance in nanotechnology [120, 121]. Dyakonov, Tamm, and Dyakonov-Tamm waves are generally directed by interfaces made of dielectric materials. The loss of the dielectric materials of concern here is generally many orders of magnitude lower than that of metals. As a result, these waves have

significantly less attenuation than SPP waves, resulting in much longer propagation lengths. This raises the possibility of communications applications. In comparison to the more robust SPP wave, many other surface waves are significantly more sensitive to propagation direction and/or dielectric characteristics of an isotropic partnering material. Perhaps these characteristics will be used in the next generation of sensors to increase sensitivity.

1.7   Objectives of the Thesis

The focus of the research conducted for this thesis was on the excitation of the SPP waves and Dyakonov surface waves in the grating-coupled configuration with CTF and a uniaxial material AZO/silicon as partnering material for the excitation of these surface waves. The objectives of the research carried out for this dissertation were to;

  (i) quantify the effect of the orientation of the morphologically significant plane of a CTF on the excitation of SPP waves and Dyakonov surface waves;

 (ii) demonstrate the excitation of high-phase-speed Dyakonov surface waves in the grating-coupled configuration; and

(iii) explore the characteristics of the optical sensors based on SPP waves in the grating-coupled configuration and its dependence on the morphologically significant plane of the CTF.

1.8   Organization of the Thesis

To achieve these objectives, the excitation of SPP waves guided by a CTF deposited on a one-dimensional metallic surface-relief grating is studied in Chap. 2, when either the p- or s-polarized light is incident on surface-relief grating of a matal and CTF. It is considered that the plane of incidence and/or the morphologically significant plane of the CTF do not coincide with the grating plane.

In Chap. 3, the metal is replaced with an isotropic dielectric material for the excitation of Dyakonov surface waves. The wavenumbers of the possible Dyakonov surafce waves that can be supported by the glass/CTF interface are found as functions of the incident angle for different values of the vepor deposition angle χ_v from the associated canonical-boundary value problem. The excitation of Dyakonov surface waves guided by a CTF deposited on a one-dimensional dielectric surface-relief grating is studied, when either the p- or s-polarized light is incident on the surface-relief grating of a dielectric (glass) and CTF.

In Chap. 4, the wavenumbers of the possible Dyakonov surafce waves that can be supported by the air/uniaxial interface are found. The uniaxial material is considered to be a laminar composite material comprising alternating electrically thin sheets of aluminum-doped

zinc oxide (AZO) and silicon. Some of the solutions of the boundary-value problem indicated the existence of Dyakonov surface waves with a phase speed greater than the speed of light, that is $v_{\mathrm{ph}} = \omega/\mathrm{Re}(q) > c_0$, where $c_0 = 1/\sqrt{\varepsilon_0 \mu_0}$. The grating-coupled configuration is used to demonstrate the excitation of high-phase-speed Dyakonov surface waves.

An optical sensor for sensing the refractive index of a fluid infiltrating a CTF is investigated in Chap. 5. For this purpose, an optical sensor is analyzed for the plane-wave illumination of a CTF on top of a one-dimensional metallic surface-relief grating.

Chapter 2

Excitation of SPP waves at CTF/Metal Interface

The surface plasmon-polariton (SPP) waves are electromagnetic surface waves that can be excited by various practical configurations as discussed in Chap. 1. In a previous theoretical study [13] involving a columnar thin film (CTF) grown on a one-dimensional metallic grating with the grating plane congruent with the morphologically significant plane of the CTF, it was found that the SPP wave was excited as a Floquet harmonic of different orders for p-polarized incidence only and not for s-polarized incidence. The incidence plane, grating plane, and the morphologically significant plane of the CTF were all the same in that study [13].

When the plane of incidence is congruent with the morphologically significant plane, the solution of the underlying canonical boundary-value problem indicates that the SPP wave must be p-polarized [122]. But when the two planes are non-congruent, the SPP wave cannot be accorded a specfic polarization state; labeling its polarization state as hybrid [123] is inapt [124] because the field inside the CTF comprises two extraordinary components [125, 126] that cannot be labeled as of either the p- or the s-polarization state. Therefore, it is possible that incident s-polarized light can also excite an SPP wave when the plane of incidence, the grating plane, and the morphologically significant plane are all different. This issue motivated the work reported in this chapter: the mathematical formulation of the boundary-value problem is described in Sec. 2.1, where the rigorous coupled-wave approach (RCWA) is adopted to solve the problem. Numerical results are presented and discussed in Sec. 2.2. Conclusions are presented in Sec. 2.3.

This chapter is based on: K. Mujeeb, M. Faryad, J. V. Urbina, and A. Lakhtakia. Effect of orientation on excitation of surface plasmon-polariton waves guided by a columnar thin film deposited on a metal grating. Optical Engineering, 59(5): 055103, 2020; errata: 59(6): 069801, 2020.

2.1 Boundary-Value Problem

Let me now consider the schematic of the boundary-value problem shown in Fig. 3.1. The region $0 < z < L_c$ is occupied by a CTF, the region $L_c + L_g < z < L_t$ by a metal of relative permittivity ε_m, and the half-spaces $z < 0$ and $z > L_t$ are occupied by air, where $L_t = L_c + L_g + L_m$. The intermediate region $L_c < z < L_c + L_g$ by a one-dimensional metallic grating with the CTF inside the troughs of the grating. The xz plane is the grating plane with L being the period along the x axis. The relative permittivity dyadic of the CTF is stated in Eq. (1.24) in Chap. 1. The relative permittivity dyadic $\underline{\underline{\varepsilon}}_{gr}(x,z) = \underline{\underline{\varepsilon}}_{gr}(x \pm L, z)$ in the intermediate region
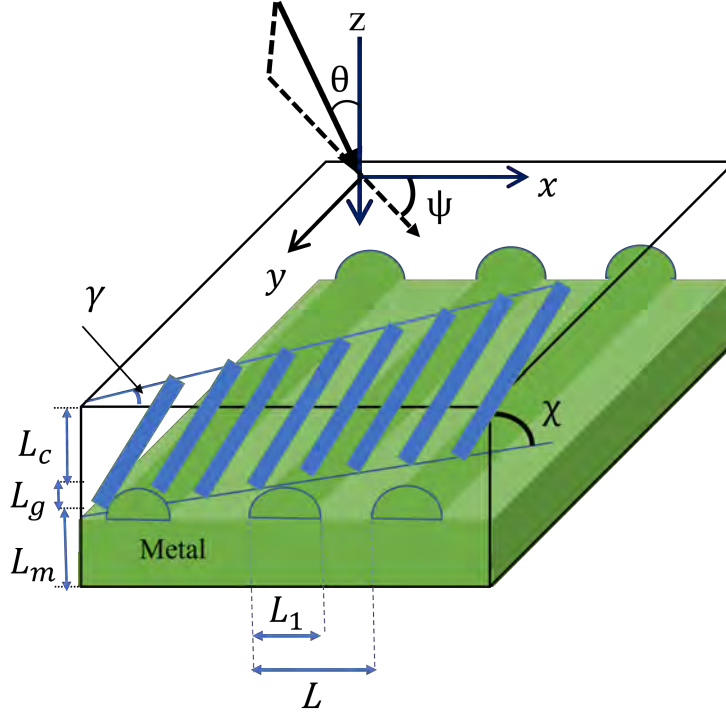
Figure 2.1: Schematic of the boundary-value problem solved for the grating-coupled configuration. The CTF is symbolically represented by a single row of nanocolumns.

$L_c < z < L_c + L_g$ is specified as

$$\underline{\underline{\varepsilon}}_{gr}(x,z) = \begin{cases} \varepsilon_m \underline{\underline{I}} - \left(\varepsilon_m \underline{\underline{I}} - \underline{\underline{\varepsilon}}_{CTF} \right) Y[L_g + L_c - z - f(x)], & x \in [0, L_1), \\ \underline{\underline{\varepsilon}}_{CTF'} & x \in (L_1, L], \end{cases}$$
$$z \in (L_c, L_c + L_g),$$

$$(2.1)$$

where $L_1 \in (0, L]$, the identity dyadic $\underline{\underline{I}} = \hat{\mathbf{u}}_x\hat{\mathbf{u}}_x + \hat{\mathbf{u}}_y\hat{\mathbf{u}}_y + \hat{\mathbf{u}}_z\hat{\mathbf{u}}_z$, and the unit step function,

$$Y(\xi) = \begin{cases} 1, & \xi \geq 0, \\ 0, & \xi < 0, \end{cases} \tag{2.2}$$

and grating shape function is

$$f(x) = L_g \sin(\pi x / L_1), \qquad L_1 \in [0, L], \tag{2.3}$$

for all numerical results presented here.

$$\underline{\underline{\varepsilon}}(x, z) = \sum_{n \in \mathbb{Z}} \underline{\underline{\varepsilon}}^{(n)}(z) \exp(i2n\pi x/L), \quad z \in (0, L_t), \tag{2.4}$$

where $\mathbb{Z} = \{0, \pm 1, \pm 2, \ldots\ldots\}$ and the Fourier coefficients

$$\underline{\underline{\varepsilon}}^{(n)}(z) = \begin{cases} \frac{1}{L} \int_0^L \underline{\underline{\varepsilon}}_{gr}(x, z) \exp(-in2\pi x/L) dx, & z \in (L_c, L_c + L_g), \\ \underline{\underline{0}}, & z \notin (L_c, L_c + L_g), \end{cases} \tag{2.5}$$

for $n \neq 0$ but

$$\underline{\underline{\varepsilon}}^{(0)}(z) = \begin{cases} \underline{\underline{\varepsilon}}_{CTF}, & z \in (0, L_c), \\ \frac{1}{L} \int_0^L \underline{\underline{\varepsilon}}_{gr}(x, z) dx, & z \in (L_c, L_c + L_g), \\ \varepsilon_m \underline{\underline{I}}, & z \in (L_c + L_g, L_t). \end{cases} \tag{2.6}$$

Consider the interface $z = 0$ to be illuminated by a plane wave propagating at the azimuthal angle $\psi \in [0°, 360°)$ (with respect to the x axis in the xz plane) and the polar angle $\theta \in [0°, 90°)$ (with respect to the z axis). Thus, the plane of incidence is jointly defined by the unit vectors $\hat{\mathbf{u}}_x \cos\psi + \hat{\mathbf{u}}_y \sin\psi$ and $\hat{\mathbf{u}}_z$. The field phasors of the incident, reflected, and transmitted plane

wave in terms of Floquet harmonics [3] can be written as

$$\mathbf{E}_{\text{inc}}(\mathbf{r}) = \sum_{n\in\mathbb{Z}} (\mathbf{s}_n a_{\text{s}}^{(n)} + \mathbf{p}_n^+ a_{\text{p}}^{(n)}) \exp[i(k_{\text{x}}^{(n)} x + k_{\text{y}}^{(0)} y + k_{\text{z}}^{(n)} z)], \quad z < 0, \tag{2.7}$$

$$\eta_0 \mathbf{H}_{\text{inc}}(\mathbf{r}) = \sum_{n\in\mathbb{Z}} (\mathbf{p}_n^+ a_{\text{s}}^{(n)} - \mathbf{s}_n a_{\text{p}}^{(n)}) \exp[i(k_{\text{x}}^{(n)} x + k_{\text{y}}^{(0)} y + k_{\text{z}}^{(n)} z)], \quad z < 0, \tag{2.8}$$

$$\mathbf{E}_{\text{ref}}(\mathbf{r}) = \sum_{n\in\mathbb{Z}} (\mathbf{s}_n r_{\text{s}}^{(n)} + \mathbf{p}_n^- r_{\text{p}}^{(n)}) \exp[i(k_{\text{x}}^{(n)} x + k_{\text{y}}^{(0)} y - k_{\text{z}}^{(n)} z)], \quad z < 0, \tag{2.9}$$

$$\eta_0 \mathbf{H}_{\text{ref}}(\mathbf{r}) = \sum_{n\in\mathbb{Z}} (\mathbf{p}_n^- r_{\text{s}}^{(n)} + \mathbf{s}_n r_{\text{p}}^{(n)}) \exp[i(k_{\text{x}}^{(n)} x + k_{\text{y}}^{(0)} y - k_{\text{z}}^{(n)} z)], \quad z < 0, \tag{2.10}$$

$$\mathbf{E}_{\text{tr}}(\mathbf{r}) = \sum_{n\in\mathbb{Z}} (\mathbf{s}_n t_{\text{s}}^{(n)} + \mathbf{p}_n^+ t_{\text{p}}^{(n)}) \exp\{i[k_{\text{x}}^{(n)} x + k_{\text{y}}^{(0)} y + k_{\text{z}}^{(n)} (z - L_{\text{t}})]\}, \quad z > L_{\text{t}}, \tag{2.11}$$

$$\eta_0 \mathbf{H}_{\text{tr}}(\mathbf{r}) = \sum_{n\in\mathbb{Z}} (\mathbf{p}_n^+ t_{\text{s}}^{(n)} + \mathbf{s}_n t_{\text{p}}^{(n)}) \exp\{i[k_{\text{x}}^{(n)} x + k_{\text{y}}^{(0)} y + k_{\text{z}}^{(n)} (z - L_{\text{t}})]\}, \quad z > L_{\text{t}}, \tag{2.12}$$

where

$$k_{\text{x}}^{(n)}(\theta, \psi) = k_0 \cos\psi \sin\theta + 2n\pi/L, \tag{2.13}$$

$$k_{\text{y}}^{(0)}(\theta, \psi) = k_0 \sin\psi \sin\theta, \tag{2.14}$$

$$k_{\text{xy}}^{(n)}(\theta, \psi) = +\sqrt{(k_{\text{x}}^{(n)})^2 + (k_{\text{y}}^{(0)})^2}, \tag{2.15}$$

$$k_{\text{z}}^{(n)}(\theta, \psi) = \begin{cases} \sqrt{{k_0}^2 - (k_{\text{xy}}^{(n)})^2}, & {k_0}^2 > (k_{\text{xy}}^{(n)})^2, \\ i\sqrt{(k_{\text{xy}}^{(n)})^2 - {k_0}^2}, & {k_0}^2 < (k_{\text{xy}}^{(n)})^2, \end{cases} \tag{2.16}$$

$$\mathbf{s}_n(\theta, \psi) = \frac{-k_{\text{y}}^{(0)} \hat{\mathbf{u}}_{\text{x}} + k_{\text{x}}^{(n)} \hat{\mathbf{u}}_{\text{y}}}{k_{\text{xy}}^{(n)}}, \tag{2.17}$$

and

$$\mathbf{p}_n^{\pm}(\theta, \psi) = \mp \frac{k_{\text{z}}^{(n)}}{k_0} \left(\frac{k_{\text{x}}^{(n)} \hat{\mathbf{u}}_{\text{x}} + k_{\text{y}}^{(0)} \hat{\mathbf{u}}_{\text{y}}}{k_{\text{xy}}^{(n)}} \right) + \frac{k_{\text{xy}}^{(n)}}{k_0} \hat{\mathbf{u}}_{\text{z}}, \tag{2.18}$$

are functions of angle θ and ψ. The field phasors in the region $0 \le z \le L_{\text{t}}$ in terms of Floquet harmonics may be written as

$$\mathbf{E}_{\text{tr}}(\mathbf{r}) = \sum_{n\in\mathbb{Z}} [E_{\text{x}}^{(n)}(z)\hat{\mathbf{u}}_{\text{x}} + E_{\text{y}}^{(n)}(z)\hat{\mathbf{u}}_{\text{y}} + E_{\text{z}}^{(n)}(z)\hat{\mathbf{u}}_{\text{z}}] \exp[i(k_{\text{x}}^{(n)} x + k_{\text{y}}^{(0)} y)], \tag{2.19}$$

$$\mathbf{H}_{\text{tr}}(\mathbf{r}) = \sum_{n\in\mathbb{Z}} [H_{\text{x}}^{(n)}(z)\hat{\mathbf{u}}_{\text{x}} + H_{\text{y}}^{(n)}(z)\hat{\mathbf{u}}_{\text{y}} + H_{\text{z}}^{(n)}(z)\hat{\mathbf{u}}_{\text{z}}] \exp[i(k_{\text{x}}^{(n)} x + k_{\text{y}}^{(0)} y)]. \tag{2.20}$$

Substituting Eq. (2.4) and Eqs. (2.19)-(2.20) in the frequency-domain Maxwell curl postulates, a system of four ordinary differential equations and two algebraic equations has been obtained

and given as follows:

$$\frac{d}{dz}E_{\text{x}}^{(\text{n})}(z) = ik_0\eta_0 H_{\text{y}}^{(\text{n})}(z) + ik_{\text{x}}^{(n)} E_{\text{z}}^{(\text{n})}(z), \tag{2.21}$$

$$\frac{d}{dz}E_{\text{y}}^{(\text{n})}(z) = -ik_0\eta_0 H_{\text{y}}^{(\text{n})}(z) + ik_{\text{y}}^{(0)} E_{\text{z}}^{(\text{n})}(z), \tag{2.22}$$

$$\frac{d}{dz}H_{\text{x}}^{(\text{n})}(z) = ik_{\text{x}}^{(n)} H_{\text{z}}^{(\text{n})}(z) - i\frac{k_0}{\eta_0} \tag{2.23}$$
$$\times \sum_{n\in\mathbb{Z}} [\varepsilon_{\text{yx}}^{(n-m)} E_{\text{x}}^{(\text{n})}(z) + \varepsilon_{\text{yy}}^{(n-m)} E_{\text{y}}^{(\text{n})}(z) + \varepsilon_{\text{yz}}^{(n-m)} E_{\text{z}}^{(\text{n})}(z)],$$

$$\frac{d}{dz}H_{\text{y}}^{(\text{n})}(z) = ik_{\text{y}}^{(0)} H_{\text{z}}^{(\text{n})}(z) + i\frac{k_0}{\eta_0} \tag{2.24}$$
$$\times \sum_{n\in\mathbb{Z}} [\varepsilon_{\text{xx}}^{(n-m)} E_{\text{x}}^{(\text{n})}(z) + \varepsilon_{\text{xy}}^{(n-m)} E_{\text{y}}^{(\text{n})}(z) + \varepsilon_{\text{xz}}^{(n-m)} E_{\text{z}}^{(\text{n})}(z)],$$

and two algerbaic equations

$$k_{\text{y}}^{(0)} E_{\text{x}}^{(\text{n})} - k_{\text{x}}^{(n)} E_{\text{y}}^{(\text{n})}(z) = -k_0\eta_0 H_{\text{z}}^{(\text{n})}(z), \tag{2.25}$$

$$k_{\text{y}}^{(0)} H_{\text{x}}^{(\text{n})} - k_{\text{x}}^{(n)} H_{\text{y}}^{(\text{n})}(z) = \frac{k_0}{\eta_0} \tag{2.26}$$
$$\times \sum_{n\in\mathbb{Z}} [\varepsilon_{\text{zx}}^{(n-m)} E_{\text{x}}^{(\text{n})}(z) + \varepsilon_{\text{zy}}^{(n-m)} E_{\text{y}}^{(\text{n})}(z) + \varepsilon_{\text{zz}}^{(n-m)} E_{\text{z}}^{(\text{n})}(z)].$$

During all computations , $n \leq N_{\text{s}}$ was restricted. Equations (2.21)–(2.26) holds for all $z \in (0, L_{\text{t}})$. Using Eq. (2.25) and Eq. (2.26) in Eqs. (2.21)–(2.24) results in the four ordinary differential equations, and can be demonstrated as

$$\frac{d}{dz}[\mathbf{f}(z)] = i[\underline{\underline{P}}(z)] \bullet [\mathbf{f}(z)], \tag{2.27}$$

where $[\underline{\underline{P}}(z)]$ is given as

$$[\underline{\underline{P}}(z)] = \begin{bmatrix} [\underline{\underline{P}}_{11}(z)] & [\underline{\underline{P}}_{12}(z)] & [\underline{\underline{P}}_{13}(z)] & [\underline{\underline{P}}_{14}(z)] \\ [\underline{\underline{P}}_{21}(z)] & [\underline{\underline{P}}_{22}(z)] & [\underline{\underline{P}}_{23}(z)] & [\underline{\underline{P}}_{24}(z)] \\ [\underline{\underline{P}}_{31}(z)] & [\underline{\underline{P}}_{32}(z)] & [\underline{\underline{P}}_{33}(z)] & [\underline{\underline{P}}_{34}(z)] \\ [\underline{\underline{P}}_{41}(z)] & [\underline{\underline{P}}_{42}(z)] & [\underline{\underline{P}}_{43}(z)] & [\underline{\underline{P}}_{44}(z)] \end{bmatrix}. \tag{2.28}$$

Consider $[\underline{P}_{\alpha\beta}(z)] = [\underline{P}_{\alpha\beta}]$ and

$$[\underline{P}_{11}] = -[\underline{\mathcal{K}}_x] \cdot [\underline{\varepsilon}_{zz}(z)]^{-1} \cdot [\underline{\varepsilon}_{zx}(z)], \tag{2.29}$$

$$[\underline{P}_{12}] = -[\underline{\mathcal{K}}_x] \cdot [\underline{\varepsilon}_{zz}(z)]^{-1} \cdot [\underline{\varepsilon}_{zy}(z)], \tag{2.30}$$

$$[\underline{P}_{13}] = \frac{k_y^{(0)}}{k_0}[\underline{\mathcal{K}}_x] \cdot [\underline{\varepsilon}_{zz}(z)]^{-1}, \tag{2.31}$$

$$[\underline{P}_{14}] = k_0[\underline{I}] - \frac{1}{k_0}[\underline{\mathcal{K}}_x] \cdot [\underline{\varepsilon}_{zz}(z)]^{-1} \cdot [\underline{\mathcal{K}}_x], \tag{2.32}$$

$$[\underline{P}_{21}] = -k_y^{(0)}[\underline{\varepsilon}_{zz}(z)]^{-1} \cdot [\underline{\varepsilon}_{zx}(z)], \tag{2.33}$$

$$[\underline{P}_{22}] = -k_y^{(0)}[\underline{\varepsilon}_{zz}(z)]^{-1} \cdot [\underline{\varepsilon}_{zy}(z)], \tag{2.34}$$

$$[\underline{P}_{23}] = -k_0[\underline{I}] + \frac{k_y^{(0)2}}{k_0}[\underline{\varepsilon}_{zz}(z)]^{-1}, \tag{2.35}$$

$$[\underline{P}_{24}] = -\frac{k_y^{(0)}}{k_0}[\underline{\varepsilon}_{zz}(z)]^{-1} \cdot [\underline{\mathcal{K}}_x], \tag{2.36}$$

$$[\underline{P}_{31}] = -k_0[\underline{\varepsilon}_{yx}(z)] + k_0[\underline{\varepsilon}_{yz}(z)] \cdot [\underline{\varepsilon}_{zz}(z)]^{-1} \cdot [\underline{\varepsilon}_{zx}(z)] - \frac{k_y^{(0)}}{k_0}[\underline{\mathcal{K}}_x], \tag{2.37}$$

$$[\underline{P}_{32}] = -k_0[\underline{\varepsilon}_{yy}(z)] + k_0[\underline{\varepsilon}_{yz}(z)] \cdot [\underline{\varepsilon}_{zz}(z)]^{-1} \cdot [\underline{\varepsilon}_{zy}(z)] + \frac{1}{k_0}[\underline{\mathcal{K}}_x]^2, \tag{2.38}$$

$$[\underline{P}_{33}] = -k_y^{(0)}[\underline{\varepsilon}_{yz}(z)] \cdot [\underline{\varepsilon}_{zz}(z)]^{-1}, \tag{2.39}$$

$$[\underline{P}_{34}] = [\underline{\varepsilon}_{yz}(z)] \cdot [\underline{\varepsilon}_{zz}(z)]^{-1} \cdot [\underline{\mathcal{K}}_x], \tag{2.40}$$

$$[\underline{P}_{41}] = k_0[\underline{\varepsilon}_{xx}(z)] - k_0[\underline{\varepsilon}_{xz}(z)] \cdot [\underline{\varepsilon}_{zz}(z)]^{-1} \cdot [\underline{\varepsilon}_{zx}(z)] - \frac{k_y^{(0)2}}{k_0}[\underline{\mathcal{K}}_x], \tag{2.41}$$

$$[\underline{P}_{42}] = k_0[\underline{\varepsilon}_{xy}(z)] - k_0[\underline{\varepsilon}_{xz}(z)] \cdot [\underline{\varepsilon}_{zz}(z)]^{-1} \cdot [\underline{\varepsilon}_{zy}(z)] + \frac{k_y^{(0)2}}{k_0}[\underline{\mathcal{K}}_x], \tag{2.42}$$

$$[\underline{P}_{43}] = k_y^{(0)}[\underline{\varepsilon}_{xz}(z)] \cdot [\underline{\varepsilon}_{zz}(z)]^{-1}, \tag{2.43}$$

$$[\underline{P}_{44}] = -[\underline{\varepsilon}_{xz}(z)] \cdot [\underline{\varepsilon}_{zz}(z)]^{-1} \cdot [\underline{\mathcal{K}}_x], \tag{2.44}$$

where $[\underline{\mathcal{K}}_x] = diag[k_x^{(n)}]$, and $[\mathbf{f}(z)]$ is the column vector. The column vector $[\mathbf{f}(z)]$ has $4(2N_s + 1)$ components and is defined as

$$[\mathbf{f}(z)] = [[\mathbf{E}_x(z)]^T, [\mathbf{E}_y(z)]^T, \eta_0[\mathbf{H}_x(z)]^T, \eta_0[\mathbf{H}_y(z)]^T]. \tag{2.45}$$

The column vector $\mathbf{f}(z)$ can be computed at $z = 0$ and $z = L_t$ using the field Eqs. (2.7)–(2.12) as

$$[\mathbf{f}(0)] = \begin{bmatrix} [\underline{Y}_e^{(\text{inc})}] & [\underline{Y}_e^{(\text{ref})}] \\ [\underline{Y}_h^{(\text{inc})}] & [\underline{Y}_h^{(\text{ref})}] \end{bmatrix} \cdot \begin{bmatrix} [\mathbf{A}] \\ [\mathbf{R}] \end{bmatrix}, \tag{2.46}$$

and

$$[\mathbf{f}(L_t)] = \begin{bmatrix} [\underline{\underline{Y}}_e^{(\text{inc})}] \\ [\underline{\underline{Y}}_h^{(\text{inc})}] \end{bmatrix} \cdot [\mathbf{T}], \tag{2.47}$$

with

$$[\underline{\underline{Y}}_e^{(\text{inc})}] = \begin{bmatrix} -\dfrac{k_y^{(0)}}{k_{xy}^{(n)}} & \dfrac{k_z^{(n)}}{k_0}\dfrac{k_x^{(n)}}{k_{xy}^{(n)}} \\[2ex] \dfrac{k_x^{(n)}}{k_{xy}^{(n)}} & \dfrac{k_z^{(n)}}{k_0}\dfrac{k_y^{(0)}}{k_{xy}^{(n)}} \end{bmatrix}, \tag{2.48}$$

$$[\underline{\underline{Y}}_e^{(\text{ref})}] = \begin{bmatrix} -\dfrac{k_y^{(0)}}{k_{xy}^{(n)}} & -\dfrac{k_z^{(n)}}{k_0}\dfrac{k_x^{(n)}}{k_{xy}^{(n)}} \\[2ex] \dfrac{k_x^{(n)}}{k_{xy}^{(n)}} & -\dfrac{k_z^{(n)}}{k_0}\dfrac{k_y^{(0)}}{k_{xy}^{(n)}} \end{bmatrix}, \tag{2.49}$$

$$[\underline{\underline{Y}}_h^{(\text{inc})}] = \begin{bmatrix} \dfrac{k_z^{(n)}}{k_0}\dfrac{k_x^{(n)}}{k_{xy}^{(n)}} & \dfrac{k_y^{(0)}}{k_{xy}^{(n)}} \\[2ex] \dfrac{k_z^{(n)}}{k_0}\dfrac{k_y^{(0)}}{k_{xy}^{(n)}} & -\dfrac{k_x^{(n)}}{k_{xy}^{(n)}} \end{bmatrix}, \tag{2.50}$$

and

$$[\underline{\underline{Y}}_h^{(\text{ref})}] = \begin{bmatrix} -\dfrac{k_z^{(n)}}{k_0}\dfrac{k_x^{(n)}}{k_{xy}^{(n)}} & \dfrac{k_y^{(0)}}{k_{xy}^{(n)}} \\[2ex] -\dfrac{k_z^{(n)}}{k_0}\dfrac{k_y^{(0)}}{k_{xy}^{(n)}} & -\dfrac{k_x^{(n)}}{k_{xy}^{(n)}} \end{bmatrix}. \tag{2.51}$$

$[\mathbf{A}]$, $[\mathbf{R}]$, and $[\mathbf{T}]$ used in above equations are given as

$$[\mathbf{A}] = [a_s^{(-N_s)}, a_s^{(-N_s+1)}, a_s^{(-N_s+2)}, \ldots\ldots\ldots, a_s^{(0)}, \ldots\ldots\ldots\ldots, a_s^{(N_s-2)}, , a_s^{(N_s-1)}, a_s^{(N_s)}$$
$$a_p^{(-N_s)}, a_p^{(-N_s+1)}, a_p^{(-N_s+2)} \ldots\ldots\ldots a_p^{(0)}, \ldots\ldots\ldots\ldots, a_p^{(N_s-2)}, a_p^{(N_s-1)}, a_p^{(N_s)}]^T. \tag{2.52}$$

$$[\mathbf{R}] = [r_s^{(-N_s)}, r_s^{(-N_s+1)}, r_s^{(-N_s+2)} \ldots\ldots\ldots r_s^{(0)}, \ldots\ldots\ldots\ldots, r_s^{(N_s-2)}, r_s^{(N_s-1)}, r_s^{(N_s)}$$
$$r_p^{(-N_s)}, r_p^{(-N_s+1)}, r_p^{(-N_s+2)} \ldots\ldots\ldots r_p^{(0)}, \ldots\ldots\ldots\ldots, r_p^{(N_s-2)}, r_p^{(N_s-1)}, r_p^{(N_s)}]^T, \tag{2.53}$$

$$[\mathbf{T}] = [t_s^{(-N_s)}, t_s^{(-N_s+1)}, t_s^{(-N_s+2)} \ldots\ldots\ldots t_s^{(0)}, \ldots\ldots\ldots\ldots, t_s^{(N_s-2)}, t_s^{(N_s-1)}, t_s^{(N_s)}$$
$$t_p^{(-N_s)}, t_p^{(-N_s+1)}, t_p^{(-N_s+2)} \ldots\ldots\ldots t_p^{(0)}, \ldots\ldots\ldots\ldots, t_p^{(N_s-2)}, t_p^{(N_s-1)}, t_p^{(N_s)}]^T. \tag{2.54}$$

In order to devise a stable algorithm to evaluate the unknown $[\mathbf{R}]$ and $[\mathbf{T}]$ for known $[\mathbf{A}]$ [3, 127], the region $0 \leq z \leq L_t$ is divided into slices. The region $0 \leq z \leq L_c$ is divided into N_c slices, $L_c \leq L_c + L_g$ into N_g slices, and $L_c + L_g \leq z \leq L_t$ is divided into N_m slices. The above division of regions provide $N_c + N_g + N_m$ slices and $N_c + N_g + N_m + 1$ interfaces. In the ℓth slice, bounded by the planes $z = z_{\ell-1}$ and $z = z_\ell$, where $\ell \in [1, N_c + N_g + N_m]$, approximate $[\underline{\underline{P}}(z)]$ as

$$[\underline{\underline{P}}(z)] = [\underline{\underline{P}}]_\ell = \left[\underline{\underline{P}}\left(\frac{z_{\ell-1} + z_\ell}{2}\right)\right], \quad z \in (z_\ell, z_{\ell-1}). \tag{2.55}$$

Equation (2.27) can be written as [128]

$$[\mathbf{f}(z_{\ell-1})] = [\underline{\underline{V}}]_\ell \cdot \exp\{-id_\ell[\underline{\underline{D}}]_\ell\} \cdot [\underline{\underline{V}}]_\ell^{-1} \cdot [\mathbf{f}(z_\ell)]. \tag{2.56}$$

In Eq. (2.56), $d_\ell = z_\ell - z_{\ell-1}$, $[\underline{\underline{V}}]_\ell$ is a square matrix with eigenvectors of matrix $[\underline{\underline{P}}]_\ell$ as its columns and $[\underline{\underline{D}}]_\ell$ is a diagonal matrix with eigenvalues of $[\underline{\underline{P}}]_\ell$. The auxiliary column vector $[\mathbf{T}]_\ell$ and the transmission matrix $[\underline{\underline{Z}}]_\ell^{\text{low}}$ can be defined as [129]

$$[\mathbf{f}(z_{\ell-1})] = [\underline{\underline{Z}}]_\ell \cdot [\mathbf{T}]_\ell, \quad \ell \in [0, N_c + N_g + N_m], \tag{2.57}$$

where

$$[\mathbf{T}]_{N_c+N_g+N_m} = [\mathbf{T}], \tag{2.58}$$

$$[\underline{\underline{Z}}]_{N_c+N_g+N_m} = \begin{bmatrix} [\underline{\underline{Y}}_e^{(\text{inc})}] \\ [\underline{\underline{Y}}_h^{(\text{inc})}] \end{bmatrix}. \tag{2.59}$$

Solving Eq. (2.56) and (2.57)

$$[\underline{\underline{Z}}]_{\ell-1} \cdot [\mathbf{T}]_{\ell-1} = [\underline{\underline{V}}]_\ell \cdot \begin{bmatrix} \exp\{-id_\ell[\underline{\underline{D}}]_\ell^{\text{upp}}\} & 0 \\ 0 & \exp\{-id_\ell[\underline{\underline{D}}]_\ell^{\text{low}}\} \end{bmatrix} \cdot [\underline{\underline{V}}]_\ell^{-1} \cdot [\underline{\underline{Z}}]_\ell \cdot [\mathbf{T}]_\ell, \tag{2.60}$$

$$\ell \in [1, N_c + N_g + N_m],$$

$[\underline{\underline{D}}]_\ell^{\text{upp}}$ is the upper diagonal submatrix of $[\underline{\underline{D}}]_\ell$ and $[\underline{\underline{D}}]_\ell^{\text{low}}$ is lower diagonal submatrix of $[\underline{\underline{D}}]_\ell$, provided that the imaginary part of the eigenvalues of matrix $[\underline{\underline{D}}]_\ell$ are arranged in decreasing order. Since both $[\mathbf{T}]_\ell$ and $[\underline{\underline{Z}}]_\ell^{\text{low}}$ are unknown and cannot be determined simultaneously from Eq. (2.60), so formulate

$$[\mathbf{T}]_{\ell-1} = \exp\{-id_\ell[\underline{\underline{D}}]_\ell^{\text{upp}}\} \cdot [\underline{\underline{X}}]_\ell^{\text{upp}} \cdot [\mathbf{T}]_\ell, \tag{2.61}$$

where $[\underline{\underline{X}}]_\ell^{\text{low}}$ and $[\underline{\underline{X}}]_\ell^{\text{upp}}$ are defined via

$$\begin{bmatrix} [\underline{\underline{X}}]_\ell^{\text{upp}} \\ [\underline{\underline{X}}]_\ell^{\text{low}} \end{bmatrix} = [\underline{\underline{V}}]_\ell^{-1} \cdot [\underline{\underline{Z}}]_\ell. \tag{2.62}$$

Substituting Eq. (2.61) in Eq. (2.60)

$$[\underline{\underline{Z}}]_{\ell-1} = [\underline{\underline{V}}]_\ell \cdot \begin{bmatrix} [\underline{\underline{I}}] \\ \exp\{-id_\ell[\underline{\underline{D}}]_\ell^{\text{low}}\} \cdot [\underline{\underline{X}}]_\ell^{\text{low}} \cdot \{[\underline{\underline{X}}]_\ell^{\text{upp}}\}^{-1} \cdot \exp\{id_\ell[\underline{\underline{D}}]_\ell^{\text{upp}}\} \end{bmatrix}, \tag{2.63}$$

$$\ell \in [1, N_c + N_g + N_m].$$

From Eq. (2.62) and Eq. (2.63), $[\underline{\underline{Z}}]_0$ is found in terms of $[\underline{\underline{Z}}]_{N_c+N_g+N_m}$. After partitioning, the matrix $[\underline{\underline{Z}}]_0$ is written as the lower submatrix $[\underline{\underline{Z}}]_0^{\text{low}}$ and upper submatrix $[\underline{\underline{Z}}]_0^{\text{low}}$ as

$$[\underline{\underline{Z}}]_0 = \begin{bmatrix} [\underline{\underline{Z}}]_0^{\text{upp}} \\ [\underline{\underline{Z}}]_0^{\text{low}} \end{bmatrix}. \tag{2.64}$$

$[\mathbf{R}]$ and $[\mathbf{T}]_0$ are found using Eqs. (2.46)–(2.57)

$$\begin{bmatrix} [\mathbf{T}]_0 \\ [\mathbf{R}] \end{bmatrix} = \begin{bmatrix} [\underline{\underline{Z}}]_0^{\text{upp}} & -[\underline{Y}_e^{(\text{ref})}] \\ [\underline{\underline{Z}}]_0^{\text{low}} & -[\underline{Y}_h^{(\text{ref})}] \end{bmatrix}^{-1} \cdot \begin{bmatrix} [\underline{Y}_e^{(\text{inc})}] \\ [\underline{Y}_h^{(\text{inc})}] \end{bmatrix} \cdot [\mathbf{A}]. \tag{2.65}$$

Equation (2.65) was obtained by enforcing the boundary conditions across the plane $z = 0$. After $[\mathbf{T}]_0$ is known $[\mathbf{T}] = [\mathbf{T}]_{N_c+N_g+N_m}$ is found by reversing the sense of iteration in Eq. (2.61). The unknown amplitudes $r_s^{(n)}$, $r_p^{(n)}$, $t_s^{(n)}$, and $t_p^{(n)}$ have to be determined in terms of the known $a_s^{(n)}$ and $a_p^{(n)}$

$$\left. \begin{array}{l} a_s^{(n)} = \bar{a}_s \, \delta_{n0}, \\ a_p^{(n)} = \bar{a}_p \, \delta_{n0}, \end{array} \right\} \quad z \in [0, L_t], \tag{2.66}$$

where δ_{nm} is the Kronecker delta, $\bar{a}_p = 0$ for an incident s-polarized plane wave, and $\bar{a}_s = 0$ for an incident p-polarized plane wave. In the above RCWA, the electric and magnetic field phasors in the region $0 < z < L_t$ are expanded in terms of Floquet harmonics with unknown coefficients [14, 15]. The Floquet harmonics express the x-dependences using the functions $\exp(ik_x^{(n)}x)$, the unknown coefficients are functions of z, and the y-dependence is simply $\exp(ik_y^{(0)}y)$. After the expansions of the field phasors as well as the Fourier series given in Eq. (2.4) are substituted in the frequency-domain Maxwell curl postulates, the piecewise-uniform approximation is used. All expansions are truncated to exclude $|n| > N_s > 0$. A stable algorithm is then used to determine the unknown coefficients $r_s^{(n)}$, $r_p^{(n)}$, $t_s^{(n)}$, and $t_p^{(n)}$ for $n \in [-N_s, N_s]$ in terms of $\bar{a}_s$ and $\bar{a}_p$ [3]. The results are compactly expressed using the matrix equations

$$\begin{bmatrix} r_s^{(n)} \\ r_p^{(n)} \end{bmatrix} = \begin{bmatrix} r_{ss}^{(n)} & r_{sp}^{(n)} \\ r_{ps}^{(n)} & r_{pp}^{(n)} \end{bmatrix} \begin{bmatrix} \bar{a}_s \\ \bar{a}_p \end{bmatrix}, \qquad \begin{bmatrix} t_s^{(n)} \\ t_p^{(n)} \end{bmatrix} = \begin{bmatrix} t_{ss}^{(n)} & t_{sp}^{(n)} \\ t_{ps}^{(n)} & t_{pp}^{(n)} \end{bmatrix} \begin{bmatrix} \bar{a}_s \\ \bar{a}_p \end{bmatrix}, \tag{2.67}$$

where $r_{sp}^{(n)}$, etc., are reflection coefficients and $t_{sp}^{(n)}$, etc., are transmission coefficients. Co-polarized coefficients have both subscripts identical, but cross-polarized coefficients do not. Reflectances of nth order are determined as

$$R_{sp}^{(n)} = |r_{sp}^{(n)}|^2 \, \text{Re} \left[k_z^{(n)} / k_z^{(0)} \right], \tag{2.68}$$

etc., and transmittances likewise as

$$T_{\text{sp}}^{(n)} = |t_{\text{sp}}^{(n)}|^2 \operatorname{Re}\left[k_z^{(n)}/k_z^{(0)}\right],\qquad(2.69)$$

etc. The absorptance for *p*-polarized incident plane wave is

$$A_{\text{p}} = 1 - \sum_{n=-N_s}^{N_s}\left[R_{\text{sp}}^{(n)} + R_{\text{pp}}^{(n)} + T_{\text{sp}}^{(n)} + T_{\text{pp}}^{(n)}\right] \in [0,1],\qquad(2.70)$$

and that for *s*-polarized incident plane wave is

$$A_{\text{s}} = 1 - \sum_{n=-N_s}^{N_s}\left[R_{\text{ss}}^{(n)} + R_{\text{ps}}^{(n)} + T_{\text{ss}}^{(n)} + T_{\text{ps}}^{(n)}\right] \in [0,1].\qquad(2.71)$$

If both materials in the region $0 < z < L_t$ are non-dissipative, the principle of conservation of energy requires that $A_{\text{p}} = A_{\text{s}} = 0$.

2.2 Numerical Results and Discussion

The free space wavelength $\lambda_0 = 633$ nm was fixed for all data presented here. The CTF was taken to be made of tantalum oxide [7, 86] with permittivity given in Eq. (1.3) in Chap. 1. The vapor deposition angle $\chi_v = 20°$ was fixed for all data presented here. The metal was taken as silver with refractive index $n_m = \sqrt{\varepsilon_m} = 0.05096 + 3.92451i$. The dimensions $L = 900$ nm, $L_m = 30$ nm, and $L_g = 20$ nm were kept fixed for all calculations along with $\gamma = 15°$ and $\gamma = 30°$.

2.2.1 Canonical Boundary-Value Problem

In the underlying canonical boundary-value problem [3], the CTF occupies the half-space $z < 0$, the metal occupies the half-space $z > 0$, and the SPP wave propagates along the direction $\hat{\mathbf{u}}_x \cos\bar{\psi} + \hat{\mathbf{u}}_y \sin\bar{\psi}$. The complex-valued wavenumber q of the SPP wave is a function of $\bar{\psi}$ due to the anisotropy of the CTF, as has been shown elsewhere [122]. Only one value of q exists for each value of $\bar{\psi}$, which means that only one SPP wave can be excited for propagation in a direction specified by $\bar{\psi}$. Also, if an SPP wave is excited for a given value of $\bar{\psi} \in [0°, 90°]$, then it is also excited for $180° \pm \bar{\psi}$ and $360° - \bar{\psi}$. Fields in both partnering materials vary as $\exp[iq(x\cos\bar{\psi} + y\sin\bar{\psi}) + i\alpha z]$ with $\operatorname{Im}(\alpha) < 0$ in the CTF and $\operatorname{Im}(\alpha) > 0$ in metal so that the fields decay as $z \to \pm\infty$.

The symmetry of the problem enjoins the solutions of the dispersion equation [3, 12] for SPP-wave propagation to be identical for $\bar{\psi}$ and $180° \pm \bar{\psi}$. Furthermore, the morphologically significant plane of the CTF forms a natural reference plane. Hence, the focus here was on $\phi = \bar{\psi} - \gamma \in [0°, 90°]$, where ϕ is the angle subtended by the direction of propagation on the mor-
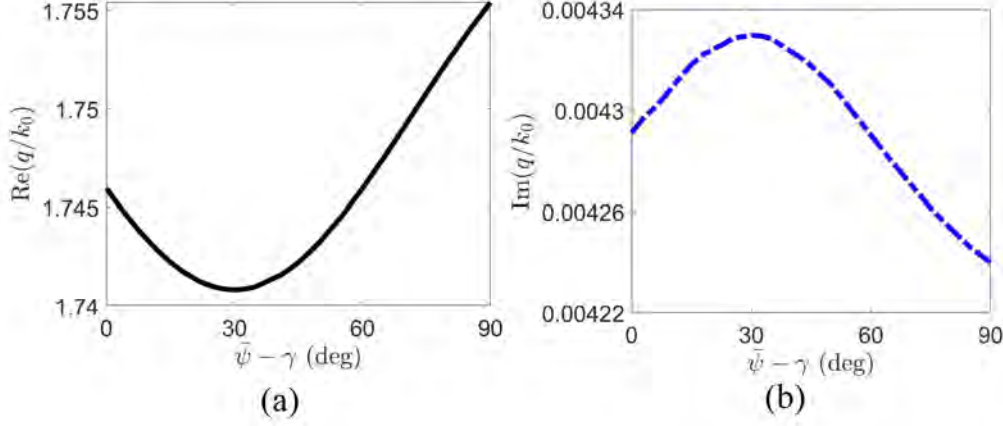
Figure 2.2: Real and imaginary parts of the normalized SPP wavenumber q/k_0 as functions of $\phi = \bar{\psi} - \gamma$ in the canonical boundary-value problem. The metal has relative permittivity $\varepsilon_{\mathrm{m}} = (0.05096 + 3.92451i)^2$ and the CTF is made of tantalum oxide [7, 86].

phologically significant plane. A combination of search and Newton–Raphson method [136] was employed to solve the dispersion equation for obtaining the complex-valued wavenumber q as a function of $\bar{\psi}$ for fixed γ. The Matlab™ program for finding the complex-valued wavenumber q is provided in Appendix A.1. It was assumed that $\varepsilon_{\mathrm{m}} = (0.05096 + 3.92451i)^2$ and $\lambda_0 = 633$ nm.

The real part and imaginary parts of the relative wavenumber q/k_0 are presented in Figs. 2.2(a) and 2.2(b), respectively, as functions of $\phi \in [0°, 90°]$. These figures show that SPP waves can exist for every $\phi \in [0°, 90°]$. In fact, it was found that the SPP waves can exist for propagation in any direction in the interface plane, i.e., $\bar{\psi} \in [0°, 90°]$.

2.2.2 Grating-Coupled Excitation

In the grating-coupled configuration, the in-plane component of the wave vector of the nth order of Floquet harmonic is given by $\hat{\mathbf{u}}_{\mathrm{x}} k_{\mathrm{x}}^{(n)} + \hat{\mathbf{u}}_{\mathrm{y}} k_{\mathrm{y}}^{(0)}$; it is clearly a function of θ and ψ. Whereas ψ is fixed by the direction of propagation of the incident plane wave, candidate values of θ for the excitation of an SPP wave are given by the locations of the peaks when the absorptances A_{p} and A_{s} are plotted as functions of θ. Only those absorptance peaks are acceptable candidates if their locations on the θ axis are independent of the thickness L_{c} of the CTF beyond a threshold. If the in-plane component of the wave vector of a Floquet harmonic for a specific peak thus identified then matches the wavenumber of an SPP wave obtained from the solution of the underlying canonical boundary-value problem, the excitation of the SPP wave in the grating-coupled configuration is confirmed. In other words, matching condition [130, 131]

$$\mathrm{Re}[q(\bar{\psi})]\left(\hat{\mathbf{u}}_{\mathrm{x}} \cos \bar{\psi} + \hat{\mathbf{u}}_{\mathrm{y}} \sin \bar{\psi}\right) = \hat{\mathbf{u}}_{\mathrm{x}} k_{\mathrm{x}}^{(n)}(\theta, \psi) + \hat{\mathbf{u}}_{\mathrm{y}} k_{\mathrm{y}}^{(0)}(\theta, \psi), \tag{2.72}$$

must be satisfied reasonably well for a specific pair $\{\bar{\psi}, n\}$ by a candidate absorption peak. When $|\bar{\psi} - \psi| \notin \{0°, 180°\}$, the direction of propagation of the SPP wave does not lie wholly in the plane of incidence. Let me also note that $\sin \psi = 0$ implies that $\sin \bar{\psi} = 0$ because the wavenumbers in Eqs. (2.72) can not be null valued. The thickness L_c was kept variable between 1000 and 3000 nm. Both A_p and A_s were calculated using a program implemented on the Matlab™ platform on an HP Spectre 360 laptop computer, for θ varying in steps of $0.1°$ and for ψ varying in steps $\geq 0.1°$. The Matlab™ program is provided in Appendix A.3. The $N_s = 10$ was fixed after checking that both absorptances converged with a tolerance limit of $\pm 0.1\%$. Furthermore, adherence to the principle of conservation of energy was tested by confirming that that $A_p = A_s = 0$ when all four of $\varepsilon_{\mathcal{A}_a}$, $\varepsilon_{\mathcal{A}_b}$, $\varepsilon_{\mathcal{A}_c}$, and ε_m are real and positive. Although A_p and A_s were calculated for $\theta \in [0°, 89°]$ and $\psi \in [0°, 90°]$, data are presented here only for smaller ranges of θ in which the excitation of an SPP wave in the grating-coupled configuration was confirmed.

2.2.2.1 *p*-Polarized Incident Plane Wave

$\psi = 0°$

Figure 2.3(a) shows angular spectra the absorptance A_p (i.e., the variations of these absorptance with the polar angle of incidence θ) for three different values of the CTF thickness L_c when the plane of incidence coincides with the grating plane (i.e., $\psi = 0°$) and $\gamma = 15°$. These plots exemplify the excitation of the same SPP wave for three different values of θ. The first excitation occurs at $\theta_1 \simeq 19.2°$, regardless of $L_c \geq 1000$ nm, when the in-plane wavenumber $k_{xy}^{(2)} = 1.7355 k_0$ of the Floquet harmonic of order $n = 2$ matches the canonical solution $\mathrm{Re}[q(\bar{\psi}_1)] = 1.7422 k_0$ at $\bar{\psi}_1 = 0°$. This is in accord with Eq. (2.72) which mandates $\bar{\psi} = \psi$ and $n > 0$ when $\psi = 0°$. The second excitation occurs at $\theta_2 \simeq 21.7°$, regardless of $L_c \geq 1000$ nm, when $k_{xy}^{(-3)} = 1.7403 k_0$ matches $\mathrm{Re}[q(\bar{\psi}_2)] = 1.7422 k_0$ at $\bar{\psi}_2 = 180°$. This is in accord with Eq. (2.72), whereby $\bar{\psi} = 180° + \psi$ and $n < 0$ when $\psi = 0°$. In the canonical problem, the same SPP wave is excited for $\bar{\psi}_1$ and $\bar{\psi}_2 = 180° + \bar{\psi}_1$. The third excitation occurs at $\theta_3 \simeq 24°$, when $k_{xy}^{(-3)} = 1.7033 k_0$ matches $\mathrm{Re}[q(\bar{\psi}_3)] = 1.7422 k_0$ at $\bar{\psi}_3 = 180°$, again in accord with Eq. (2.72).

The situation is similar in Fig. 2.3(b) for the excitation of an SPP wave at three angular locations when $\gamma = 30°$. The canonical problem yields $\mathrm{Re}[q(\bar{\psi})] = 1.7459 k_0$ for $\bar{\psi} \in \{0°, 180°\}$. The figure demonstrates the excitation of the SPP wave, first at $\theta_1 \simeq 19.8°$, when the in-plane wavenumber $k_{xy}^{(2)} = 1.7454 k_0$, second at $\theta_2 \simeq 21.7°$ when the in-plane wavenumber $k_{xy}^{(-3)} = 1.7403 k_0$, as a Floquet harmonic of order $n = 2$ and $n = -3$, respectively, matches the canonical solution. The third excitation occurs at $\theta_3 \simeq 23.8°$ as a Floquet harmonic of order $n = -3$ because a $k_{xy}^{(-3)} = 1.7065 k_0$ matches $\mathrm{Re}[q(\bar{\psi}_3)] = 1.7459 k_0$.

It was conclude that multiple excitation of an SPP wave, previously demonstrated for $\gamma = 0°$ [13], can occur even when the morphologically significant plane of the CTF does not coincide with the grating plane.

The absorptance plots in Fig. 2.3(a) and Fig. 2.3(b) indicate that the excitations of the SPP

Figure 2.3: Absorptance A_p as a function of incidence angle θ for $L_c \in \{1000, 2000, 3000\}$ nm, when $\chi_v = 20°$, $\psi = 0°$, $L = 900$ nm, and $L_m = 30$ nm. (a) $\gamma = 15°$, and (b) $\gamma = 30°$. A downward arrow identifies the excitation of an SPP wave as a Floquet harmonic of order n, which is indicated alongside the arrow.

wave are stronger at θ_1 and θ_2 than at θ_3. This conclusion is also supported by the differences $\left| k_{xy}^{(2)}(\psi_1) - \mathrm{Re}\left[q(\bar{\psi}_1)\right] \right|$ and $\left| k_{xy}^{(-3)}(\psi_2) - \mathrm{Re}\left[q(\bar{\psi}_2)\right] \right|$ being smaller that $\left| k_{xy}^{(-3)}(\psi_3) - \mathrm{Re}\left[q(\bar{\psi}_3)\right] \right|$.

$\psi = 30°$

The foregoing calculations were repeated for $\gamma = 15°$ and $\psi = 30°$. Now the plane of incidence does not coincide with the grating plane. The plots in Fig. 2.4(a) illustrate the excitation of an SPP wave for three different values of θ. The first excitation occurs at $\theta_1 \simeq 21.3°$, regardless of $L_c \geq 1000$ nm, when the in-plane wavenumber $k_{xy}^{(2)} = 1.7308k_0$ of the Floquet harmonic of order $n = 2$ matches the canonical solution $\mathrm{Re}[q(\bar{\psi}_1)] = 1.7413k_0$ at $\bar{\psi}_1 = 6.0235°$, in accord with Eq. (2.72). The second excitation occurs at $\theta_2 \simeq 24°$, when $k_{xy}^{(-3)} = 1.7695k_0$ matches $\mathrm{Re}[q(\bar{\psi}_2)] = 1.7436k_0$ at $\bar{\psi}_2 = 173.4004°$. The third excitation occurs at $\theta_3 \simeq 26.8°$, when $k_{xy}^{(-3)} = 1.7342k_0$ matches $\mathrm{Re}[q(\bar{\psi}_3)] = 1.7438k_0$ at $\bar{\psi}_3 = 172.5308°$.

The plots in Fig. 2.4(b) illustrate the excitation of an SPP wave for three different values of θ for $\gamma = 30°$. The first excitation occurs at $\theta_1 \simeq 21.5°$, regardless of $L_c \geq 1000$ nm, when the in-plane wavenumber $k_{xy}^{(2)} = 1.7338k_0$ of the Floquet harmonic of order $n = 2$ matches the canonical solution $\mathrm{Re}[q(\bar{\psi}_1)] = 1.7442k_0$ at $\bar{\psi}_1 = 6.0672°$, in accord with Eq. (2.72). The second excitation occurs at $\theta_2 \simeq 24°$, when $k_{xy}^{(-3)} = 1.7695k_0$ matches $\mathrm{Re}[q(\bar{\psi}_2)] = 1.7480k_0$ at $\bar{\psi}_2 = 173.4004°$. The third excitation occurs at $\theta_3 \simeq 26.1°$, when $k_{xy}^{(-3)} = 1.7429k_0$ matches $\mathrm{Re}[q(\bar{\psi}_3)] = 1.7482k_0$ at $\bar{\psi}_3 = 172.7496°$. Given the small difference between $180° - \bar{\psi}_1$, $\bar{\psi}_2$, and $\bar{\psi}_3$, the SPP waves excited at θ_1, θ_2, and θ_3 have quantitatively close but not identical attributes.

Figure 2.4: Absorptance A_p as a function of incidence angle θ for $L_c \in \{1000, 2000, 3000\}$ nm, when $\chi_v = 20°$, $\psi = 30°$, $L = 900$ nm, and $L_m = 30$ nm. (a) $\gamma = 15°$, and (b) $\gamma = 30°$. A downward arrow identifies the excitation of an SPP wave as a Floquet harmonic of order n, which is indicated alongside the arrow.

$\psi > 30°$

Figure 2.5(a) provides evidence of SPP-wave excitation at $\theta_1 \simeq 64.05°$, when $\psi = 89.5°$ and $\gamma = 15°$. This SPP wave is excited as a Floquet harmonic of order $n = 2$ because $k_{xy}^{(2)} = 1.6761k_0$ matches $\mathrm{Re}[q(\bar{\psi}_1)] = 1.7426k_0$ at $\bar{\psi}_1 = 32.4423°$.

Figure 2.5: Absorptance A_p as a function of incidence angle θ for $L_c \in \{1000, 2000, 3000\}$ nm, when $\chi_v = 20°$, $L = 900$ nm, and $L_m = 30$ nm. (a) $\gamma = 15°$, $\psi = 89.5°$, and (b) $\gamma = 30°$ and $\psi = 88.1°$. A downward arrow identifies the excitation of an SPP wave as a Floquet harmonic of order n, which is indicated alongside the arrow.

Figure 2.5(b) provides evidence of SPP-wave excitation at $\theta_1 \simeq 66.1°$, when $\psi = 88.1°$ and $\gamma = 30°$. This SPP wave is excited as a Floquet harmonic of order $n = 2$ because $k_{xy}^{(2)} = 1.7029k_0$

matches $\mathrm{Re}[q(\bar{\psi}_1)] = 1.7409k_0$ at $\bar{\psi}_1 = 32.4516°$. No SPP wave was found to be excited for $\psi \in (89.5°, 90°]$ when $\gamma = 15°$, and $\psi \in (88.1°, 90°]$ when $\gamma = 30°$.

2.2.2.2   *s*-Polarized Incident Plane Wave

$\psi = 0°$

No depolarization can occur when the incidence plane is congruent with the morphologically significant plane of the CTF, i.e, when $\gamma = \psi$. Having fixed $\gamma = 0°$ and $\psi = 0°$, Chiadini *et al.* [13] therefore they did not have to consider the excitation of an SPP wave due to illumination by an *s*-polarized incident plane wave. However, depolarization will occur if $\gamma \neq \psi$ [2, 36], as confirmed for the grating-coupled configuration of Fig. 3.1. Therefore, the evidence were found for the excitation of SPP waves by *s*-polarized illumination for $\psi = 0°$ and either $\gamma = 15°$, or $\gamma = 30°$. Figure 2.3(a) provides evidence of SPP-wave excitation at $\theta_1 = 19.2°$, $\theta_2 = 21.7°$, and $\theta_3 = 24°$ due to *p*-polarized illumination.
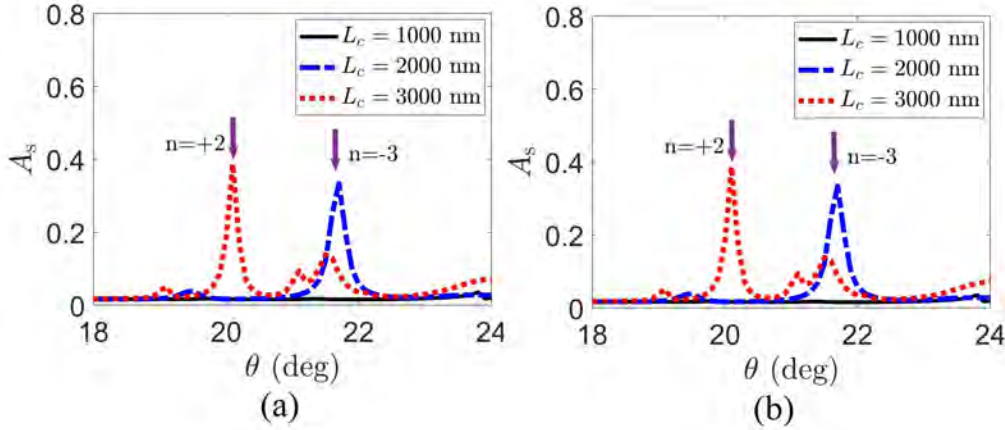
Figure 2.6: Absorptance A_s as a function of incidence angle θ for $L_c \in \{1000, 2000, 3000\}$ nm, when $\chi_\mathrm{v} = 20°$, $\psi = 0°$, $L = 900$ nm, and $L_\mathrm{m} = 30$ nm. (a) $\gamma = 15°$ and (b) $\gamma = 30°$. A downward arrow identifies the excitation of an SPP wave as a Floquet harmonic of order n, which is indicated alongside the arrow.

Figure. 2.6(a) contains A_s-peaks for SPP-wave excitation at $\theta_1 = 20.1°$ (when $L_\mathrm{c} = 3000$ nm) and $\theta_2 = 21.7°$, but not at θ_3, for *s*-polarized illumination. Figure 2.3(b) provides evidence of SPP-wave excitation at $\theta_1 = 19.8°$, $\theta_2 = 21.7°$, and $\theta_3 = 23.8°$ due to *p*-polarized illumination. These values of θ are also candidates for SPP-wave excitation due to *s*-polarized illumination. Indeed, Fig. 2.6(b) contains A_s-peaks for SPP-wave excitation at θ_1 (when $L_\mathrm{c} = 3000$ nm) and θ_2, but not at θ_3, for *s*-polarized illumination. Comparison of Figs. 2.3 and 2.6 suggests that *s*-polarized illumination excites weaker SPP waves than *p*-polarized illumination, which may explain the very low values of A_s at θ_3.

$\psi = 30°$

Figure 2.7(a) shows the absorptance spectrum A_s for three different values of the CTF thickness Lc when $\gamma = 15°$. This figures demonstrates the first excitation of an SPP wave at $\theta_1 \simeq 22.1°$, regardless of $L_c \geq 1000$ nm, when the in-plane wavenumber $k_{xy}^{(2)} = 1.7427k_0$ of the Floquet harmonic of order $n = 2$ matches the canonical solution $\text{Re}[q(\bar{\psi}_1)] = 1.7413k_0$ at $\bar{\psi}_1 = 6.1969°$. The second excitation of an SPP wave occurs at $\theta_2 \simeq 23.9°$ when the in-plane wavenumber $k_{xy}^{(2)} = 1.7692k_0$ of the Floquet harmonic of order $n = 2$ matches the canonical solution $\text{Re}[q(\bar{\psi}_2)] = 1.7412k_0$ at $\bar{\psi}_2 = 6.5748°$. The third excitation occurs at $\theta_3 \simeq 26.2°$ when $k_{xy}^{(-3)} = 1.7417k_0$ is close to the canonical solution $\text{Re}[q(\bar{\psi}_3)] = 1.7437k_0$ at $\bar{\psi}_3 = 172.7184°$. The fourth excitation takes place at $\theta_4 \simeq 28.9°$ when $k_{xy}^{(-3)} = 1.7086k_0$ matches $\text{Re}[q(\bar{\psi}_4)] = 1.7439k_0$ at $\bar{\psi}_4 = 171.8698°$.
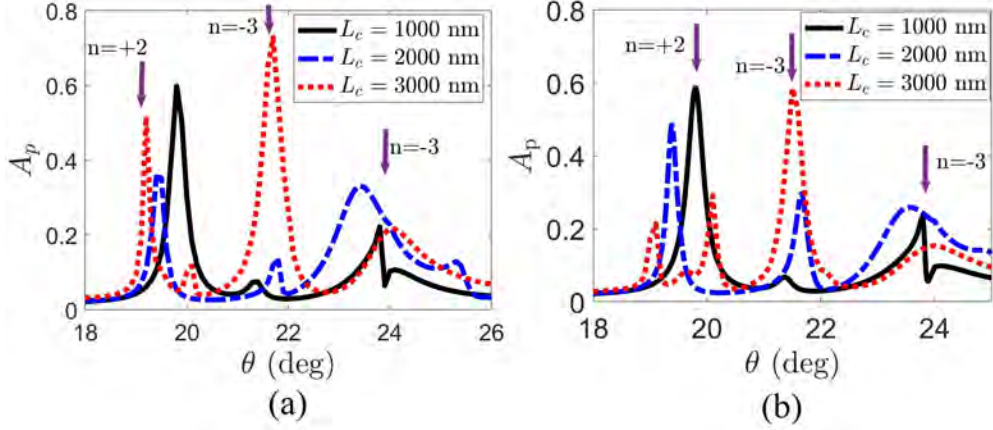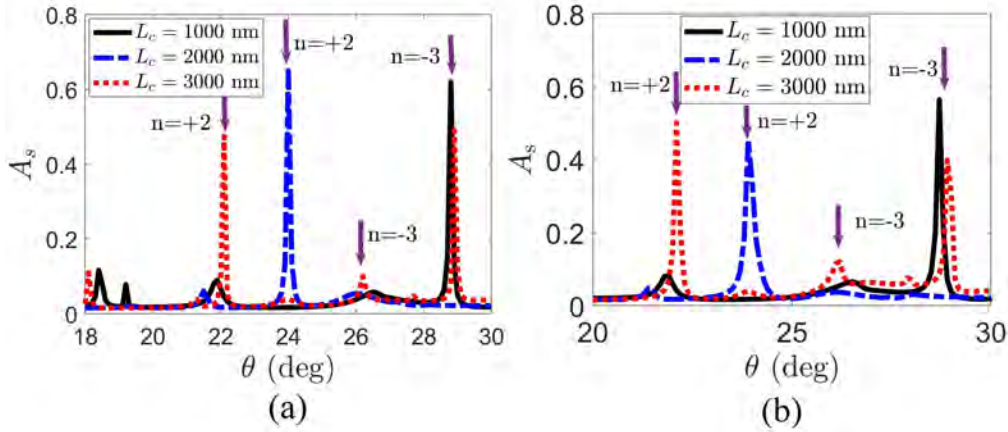

Figure 2.7: Absorptance A_s as a function of incidence angle θ for $L_c \in \{1000, 2000, 3000\}$ nm, when $\chi_v = 20°$, $\psi = 30°$, $L = 900$ nm, and $L_m = 30$ nm. (a) $\gamma = 15°$ and (b) $\gamma = 30°$. A downward arrow identifies the excitation of an SPP wave as a Floquet harmonic of order n, which is indicated alongside the arrow.

Figure 2.7(b) shows the absorptance A_s as a function of θ for three different values of the CTF thickness Lc when $\gamma = 30°$. Figure 2.7(b) provides evidence of SPP-wave excitation at $\theta_1 \simeq 22.1°$, $\theta_2 \simeq 23.9°$, $\theta_3 \simeq 26.2°$, and $\theta_4 \simeq 28.9°$ regardless of $L_c \geq 1000$ nm, with the canonical solution $\text{Re}[q(\bar{\psi}_1)] = 1.7442k_0$, $\text{Re}[q(\bar{\psi}_2)] = 1.7386k_0$, $\text{Re}[q(\bar{\psi}_3)] = 1.7482k_0$, and $\text{Re}[q(\bar{\psi}_4)] = 1.7485k_0$, respectively. Figure 2.7(b) provides evidence of SPP-wave excitation excitation at the same angular locations as in Fig. 2.7(a) except the fact that s-polarized illumination excites stronger SPP waves for $\gamma = 15°$ than $\gamma = 30°$.

A comparison of Figs. 2.4 and 2.7 shows that s-polarized illumination can excite four SPP waves, whereas p-polarized illumination can excite three SPP waves, as θ is swept from $0°$ to $90°$. Also, the values of θ_1 to θ_3 are different for the two different polarization states of illumination. Both differences highlight the role of depolarization that must occur in the CTF

due to its anisotropy.

$\psi > 30°$

The plots of A_s versus θ in Fig. 2.8(a) for $\psi = 89.5°$ when $\gamma = 15°$ illustrate the excitation of an SPP wave at $\theta_1 \simeq 63.7°$, when the in-plane wavenumber $k_{xy}^{(2)} = 1.6746k_0$ of the Floquet harmonic of order $n = 2$ matches the canonical solution $\mathrm{Re}[q(\bar{\psi}_1)] = 1.7426k_0$ at $\bar{\psi}_1 = 32.3650°$.
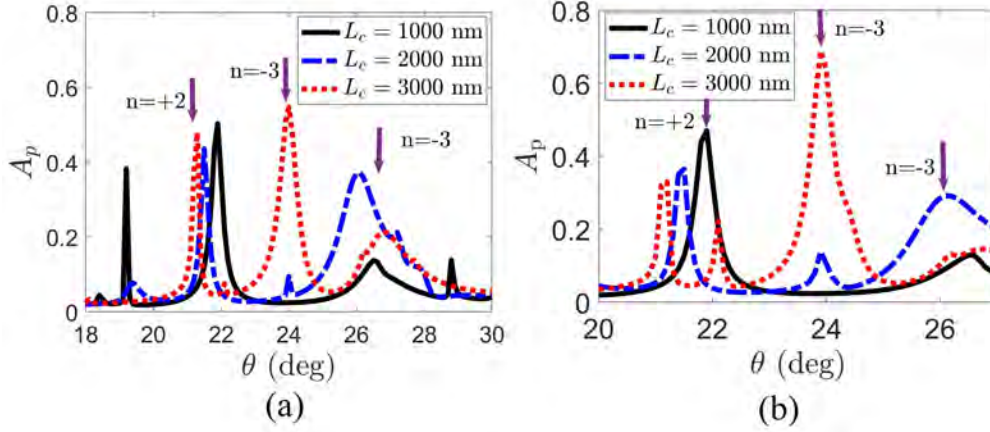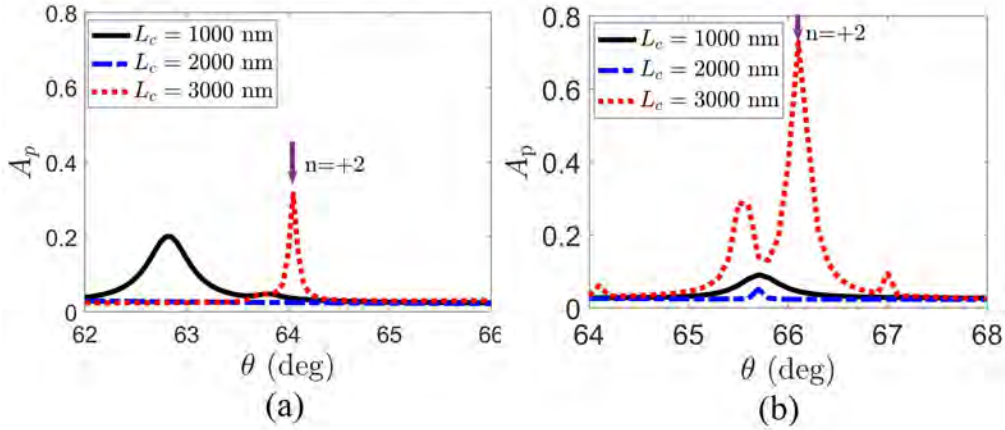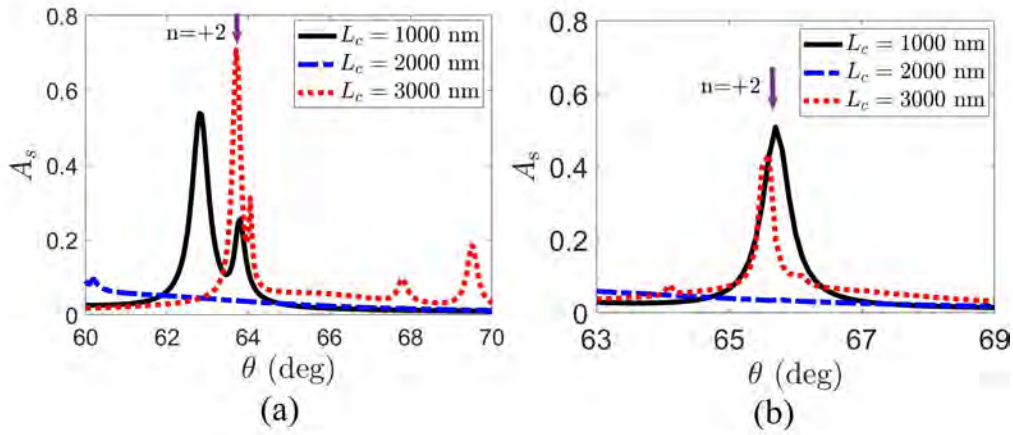

Figure 2.8: Absorptance A_s as a function of incidence angle θ for $L_c \in \{1000, 2000, 3000\}$ nm, when $\chi_v = 20°$, $L = 900$ nm, and $L_m = 30$ nm. (a) $\gamma = 15°$ and $\psi = 89.5°$, (b) $\gamma = 30°$ and $\psi = 88.1°$. A downward arrow identifies the excitation of an SPP wave as a Floquet harmonic of order n, which is indicated alongside the arrow.

Figure 2.8(b) examplify the excitation of an SPP wave for $\psi = 88.1°$ when $\gamma = 30°$. The SPP wave is excited at $\theta_1 \simeq 65.7°$, when the in-plane wavenumber $k_{xy}^{(2)} = 1.7013k_0$ of the Floquet harmonic of order $n = 2$ matches the canonical solution $\mathrm{Re}[q(\bar{\psi}_1)] = 1.7409k_0$ at $\bar{\psi}_1 = 32.3724°$. The excitation of SPP wave for $\gamma = 30°$ is weaker than the excitation of SPP wave for $\gamma = 15°$.

No SPP wave was found to be excited for $\psi \in (89.5°, 90°]$ when $\gamma = 15°$, and $\psi \in (88.1°, 90°]$ when $\gamma = 30°$.

2.3   Conclusions

The excitation of SPP waves by plane-wave illumination of a one-dimensional metallic surface-relief grating coated with a homogeneous biaxial dielectric material was theoretically investigated. The grating profile was taken to be invariant along a fixed axis. The plane of incidence could be different from the grating plane. The biaxial dielectric material was taken to be a CTF whose morphologically significant plane could differ from the grating plane as well as the

plane of incidence. The RCWA was adopted to solve the boundary-value problem to calculate the plane-wave absorptance as a function of the incidence direction, the orientation of the morphologically significant plane, and the linear polarization state of the illuminating plane wave. The following conclusions emerged from our numerical studies:

- Only p-polarized plane waves excite SPP waves, if both the plane of incidence and the morphologically significant plane of the CTF are congruent with the grating plane [13].

- Both p-polarized and s-polarized plane waves can excite SPP waves, provided that either the plane of incidence and/or the morphologically significant plane of the CTF do not coincide with the grating plane.

- No, one, or multiple SPP-wave excitations are possible for a fixed direction of propagation of the incident plane wave.

- The propensity for multiple excitation decreases as the incidence direction becomes normal to the grating plane, i.e., as ψ increases towards $90°$.

- The direction of propagation of an SPP wave excited may not wholly lie in the plane of incidence.

Chapter 3

Excitation of Dyakonov Surface Waves

A Dyakonov surface wave is guided by the interface of two homogeneous dielectric materials of which at least one is anisotropic. The excitation of any surface wave requires the matching of the wavenumber of that surface wave with the magnitude of the component of the wave vector of the incident light parallel to the interface plane. The Dyakonov surface waves have been experimentally observed in prism-coupled configuration [50]. In the prism-coupled configuration, the matching happens for a very narrow range of the incidence angle, when both partnering materials have either small or negligible dissipation. However, in the grating-coupled configuration [3], the matching can happen at more than one value of the incidence angle [13, 135] since diffraction from a grating comprises a multiplicity of non-specular Floquet harmonics [97]. Additionally, the grating-coupled configuration removes the need for a high-refractive-index material to couple incident light to surface waves. Therefore, the theoretically investigate was set out ti find the excitation of Dyakonov surface waves using grating-coupled configuration of an isotropic dielectric material and a biaxial dielectric material. The biaxial material was chosen to be a columnar thin film (CTF).

In this chapter, to fully understand the excitation of Dyakonov surface waves in the grating-coupled configuration, a very general setting possible for a CTF deposited over a one-dimensional grating has been used. The plane of incidence, the morphologically significant plane of the CTF, and the grating plane are taken to be arbitrarily oriented with respect to each other. The absorptance is computed using the rigorous coupled-wave approach (RCWA) [3, 14, 15] used in Chap. 2. Note that the mathematical formulation of the Dyakonov surface wave excitation is isomorphic to the SPP-wave excitation, therefore, the theory for the Dyakonov surface wave is

omitted here. The plan of the chapter is as follows: the boundary-value problem is described in Sec. 3.1, and numerical results are presented and discussed in Sec. 3.2. Conclusions are presented in Sec. 3.3.

3.1   Boundary-Value Problem

A schematic of the boundary-value problem is shown in Fig. 3.1. The region $0 < z < L_c$ is occupied by a CTF, the region $L_c + L_g < z < L_t$ by a homogeneous isotropic dielectric material of relative permittivity ε_d, and the half-spaces $z < 0$ and $z > L_t$ are occupied by air, where $L_t = L_c + L_g + L_d$. The intermediate region $L_c < z < L_c + L_g$ is occupied by a one-dimensional dielectric grating with the CTF assumed to fully occupy the troughs of the grating. The xz plane is the grating plane with L being the spatial period along the x axis. The interface $z = 0$
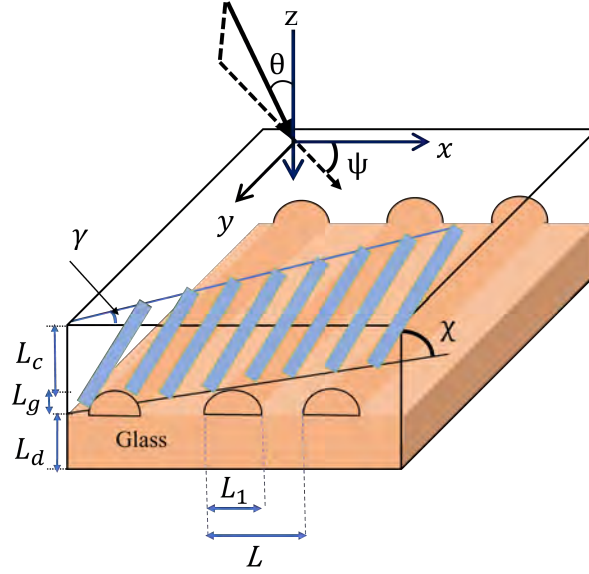
Figure 3.1: Schematic of the boundary-value problem solved for the grating-coupled configuration. Only the nanocolumns of the CTF in its morphologically significant plane are depicted.

is considered to be illuminated by a plane wave propagating at the polar angle θ (with respect to the z axis) and the azimuthal angle ψ (with respect to the x axis in the xy plane). Thus, the plane of incidence is jointly defined by the unit vectors $\hat{\mathbf{u}}_x \cos\psi + \hat{\mathbf{u}}_y \sin\psi$ and $\hat{\mathbf{u}}_z$. The electric and magnetic field phasors in the region $0 < z < L_t$ are expanded in terms of specular and non-specular Floquet harmonics with unknown coefficients [3, 14, 15]. The theoretical formulation of the boundary-value problem using the rigorous coupled-wave approach (RCWA) is explained in detail in Chap. 2, and is not repeated in this chapter.

3.2 Numerical Results and Discussion

3.2.1 Canonical Boundary-Value Problem

Before presenting the results for the grating-coupled configuration, the results of the underlying canonical boundary-value problem of Dyakonov surface waves guided by the planar interface of a CTF and an isotropic dielectric material occupying half-spaces on either side of that interface [3, 12] are presented. Theory for the canonical boundary-value problem has already been discussed in Chap. 1. Let the Dyakonov surface wave propagate in the interface plane parallel to the unit vector $\hat{\mathbf{u}}_x \cos \bar{\psi} + \hat{\mathbf{u}}_y \sin \bar{\psi}$. Then the surface wavenumber $q \equiv q(\bar{\psi})$ depends on the direction of propagation. Fields in both partnering materials vary as $\exp[iq(x \cos \bar{\psi} + y \sin \bar{\psi}) + i\alpha z]$ with $\mathrm{Im}(\alpha) < 0$ in the CTF and $\mathrm{Im}(\alpha) > 0$ in the isotropic dielectric material so that the fields decay as $z \to \pm\infty$. It was assumed that $\varepsilon_d = (1.5 + 0.001i)^2$ and $\lambda_0 = 633$ nm. The code for the program is provided in Appendix A.4.

The real and imaginary parts of the relative wavenumber q/k_0 are presented in Figs. 3.2(a) and 3.2(b), respectively, as functions of $\phi \in [0, 90°]$ for different values of χ_v. These figures show that Dyakonov surface waves can exist for $\phi \in [23.1°, 34°)$, $\phi \in [38.7°, 65.7°]$, and $\phi \in [37.9°, 90°]$, respectively for $\chi_v = 20°$, $\chi_v = 25°$, and $\chi_v = 30°$. However, for $\chi_v = 40°$ and $\chi_v = 45°$, Dyakonov surface waves can exist for every $\phi \in [0°, 90°]$. In fact, the Dyakonov surface waves can exist for propagation in any direction in the interface plane, i.e., $\bar{\psi} \in [0°, 90°]$, when $\chi_v \geq 35.1°$. Thus, the angular existence domain (AED), i.e., the admissible range of ψ, of Dyakonov surface waves can be very large, not surprisingly because $\mathrm{Im}(\varepsilon_d) > 0$ even though it is much smaller than $\mathrm{Re}(\varepsilon_d)$.
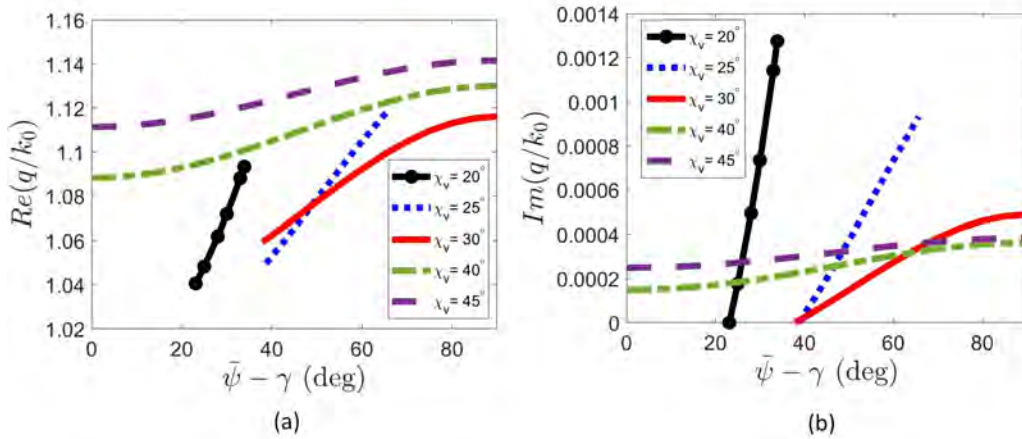
Figure 3.2: Real and imaginary parts of the normalized Dyakonov surface wavenumber q/k_0 as functions of $\bar{\psi} - \gamma$ in the canonical boundary-value problem for various values of the collimated vapor flux angle χ_v of the CTF. The isotropic dielectric partner has relative permittivity $\varepsilon_d = (1.5 + 0.001i)^2$ and the CTF is made of tantalum oxide [7, 86].

3.2.2 Grating-Coupled Excitation

The absorptance

$$A_{\rm p} = 1 - \sum_{n=-N_t}^{N_t} \left[R_{\rm sp}^{(n)} + R_{\rm pp}^{(n)} + T_{\rm sp}^{(n)} + T_{\rm pp}^{(n)} \right] \in [0,1], \tag{3.1}$$

for a p-polarized incident plane wave with $a_{\rm s}^{(n)} = 0$ and $a_{\rm p}^{(n)} = \delta_{n0}$ and the absorptance

$$A_{\rm s} = 1 - \sum_{n=-N_t}^{N_t} \left[R_{\rm ss}^{(n)} + R_{\rm ps}^{(n)} + T_{\rm ss}^{(n)} + T_{\rm ps}^{(n)} \right] \in [0,1] \tag{3.2}$$

for a s-polarized incident plane wave with $a_{\rm p}^{(n)} = 0$ and $a_{\rm s}^{(n)} = \delta_{n0}$.

To delineate the excitation of Dyakonov surface waves, both absorptances $A_{\rm s}$ and $A_{\rm p}$ are computed as functions of θ for various thicknesses $L_{\rm c}$ and $L_{\rm d}$ of the two partnering dielectric materials, with ψ, γ, L, $L_{\rm g}$, $\chi_{\rm v}$, $\varepsilon_{\rm d}$, and λ_0 fixed. Then those thickness-independent absorptance peaks are identified whose angular location (on the θ axis) matches a prediction from the canonical problem. This match is nontrivial as the direction of propagation of the Dyakonov surface wave (given by angle $\bar{\psi}$ with respect to the x axis) in the interface plane does not necessarily lie in the incidence plane that makes an angle ψ with respect to the xz plane because of the existence of nonspecular Floquet harmonics unless $\sin\psi = 0$. Therefore, the real part of the Dyakonov surface wavenumber for some admissible $\bar{\psi}$ has to match the in-plane wavenumber of one of the Floquet harmonics. Thus, the matching conditions [130, 131, 135]

$$\left. \begin{aligned} {\rm Re}[q(\bar{\psi})]\cos\bar{\psi} &= k_0 \sin\theta\cos\psi + 2n\pi/L \\ {\rm Re}[q(\bar{\psi})]\sin\bar{\psi} &= k_0 \sin\theta\sin\psi \end{aligned} \right\} \tag{3.3}$$

must be satisfied reasonably well for a specific pair $\{\bar{\psi}, n\}$ by a candidate absorption peak for the fixed ψ and γ. The in-plane wavenumber of the Floquet harmonic of order n is given by

$$k_{\rm xy}^{(n)} = +\sqrt{k_0^2 \sin^2\theta + (2n\pi k_0/L)\cos\psi\sin\theta + (2n\pi/L)^2}. \tag{3.4}$$

For representative results, $\chi_{\rm v} = 20°$, $L = 500$ nm and $L_{\rm g} = 50$ nm were fixed. Then, the absorptances $A_{\rm p}$ and $A_{\rm s}$ were computed for four combinations of $L_{\rm c}$ and $L_{\rm d}$ with $\gamma = 15°$ fixed. The calculated absorptances are provided as functions of θ in Figs. 3.3 and 3.4 for p- and s-polarized incident plane waves, respectively. Whereas $\psi = 35°$ for Fig. 3.3(a), $\psi = 37°$ for Fig. 3.3(b), and $\psi = 46°$ for Fig. 3.3(c) for p-polarized incident plane wave. For s-polarized incident plane waves $\psi = 39.7°$ for Fig. 3.4(a) and $\psi = 44°$ for Fig. 3.4(b). All expansions in RCWA were truncated to include only $n \in [-10, 10]$ (i.e., $N_{\rm s} = 10$), after checking that both $A_{\rm p}$ and $A_{\rm s}$ converged with maximum tolerance limit of $\pm 0.1\%$. Figure 3.3(a) shows the excitation of a Dyakonov surface wave at $\theta_1 \simeq 18.9°$ when $\psi = 35°$, because the $A_{\rm p}$-peak is indepen-

dent of the chosen values of L_c and L_d, and the in-plane wavenumber $k_{xy}^{(-1)} = 1.0178k_0$ of the Floquet harmonic of order $n = -1$ matches the canonical solution $\text{Re}[q(\bar{\psi}_1)] = 1.0506k_0$ at $\bar{\psi}_1 = 169.5°$, i.e., $\phi \in \{25.5°, 154.5°\}$. The other peaks present in Fig. 3.3(a) represent waveguide modes [27, 133] because their angular locations are dependent upon on the thicknesses of the isotropic and the anisotropic dielectric partnering materials; furthermore, their angular locations do not satisfy Eq. (3.3).

Figure 3.3(b) shows the excitation of a Dyakonov surface wave as a Floquet harmonic of order $n = -1$ at two different values of θ. The first excitation of a Dyakonov surface wave at $\theta_1 \simeq 19.4°$ when $\psi = 37°$, because the A_p-peak is independent of the chosen values of L_c and L_d, and the in-plane wavenumber $k_{xy}^{(-1)} = 1.0205k_0$ of the Floquet harmonic of order $n = -1$ matches the canonical solution $\text{Re}[q(\bar{\psi}_1)] = 1.0540k_0$ at $\bar{\psi}_1 = 168.7°$, i.e., $\phi \in \{26.3°, 153.7°\}$. The second Dyakonov surface wave is excited at $\theta_2 \simeq 20.8°$ when $\psi = 37°$, where the in-plane wavenumber $k_{xy}^{(-1)} = 1.0054k_0$ of the Floquet harmonic of order $n = -1$ matches the canonical solution $\text{Re}[q(\bar{\psi}_2)] = 1.0585k_0$ at $\bar{\psi}_2 = 167.7°$, i.e., $\phi \in \{27.3°, 152.7°\}$. Figure 3.3(b) shows that Dyakonov waves of same order of the Floquet harmonic is excited for different values of θ.

Figure 3.3(c) shows the excitation of a Dyakonov surface wave at two different values of θ when $\psi = 46°$. The first excitation occurs at $\theta_1 \simeq 16.8°$, because the A_p-peak is independent of the chosen values of L_c and L_d, and the in-plane wavenumber $k_{xy}^{(-1)} = 1.0853k_0$ matches the canonical solution $\text{Re}[q(\bar{\psi}_1)] = 1.0529k_0$ at $\bar{\psi}_1 = 169°$, i.e., $\phi \in \{26°, 154°\}$. The second excitation occurs at $\theta_2 \simeq 21.8°$, when $k_{xy}^{(-1)} = 1.0428k_0$ matches the canonical solution $\text{Re}[q(\bar{\psi}_2)] = 1.0710k_0$ at $\bar{\psi}_2 = 165.2°$, i.e., $\phi \in \{29.8°, 150.2°\}$. Since the values of q are significantly different for the two excitations, it can not be considered that the same Dyakonov surface wave has been excited twice. Excitation of different Dyakonov surface waves for the same value of the azimuthal angle by varying the polar angle was also found for some other values of ψ. From similar calculations for other values of ψ (for the same value of γ), it was found that Dyakonov surface waves can be excited by p-polarized illumination for all $\psi \in [33°, 47°]$, but not for values of ψ outside of this interval. Also, note that all three peaks in Fig. 3.3 identified with the excitation of Dyakonov surface waves change their angular locations slightly when the thicknesses of the partnering materials are changed, because of the interaction of the three bimaterial interfaces. With $\text{Re}[q(\bar{\psi})]$ exceeding k_0, each Dyakonov surface wave spills evanescent fields into the two half-spaces occupied by air.

Excitation of Dyakonov surface waves by s-polarized incident plane waves was identified using the same method as described for p-polarized incidence. Figure 3.4(a) demonstrates the excitation of a Dyakonov surface wave at $\theta_1 \simeq 16.05°$ when $\psi = 39.7°$, because the A_s-peak is independent of L_c and L_d, and the in-plane wavenumber $k_{xy}^{(-1)} = 1.0680k_0$ of the Floquet harmonic of order $n = -1$ matches the canonical solution $\text{Re}[q(\bar{\psi}_1)] = 1.0463k_0$ at $\bar{\psi}_1 = 170.5°$, i.e., $\phi \in \{24.5°, 155.5°\}$. Figure 3.4(b) demonstrates the excitation of a Dyakonov surface wave at $\theta_1 \simeq 16.9°$ when $\psi = 44°$, and the in-plane wavenumber $k_{xy}^{(-1)} = 1.0760k_0$ of the Floquet
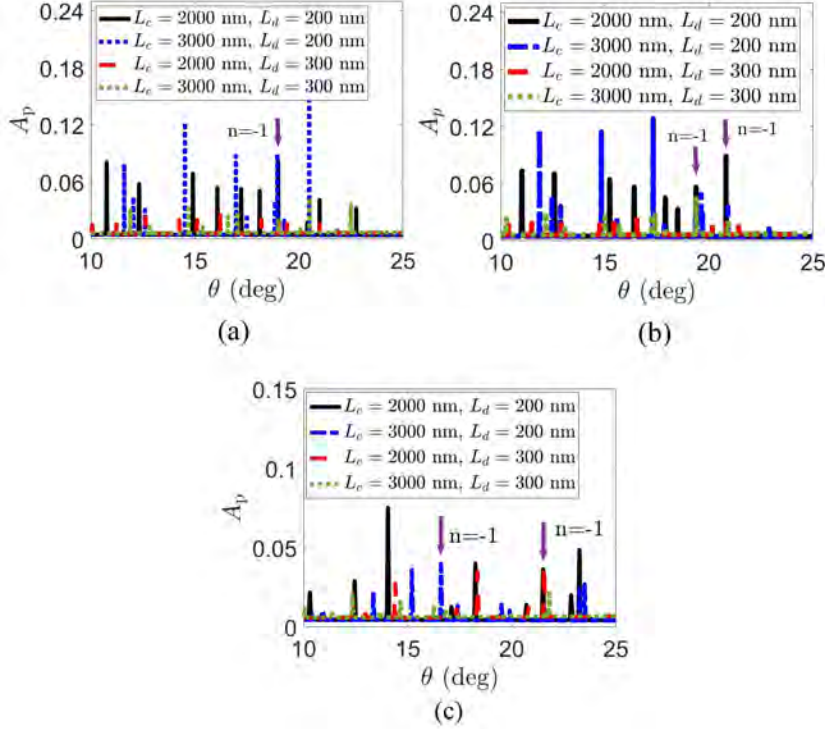
Figure 3.3: Absorptance A_p as a function of incidence angle θ for $L_c \in \{2000, 3000\}$ nm and $L_d \in \{200, 300\}$ nm in the grating-coupled configuration, when $\gamma = 15°$, $\chi_v = 20°$, $L = 500$ nm, and $L_g = 50$ nm. (a) $\psi = 35°$, (b) $\psi = 37°$, and (c) $\psi = 46°$. A downward arrow identifies the peak that indicates the excitation of a Dyakonov surface wave as a Floquet harmonic of order n, which is indicated alongside the arrow.

harmonic of order $n = -1$ matches the canonical solution $\mathrm{Re}[q(\bar{\psi}_1)] = 1.0519 k_0$ at $\bar{\psi}_1 = 169.2°$, i.e., $\phi \in \{25.8°, 154.2°\}$. By making similar analyses at other values of ψ, it was found that the Dyakonov surface waves are excited by s-polarized plane waves in a smaller angular range for the same value of $\gamma = 15°$ than for the p-polarized incident plane waves i.e., $39.7° \leq \psi \leq 44.9°$. Any instance of multiple excitations of Dyakonov surface waves was could not be found by varying the polar angle while keeping the azimuthal angle fixed, when the incident plane wave is s-polarized. All Dyakonov surface waves identified in this section are guided by the isotropic-dielectric/CTF interface because the wavenumbers of the Floquet harmonics and the possible Dyakonov surface waves for this interface match through Eq. (3.3), as explained in the foregoing paragraphs. Surface-wave propagation cannot be supported by the interface of air and the isotropic dielectric material, and any solutions for the air/CTF interface could not be found for the values of χ and ψ used for Figs. 3.3 and 3.4.
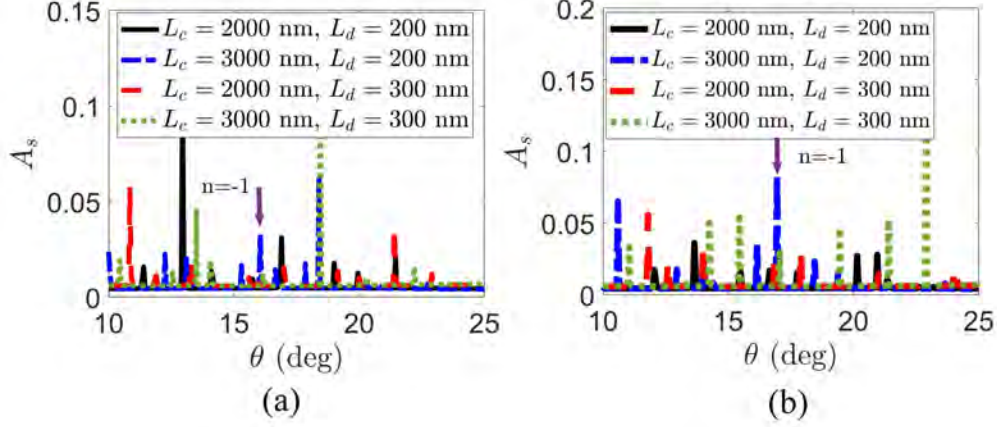
Figure 3.4: Absorptance A_s as a function of incidence angle θ for $L_c \in \{2000, 3000\}$ nm and $L_d \in \{200, 300\}$ nm in the grating-coupled configuration, when $\gamma = 15°$, $\chi_v = 20°$, $L = 500$ nm, and $L_g = 50$ nm. (a) $\psi = 39.7°$ and (b) $\psi = 44°$. A downward arrow identifies the peak that indicates the excitation of a Dyakonov surface wave as a Floquet harmonic of order n, which is indicated alongside the arrow.

3.3 Conclusions

Grating-coupled excitation of Dyakonov surface waves was investigated for the plane-wave illumination of a columnar thin film on top of a one-dimensional dielectric surface-relief grating. The grating plane, the incidence plane, and the morphologically incident planes were taken to be arbitrarily different from each other. The absorptances A_s and A_p were computed using the rigorous coupled-wave approach for various combinations of the thicknesses of the isotropic and the anisotropic partnering dielectric materials. The absorptance peaks independent of the thicknesses of the partnering dielectric materials were identified and the in-plane wavenumbers of the possible Floquet harmonics were compared with the wavenumber of the Dyakonov surface wave. A successful match was used as an indication of the excitation of a Dyakonov surface wave as a Floquet harmonic of a specific order.

- When the incidence plane is not congruent with the grating plane (i.e., $\psi \notin \{0°, 180°\}$) and the incident plane wave is p polarized, Dyakonov surface waves can be excited for multiple values of the polar angle of incidence.

- It was found that p-polarized incident plane waves can excite Dyakonov surface waves in a wider range of directions in the interface plane than s-polarized incident plane waves.

Chapter 4

Excitation of High-Phase-Speed Dyakonov Surface Waves

Electromagnetic surface waves are guided by the interface of two dissimilar materials. Surface-wave propagation is supported by a large variety of combinations of isotropic, homogenous, anisotropic, and periodically nonhomogeneous materials except for the interface of two lossless, isotropic dielectric materials [3, 137, 138]. The amplitudes of the electric and magnetic field phasors of a surface wave decay away from the interface, either monotonically [139, 140] or in a piecewise manner [3, 141]. The characteristics of a surface wave—such as phase speed, attenuation rate, degree of localization, and polarization state—depend upon the two partnering materials. Propagation of the surface wave can be either with attenuation if at least one of the two partnering materials is dissipative [140–143], or without attenuation if both partnering materials are nondissipative [43, 144].

The surface wave that are guided by an interface of two homogeneous dielectric materials of which at least one is anisotropic are commonly called Dyakonov surface waves [12, 43–45, 51, 145–147], although there are antecedent works by others [144, 148]. An anisotropic dielectric material may be either uniaxial [43, 144], biaxial [12, 45, 147], or gyrotropic [49, 149].

If at least one of the two partnering materials is dissipative, the wavenumber of the surface wave is, in general, complex-valued [54, 56] with the phase speed, which is inversely proportional to the real part of the wavenumber, usually smaller than the phase speed of any plane wave propagating in either of the partnering materials. However, the phase speed of the surface wave can be sometime higher than the phase speed of the plane wave in the bulk material, especially when one of the partnering dielectric materials is periodically nonhomogeneous [19].

High-phase-speed Dyakonov surface waves have recently been found to exist at the interface of a dissipative uniaxial dielectric material and a nondissipative isotropic dielectric material [20]. In that work, both partnering materials were taken to occupy adjacent half spaces, which is clearly a physically unrealizable configuration.

In this chapter, the practical configuration was set to examine the excitation of these high-phase-speed Dyakonov surface waves. There are two practical configurations to couple an incident plane wave to a surface wave [3], one involving a prism, the other a surface-relief grating. I chose the latter, because the prism-coupled configuration require a prism made of a material of suitable refractive index, which may not always be possible. Furthermore, the wavenumber of a high-phase-speed Dyakonov surface wave has a real part that is sufficiently small so that a prism may be unnecessary. But that is already available through the grating-coupled configuration which offers coupling through both specular and nonspecular modes [3].

The plan of this chapter is as follows: the boundary-value problem is described briefly in Sec. 4.1, numerical results are presented and discussed in Sec. 4.2, and conclusions in Sec. 4.3.
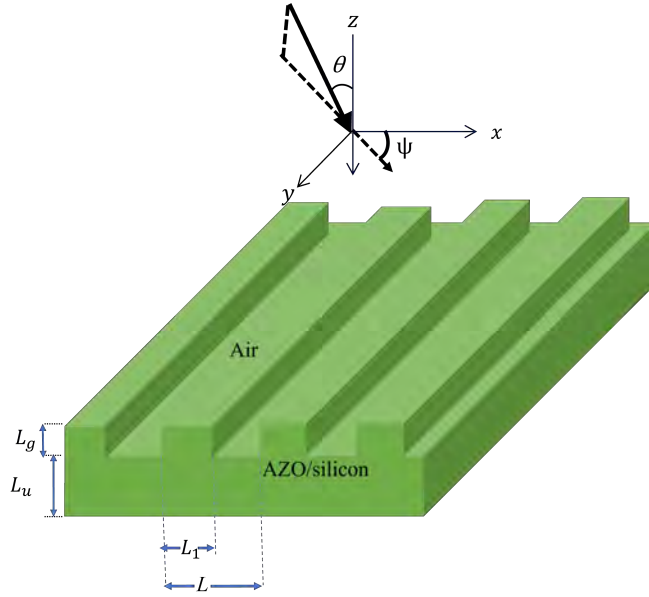
Figure 4.1: Schematic of the boundary-value problem solved for the grating-coupled configuration. The structure is made of a laminar composite material comprising alternating electrically thin sheets of AZO and silicon, which can be homogenized into a uniaxial material.

4.1 Boundary-Value Problem

Let me consider the boundary-value problem shown schematically in Fig. 4.1. The half-spaces $z < 0$ and $z > L_{\mathrm{u}} + L_{\mathrm{g}}$ are vacuous. The region $0 < z < L_{\mathrm{g}}$ is a one-dimensional surface-relief

grating made of alternating bars of vacuum and a uniaxial material labeled $\mathcal{A}$. These bars are invariant along the y axis but have a rectangular cross section in the xz plane. The period is denoted by L, and the cross section of the bars of material $\mathcal{A}$ is of dimensions $L_1 \times L_g$ with $L_1 \in (0, L)$. The region $L_g < z < L_u + L_g$ is occupied by the material $\mathcal{A}$. Thus, the xz plane is the grating plane.

The uniaxial material $\mathcal{A}$ is chosen to be a laminar composite material comprising alternating electrically thin sheets of aluminum-doped zinc oxide (AZO) and silicon identified as "AZO/silicon" in Fig. 4.1. This material was fabricated and optically characterized as a homogenized composite material by Takayama *et al.* [150]. Its relative permittivity dyadic is given by

$$\underline{\underline{\varepsilon}}_\mathcal{A} = \varepsilon_\mathcal{A}^s(\hat{\mathbf{u}}_y\hat{\mathbf{u}}_y + \hat{\mathbf{u}}_z\hat{\mathbf{u}}_z) + \varepsilon_\mathcal{A}^t\hat{\mathbf{u}}_x\hat{\mathbf{u}}_x. \tag{4.1}$$

$L_1 = 0.5L$ was fixed throughout the chapter. The relative permittivity dyadic $\underline{\underline{\varepsilon}}_{gr}(x, z) = \underline{\underline{\varepsilon}}_{gr}(x \pm L, z)$ in the region $0 < z < L_g + L_u$ is represented as a Fourier series, i.e.,

$$\underline{\underline{\varepsilon}}_{gr}(x, z) = \sum_{n \in \mathbb{Z}} \underline{\underline{\varepsilon}}^{(n)}(z) \exp(2in\pi x/L), \qquad z \in (0, L_g + L_u), \tag{4.2}$$

where $\mathbb{Z} = \{0, \pm 1, \pm 2, \ldots\ldots\}$ and the Fourier coefficients

$$\underline{\underline{\varepsilon}}^{(n)}(z) = \begin{cases} \frac{i}{2n\pi}(\underline{\underline{\varepsilon}}_\mathcal{A} - \underline{\underline{I}})\left[(-1)^n - 1\right], & z \in (0, L_g), \\ \underline{\underline{0}}, & z \in (L_g, L_g + L_u), \end{cases} \tag{4.3}$$

for $n \neq 0$ but

$$\underline{\underline{\varepsilon}}^{(0)}(z) = \begin{cases} \frac{1}{2}(\underline{\underline{\varepsilon}}_\mathcal{A} - \underline{\underline{I}}) + \underline{\underline{I}}, & z \in (0, L_g), \\ \underline{\underline{\varepsilon}}_\mathcal{A}, & z \in (L_g, L_g + L_u), \end{cases} \tag{4.4}$$

The interface $z = 0$ is illuminated by a plane wave propagating at the polar angle $\theta \in [0°, 90°)$ with respect to the z axis and the azimuthal angle $\psi \in [0°, 360°)$ with respect to the x axis in the xz plane. The incident, reflected, and transmitted electric field phasors can be written as [3, 135]

$$\mathbf{E}_{inc}(\mathbf{r}) = \sum_{n \in \mathbb{Z}} \left\{ (\mathbf{s}_n a_s^{(n)} + \mathbf{p}_n^+ a_p^{(n)}) \right. \tag{4.5}$$
$$\left. \times \exp[i(k_x^{(n)}x + k_y^{(0)}y + k_z^{(n)}z)] \right\}, \quad z < 0,$$

$$\mathbf{E}_{ref}(\mathbf{r}) = \sum_{n \in \mathbb{Z}} \left\{ (\mathbf{s}_n r_s^{(n)} + \mathbf{p}_n^- r_p^{(n)}) \right. \tag{4.6}$$
$$\left. \times \exp[i(k_x^{(n)}x + k_y^{(0)}y - k_z^{(n)}z)] \right\}, \quad z < 0,$$

and

$$\mathbf{E}_{\text{tr}}(\mathbf{r}) = \sum_{n \in \mathbb{Z}} (\mathbf{s}_n t_{\text{s}}^{(n)} + \mathbf{p}_n^+ t_{\text{p}}^{(n)}) \tag{4.7}$$
$$\times \exp\{i[k_{\text{x}}^{(n)} x + k_{\text{y}}^{(0)} y + k_{\text{z}}^{(n)}(z - L_{\text{g}} - L_{\text{u}})]\}, \qquad z > L_{\text{g}} + L_{\text{u}},$$

where

$$k_{\text{x}}^{(n)} = k_0 \sin\theta \cos\psi + 2n\pi/L, \tag{4.8}$$

$$k_{\text{y}}^{(0)} = k_0 \sin\theta \sin\psi, \tag{4.9}$$

$$k_{\text{xy}}^{(n)} = +\sqrt{(k_{\text{x}}^{(n)})^2 + (k_{\text{y}}^{(0)})^2}, \tag{4.10}$$

$$k_{\text{z}}^{(n)} = \begin{cases} \sqrt{(k_0)^2 - (k_{\text{xy}}^{(n)})^2}, & (k_0)^2 > (k_{\text{xy}}^{(n)})^2, \\ i\sqrt{(k_{\text{xy}}^{(n)})^2 - (k_0)^2}, & (k_0)^2 < (k_{\text{xy}}^{(n)})^2, \end{cases} \tag{4.11}$$

$$\mathbf{s}_n = \frac{-k_{\text{y}}^{(0)} \hat{\mathbf{u}}_{\text{x}} + k_{\text{x}}^{(n)} \hat{\mathbf{u}}_{\text{y}}}{k_{\text{xy}}^{(n)}}, \tag{4.12}$$

and

$$\mathbf{p}_n^{\pm} = \mp \frac{k_{\text{z}}^{(n)}}{k_0} \left(\frac{k_{\text{x}}^{(n)} \hat{\mathbf{u}}_{\text{x}} + k_{\text{y}}^{(0)} \hat{\mathbf{u}}_{\text{y}}}{k_{\text{xy}}^{(n)}} \right) + \frac{k_{\text{xy}}^{(n)}}{k_0} \hat{\mathbf{u}}_{\text{z}}. \tag{4.13}$$

In Eq. (4.5),

$$\left. \begin{array}{l} a_{\text{s}}^{(n)} = \bar{a}_{\text{s}} \, \delta_{n0} \\ a_{\text{p}}^{(n)} = \bar{a}_{\text{p}} \, \delta_{n0} \end{array} \right\}, \tag{4.14}$$

where δ_{nm} is the Kronecker delta, $\bar{a}_{\text{p}} = 0$ for an incident s-polarized plane wave, and $\bar{a}_{\text{s}} = 0$ for an incident p-polarized plane wave. The unknown reflection amplitudes $r_{\text{s}}^{(n)}$ and $r_{\text{p}}^{(n)}$ in Eq. (4.6) and the unknown transmission amplitudes $t_{\text{s}}^{(n)}$ and $t_{\text{p}}^{(n)}$ in Eq. (4.7) have to be determined in terms of $\bar{a}_{\text{s}}$ and $\bar{a}_{\text{p}}$, for which purpose the rigorous coupled-wave approach (RCWA) [3, 14, 15] is very well suited.

The electric and magnetic field phasors in the region $0 < z < L_{\text{g}} + L_{\text{u}}$ are expanded in terms of Floquet harmonics with unknown coefficients. The Floquet harmonics express the x-dependences using the functions $\exp(ik_{\text{x}}^{(n)}x)$, the y-dependence is simply $\exp(ik_{\text{y}}^{(0)}y)$, and the unknown coefficients are functions of z. Non-specular Floquet harmonics are of order $n \neq 0$, whereas the specular Floquet harmonic is of order $n = 0$. After the expansions of the field phasors as well as the Fourier series (4.2) are substituted in the frequency-domain Maxwell curl postulates, all expansions were truncated to exclude $|n| > N_{\text{s}} > 0$. A stable algorithm is then used to determine the unknown coefficients $r_{\text{s}}^{(n)}$, $r_{\text{p}}^{(n)}$, $t_{\text{s}}^{(n)}$, and $t_{\text{p}}^{(n)}$ for $n \in [-N_{\text{s}}, N_{\text{s}}]$ in terms of $\bar{a}_{\text{s}}$ and $\bar{a}_{\text{p}}$ [3].

Table 4.1: Relative permittivity scalars of material $\mathcal{A}$ [20] and the solutions of the canonical boundary-problem for $\psi = 22°$.

λ_0 (μm)	$\varepsilon_\mathcal{A}^t$	$\varepsilon_\mathcal{A}^s$	1st solution	
			q/k_0	v_{ph}/c_0
2.0000	+0.8999+2.0437i	+7.0227+0.5299i	0.9507+0.1575i	1.0519
2.8928	-0.9819+6.5875i	+5.7128+1.6085i	0.9941+0.0578i	1.0059
3.7855	+0.6351+13.0825i	+4.4029+3.0573i	0.9872+0.0356i	1.0130
8.9797	+16.9301+19.9579i	-1.7747+16.0555i	0.9882+0.01647i	1.0119

2nd solution	
q/k_0	v_{ph}/c_0
2.2972 + 0.6771i	0.4353
2.4429+ 0.5966i	0.4094
2.1935 + 0.8119i	0.4559
———	———

The results are compactly expressed using the matrix equations

$$\left[\begin{array}{c} r_{\text{s}}^{(n)} \\ r_{\text{p}}^{(n)} \end{array}\right] = \left[\begin{array}{cc} r_{\text{ss}}^{(n)} & r_{\text{sp}}^{(n)} \\ r_{\text{ps}}^{(n)} & r_{\text{pp}}^{(n)} \end{array}\right] \left[\begin{array}{c} \bar{a}_{\text{s}} \\ \bar{a}_{\text{p}} \end{array}\right]$$ (4.15)

and

$$\left[\begin{array}{c} t_{\text{s}}^{(n)} \\ t_{\text{p}}^{(n)} \end{array}\right] = \left[\begin{array}{cc} t_{\text{ss}}^{(n)} & t_{\text{sp}}^{(n)} \\ t_{\text{ps}}^{(n)} & t_{\text{pp}}^{(n)} \end{array}\right] \left[\begin{array}{c} \bar{a}_{\text{s}} \\ \bar{a}_{\text{p}} \end{array}\right],$$ (4.16)

where $r_{\text{sp}}^{(n)}$, etc., are reflection coefficients and $t_{\text{sp}}^{(n)}$, etc., are transmission coefficients.

Reflectances of nth order are determined as

$$R_{\text{sp}}^{(n)} = |r_{\text{sp}}^{(n)}|^2 \text{Re}\left[k_z^{(n)}/k_z^{(0)}\right],$$ (4.17)

etc., and transmittances likewise as

$$T_{\text{sp}}^{(n)} = |t_{\text{sp}}^{(n)}|^2 \text{Re}\left[k_z^{(n)}/k_z^{(0)}\right],$$ (4.18)

etc. The absorptances for p-polarized and s-polarized incidences are calculated as

$$A_{\text{p}} = 1 - \sum_{n=-N_{\text{s}}}^{N_{\text{s}}} \left[R_{\text{sp}}^{(n)} + R_{\text{pp}}^{(n)} + T_{\text{sp}}^{(n)} + T_{\text{pp}}^{(n)}\right] \in [0,1]$$ (4.19)

$$A_{\text{s}} = 1 - \sum_{n=-N_{\text{s}}}^{N_{\text{s}}} \left[R_{\text{ss}}^{(n)} + R_{\text{ps}}^{(n)} + T_{\text{ss}}^{(n)} + T_{\text{ps}}^{(n)}\right] \in [0,1].$$ (4.20)

The absorptances are zero if material $\mathcal{A}$ is not dissipative [151]

4.2 Numerical Results and Discussion

The canonical boundary-value problem for surface-wave propagation guided by the planar interface of the chosen material $\mathcal{A}$ and vacuum has been solved by Mackay *et al.* [20]. The Matlab™ program is provided in Appendix A.5. The experimentally determined values of the relative permittivity scalars $\varepsilon_{\mathcal{A}}^{\mathrm{t}}$ and $\varepsilon_{\mathcal{A}}^{\mathrm{s}}$ [150] are given in Table 4.1 for four different values of the free-space wavelength $\lambda_0 = 2\pi/k_0$. At a specific value of λ_0, $\mathrm{Re}\left(\underline{\underline{\varepsilon}}_{\mathcal{A}}\right)$ can be either positive definite or indefinite, but $\mathrm{Im}\left(\underline{\underline{\varepsilon}}_{\mathcal{A}}\right)$ is positive definite only.

Two solutions were found in Ref. 20 for $\lambda_0 \in \{2, 2.8928, 3.7855\}$ μm and one for $\lambda_0 = 8.9797$ μm. For each solution, q is the surface wavenumber and $v_{\mathrm{ph}} = \omega/\mathrm{Re}(q)$ is the phase speed. A solution can be considered to be a high-phase-speed solution if $v_{\mathrm{ph}} > c_0$, where $c_0 = 1/\sqrt{\varepsilon_0 \mu_0}$ is the phase speed in vacuum. As can be gathered from Table 4.1, a high-phase-speed solution exists for

- indefinite $\mathrm{Re}\left(\underline{\underline{\varepsilon}}_{\mathcal{A}}\right)$ corresponding to $\lambda_0 \in \{2.8928, 8.9797\}$ μm and

- positive definite $\mathrm{Re}\left(\underline{\underline{\varepsilon}}_{\mathcal{A}}\right)$ corresponding to $\lambda_0 \in \{2, 3.7855\}$ μm.

Here, the focus is on the grating-coupled excitation of these high-phase-speed surface waves.

To identify the excitations of Dyakonov surface waves, the angular spectra of the absorptances A_{p} and A_{s} (i.e., the variations of these absorptances with the polar angle of incidence θ) have to be examined. The code for program is same as provided in Appendix A.3. An absorptance peak whose angular location is independent of L_{u} beyond a threshold value when $L_{\mathrm{g}} > 0$ *may* indicate the excitation of a Dyakonov surface wave. In order to confirm, that angular location has to be compared to the angular locations predicted by the solutions of the canonical boundary-value problem; confirmation requires a reasonable match [130, 135, 147].

In the remainder of this section, the absorptance spectra is presented and analyzed when a grating is present (i.e., $L_{\mathrm{g}} > 0$) and when it is absent (i.e., $L_{\mathrm{g}} = 0$). The corresponding absorptance spectra without the grating are used to identify the peaks arising from the excitation of Dyakonov surface waves. Note that the absorptances are non-zero only due to $\mathrm{Im}(\varepsilon_{\mathcal{A}}^{\mathrm{s}}) > 0$ and/or $\mathrm{Im}(\varepsilon_{\mathcal{A}}^{\mathrm{t}}) > 0$; see Table 4.1.

4.2.1 *p*-Polarized Incidence

Figure 4.2 shows the absorptance A_{p} as a function of θ for different wavelengths when $L = 0.75\,\lambda_0$, $L_1 = 0.5L$, $L_{\mathrm{g}} \in \{0, 200\}$ nm, $L_{\mathrm{u}} = 3$ μm, and $\psi = 22°$.

According to Fig. 4.2(a), a Dyakonov surface wave is excited for $\lambda_0 = 2$ μm when $L_{\mathrm{g}} > 0$, provided that $\theta_1 \simeq 16.2°$, because A_{p} has a peak and the in-plane wavenumber $k_{\mathrm{xy}}^{(-2)} = 2.4103k_0$ of the Floquet harmonic of order $n = -2$ matches the canonical solution $\mathrm{Re}(q) =$

$2.2972k_0$ with an error less than 5%. Figure 4.2(b) shows that a Dyakonov surface wave is excited at $\theta_1 \simeq 17.6°$ for $\lambda_0 = 2.8928$ μm when $L_{\rm g} > 0$, because the in-plane wavenumber $k_{\rm xy}^{(-2)} = 2.3890k_0$ of order $n = -2$ matches the canonical solution $\text{Re}(q) = 2.4429k_0$ with an error less than 2.5%. The absorptance spectra for $L_{\rm g} = 0$ in Figs. 4.2(a) and 4.2(b) do not contain peaks in the vicinities of $16.2°$ and $17.6°$, respectively, indicating the necessity of a grating to excite a Dyakonov surface wave as a Floquet harmonic of order $n \neq 0$.
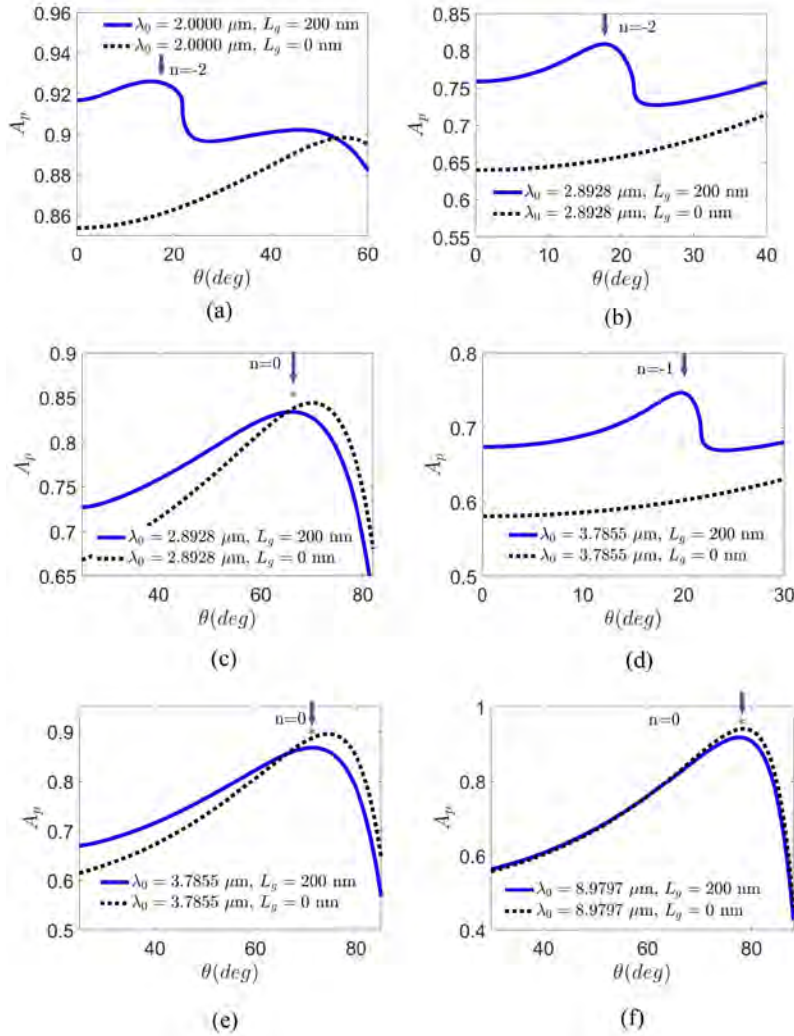
Figure 4.2: Absorptance $A_{\rm p}$ as a function of incidence angle θ when $L = 0.75$ λ_0, $L_1 = 0.5L$, $L_{\rm g} \in \{0, 200\}$ nm, $L_{\rm u} = 3$ μm, and $\psi = 22°$. (a) $\lambda_0 = 2$ μm, (b)–(c) $\lambda_0 = 2.8928$ μm, (d)–(e) $\lambda_0 = 3.7855$ μm, and (f) $\lambda_0 = 8.9797$ μm. A downward arrow identifies the excitation of a Dyakonov surface wave and an asterisk identifies the excitation of high-phase-speed Dyakonov surface wave.

Figure 4.2(c) shows the *possible* excitation of a high-phase-speed Dyakonov surface wave at

$\theta_1 \simeq 66.1°$ for $\lambda_0 = 2.8928$ μm when $L_g > 0$, because the in-plane wavenumber $k_{xy}^{(0)} = 0.9143k_0$ of the Floquet harmonic of order $n = 0$ matches the canonical solution $\text{Re}(q) = 0.9941k_0$ with about 8.7% error. As the error is close to 10%, this is just a conjecture since the absorptance spectra for $L_g = 0$ and $L_g > 0$ are quite similar, decreasing the confidence in attributing the peak solely to the excitation of a surface wave. Indeed, similar confusion persisted [152] in proving the excitation of Uller–Zenneck surface waves [22, 153] that also have a phase speed higher than the speed of light in the partnering materials [3]. The excitation of Uller–Zenneck waves was convincingly shown only with Floquet harmonics of non-zero order [154, 155].

Figure 4.2(d) shows the excitation of a high-phase-speed Dyakonov surface wave for $\lambda_0 = 3.7855$ μm when $L_g = 200$ nm. This excitation occurs at $\theta_1 \simeq 19.8°$, because the in-plane wavenumber $k_{xy}^{(-1)} = 1.0271k_0$ matches the canonical solution $\text{Re}(q) = 0.9872k_0$ with an error less than 3.9%. Figure 4.2(e) shows the *possible* excitation of the same Dyakonov surface wave at $\theta_2 \simeq 71.3°$ since the in-plane wavenumber $k_{xy}^{(0)} = 0.9472k_0$ of the Floquet harmonic of order $n = 0$ closely matches the canonical solution $\text{Re}(q) = 0.9872k_0$ with an error of about 4.2%. Thus, it is possible for a Dyakonov surface wave to be excited twice as the incidence angle θ increases, once as a non-specular Floquet harmonic and once as a specular Floquet harmonic.

The possible excitation of a high-phase-speed Dyakonov surface wave is also evident from the absorptance spectrum in Fig. 4.2(f) for $\lambda_0 = 8.9797$ μm when $L_g = 200$ nm. The excitation occurs at $\theta_1 \simeq 78°$, when the in-plane wavenumber $k_{xy}^{(0)} = 0.9781k_0$ of the Floquet harmonic of order $n = 0$ is within 1.05% of the canonical solution $\text{Re}(q) = 0.9882k_0$.

Figure 4.3 shows the angular spectra of A_p for $\lambda_0 \in \{2.8928, 3.7855, 8.9797\}$ μm, $L = 0.75\lambda_0$, $L_1 = 0.5L$, $L_g \in \{0, 300\}$ nm, $L_u = 3$ μm, and $\psi = 22°$. The evidence of excitation of a Dyakonov surface wave could not be found for $\lambda_0 = 2$ μm for these choices of structural parameters with the incident plane wave being *p*-polarized.

Figure 4.3(a) shows the excitation of a Dyakonov surface wave at $\theta_1 \simeq 16.9°$ for $\lambda_0 = 2.8928$ μm when $L_g = 300$ nm, because the in-plane wavenumber $k_{xy}^{(-2)} = 2.3996k_0$ of the Floquet harmonic of order $n = -2$ differs from $\text{Re}(q) = 2.4429k_0$ by only 1.8%. In addition, the excitation of a high-phase-speed Dyakonov surface wave is conjectured at $\theta_2 \simeq 67.2°$ when $L_g = 300$ nm, since the in-plane wavenumber $k_{xy}^{(0)} = 0.9219k_0$ of the specular Floquet harmonic differs from $\text{Re}(q) = 0.9941k_0$ by 7.83%.

Double excitation of a high-phase-speed Dyakonov surface wave is observed in Figs. 4.3(b) and 4.3(c) for $\lambda_0 = 3.7855$ μm when $L_g > 0$. The first excitation occurs at $\theta_1 \simeq 19.3°$, when $k_{xy}^{(-1)} = 1.0343k_0$ matches the canonical solution $\text{Re}(q) = 0.9872k_0$ with an error of 4.5%. The second excitation occurs at $\theta_2 \simeq 70.3°$, when $k_{xy}^{(0)} = 0.9415k_0$ differs by 4.8% from $\text{Re}(q) = 0.9872k_0$. Although the double excitation of a surface wave had been noted earlier [13, 135], this is the first report of the double excitation of a high-phase-speed surface wave.

Figure 4.3(d) and 4.3(e) demonstrate the double excitation of a high-phase-speed Dyakonov surface wave for $\lambda_0 = 8.9797$ μm when $L_g > 0$, the canonical boundary-value problem yielding $\text{Re}(q) = 0.9882k_0$ for it. The first excitation occurs at $\theta_1 \simeq 21.1°$ with $k_{xy}^{(-1)} = 1.0086k_0$
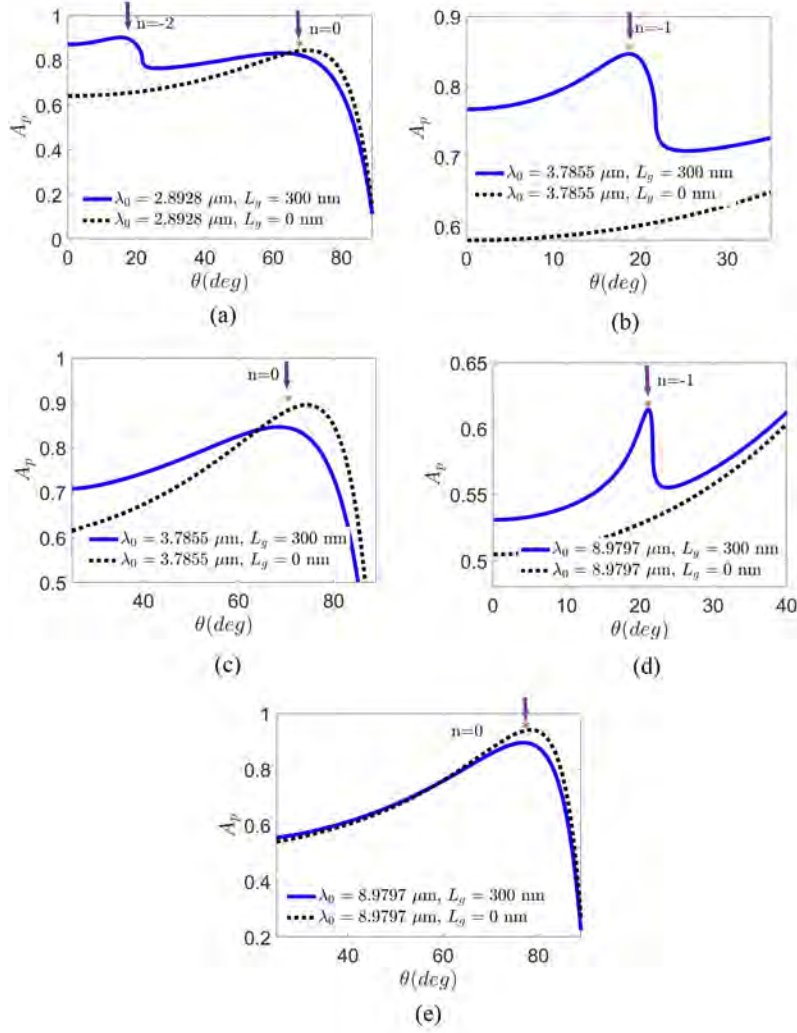
Figure 4.3: Absorptance A_p as a function of incidence angle θ when $L = 0.75\lambda_0$, $L_1 = 0.5L$, $L_g \in \{0, 300\}$ nm, $L_u = 3$ μm, and $\psi = 22°$. (a) $\lambda_0 = 2.8928$ μm, (b)–(c) $\lambda_0 = 3.7855$ μm, and (d)–(e) $\lambda_0 = 8.9797$ μm. A downward arrow identifies the excitation of a Dyakonov surface wave and an asterisk identifies the excitation of high-phase-speed Dyakonov surface wave.

[Fig. 4.3(d)], and the second excitation at $\theta_2 \simeq 77.4°$, with $k_{xy}^{(0)} = 0.9759k_0$ [Fig. 4.3(e)], with errors of 2.02% and 1.3%, respectively.

Figure 4.4 shows plots of A_p as a function of θ for $\lambda_0 \in \{2.8928, 3.7855, 8.9797\}$ μm, $L = 3$ μm, $L_1 = 0.5L$, $L_g \in \{0, 300\}$ nm, $L_u = 3$ μm, and $\psi = 22°$. No Dyakonov surface wave was found to be excited for $\lambda_0 = 2$ μm for these choices of structural parameters.

Figure 4.4(a) shows the excitation of a high-phase-speed Dyakonov surface wave at $\theta_1 \simeq 67.9°$ for $\lambda_0 = 2.8928$ μm when $L_g > 0$, since the in-plane wavenumber $k_{xy}^{(0)} = 0.9265k_0$ of the Floquet harmonic of order $n = 0$ differs from the canonical solution $\mathrm{Re}(q) = 0.9941k_0$

by 7.3%. Figure 4.4(b) demonstrates that two different Dyakonov surface waves are excited for $\lambda_0 = 3.7855$ μm when $L_{\mathrm{g}} > 0$. The first surface wave is excited at $\theta_1 \simeq 14.2°$, when $k_{\mathrm{xy}}^{(-2)} = 2.2981k_0$ matches the canonical solution $\mathrm{Re}(q) = 2.1935k_0$ with an error of 4.5%. The second surface wave is excited at at $\theta_2 \simeq 69.2°$, when $k_{\mathrm{xy}}^{(0)} = 0.9348k_0$ differs by 5.6% from the canonical solution $\mathrm{Re}(q) = 0.9872k_0$. Finally, Fig. 4.4(c) indicates the possible excitation of a high-phase-speed Dyakonov surface wave at $\theta_1 \simeq 75.6°$, with $k_{\mathrm{xy}}^{(0)} = 0.9686k_0$ matching the canonical solution $\mathrm{Re}(q) = 0.9882k_0$ with an error of 2% for $\lambda_0 = 8.9797$ μm.
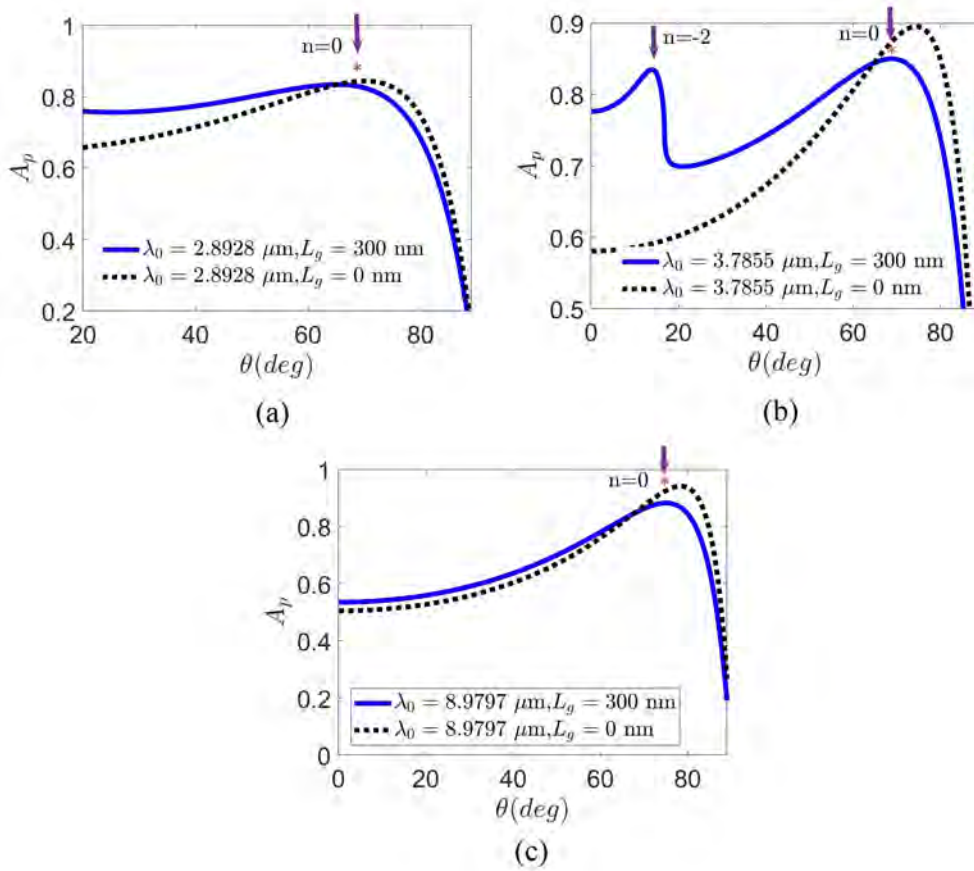
Figure 4.4: Absorptance A_{p} as a function of incidence angle θ when $L = 3$ μm, $L_{\mathrm{g}} = \{0, 300\}$ nm, $L_{\mathrm{u}} = 3$ μm, and $\psi = 22°$. (a) $\lambda_0 = 2.8928$ μm, (b) $\lambda_0 = 3.7855$ μm, and (c) $\lambda_0 = 8.9797$ μm. A downward arrow identifies the excitation of a Dyakonov surface wave and an asterisk identified the excitation of high-phase-speed Dyakonov surface wave.

4.2.2 s-Polarized Incidence

Figure 4.5 shows the angular spectra of the absorptance A_{s} for $\lambda_0 \in \{3.7855, 8.9797\}$ μm, when $L = 3$ μm, $L_1 = 0.5L$, $L_{\mathrm{g}} \in \{0, 300\}$ nm, $L_{\mathrm{u}} = 3$ μm, and $\psi = 22°$. A high-phase-speed

Dyakonov surface wave is possibly excited at $\theta_1 \simeq 20.4°$ as a Floquet harmonic of order $n = -1$ for $\lambda_0 = 3.7855$ μm when $L_g > 0$ in Fig. 4.5(a), because $k_{xy}^{(-1)} = 1.0185k_0$ differs from the canonical solution $\mathrm{Re}(q) = 0.9872k_0$ by 3.1%. Figure 4.5(b) indicates the possible excitation of a high-phase-speed Dyakonov surface wave at $\theta_1 \simeq 21.1°$ for $\lambda_0 = 8.9797$ μm when $L_g > 0$, since $k_{xy}^{(-1)} = 1.0086k_0$ matches the canonical solution $\mathrm{Re}(q) = 0.9882k_0$ with an error less than 2.1%. No Dyakonov surface wave was found to be excited at $\lambda_0 \in \{2, 2.8928\}$ μm by an s-polarized incident plane wave.
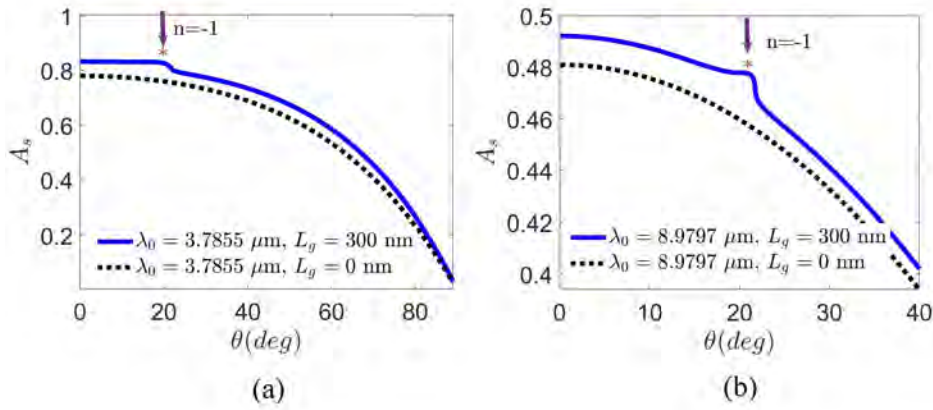
Figure 4.5: Absorptance A_s as a function of incidence angle θ when $L = 3$ μm, $L_1 = 0.5L$, $L_g \in \{0, 300\}$ nm, $L_u = 3$ μm, and $\psi = 22°$. (a) $\lambda_0 = 3.7855$ μm and (b) $\lambda_0 = 8.9797$ μm. A downward arrow identifies the excitation of a Dyakonov surface wave and an asterisk identifies the excitation of a high-phase-speed Dyakonov surface wave.

Figure 4.6 shows the angular spectra of the absorptance A_s as a function of θ for $\lambda_0 = 2$ μm, when $L = 3$ μm, $L_1 = 0.5L$, $L_g \in \{0, 300\}$ nm, $L_u = 3$ μm, and $\psi = 22°$. The excitation occurs at $\theta_1 \simeq 21.1°$ as a Floquet harmonic of order $n = -4$, because $k_{xy}^{(-4)} = 2.3353k_0$ differs from the canonical solution $\mathrm{Re}(q) = 2.2972k_0$ by 1.6%.

The excitation of a Dyakonov surface wave with s-polarized incident light in Figs. 4.5 and 4.6 is quite weak in comparison to excitation with p-polarized incident light in Figs. 4.2–4.4. Furthermore, excitation with s-polarized incident light was found to be rare with high values of L_u, e.g., 3 μm as chosen in Sec. 4.2.1 for p-polarized incident light.

However, for small values of L_u, the excitation of Dyakonov surface waves with s-polarized incidence was found to be frequent, possibly due to the coupling of both faces of the grating. As an example, Fig. 4.7 shows the absorptance A_s as a function of θ for $\lambda_0 \in \{2, 3.7855\}$ μm, when $L = 3$ μm, $L_1 = 0.5L$, $L_g \in \{0, 100\}$ nm, $L_u = 200$ nm, and $\psi = 22°$. Double excitation of a Dyakonov surface wave occurs at $\theta_1 \simeq 20.5°$ with $k_{xy}^{(3)} = 2.3284k_0$ matches the canonical solution with an error of 1.3%, and $\theta_2 \simeq 24.1°$ with $k_{xy}^{(-4)} = 2.2932k_0$ closely matches the canonical solution with an error less than 1%, as Floquet harmonics of order $n = 3$ and $n = -4$,
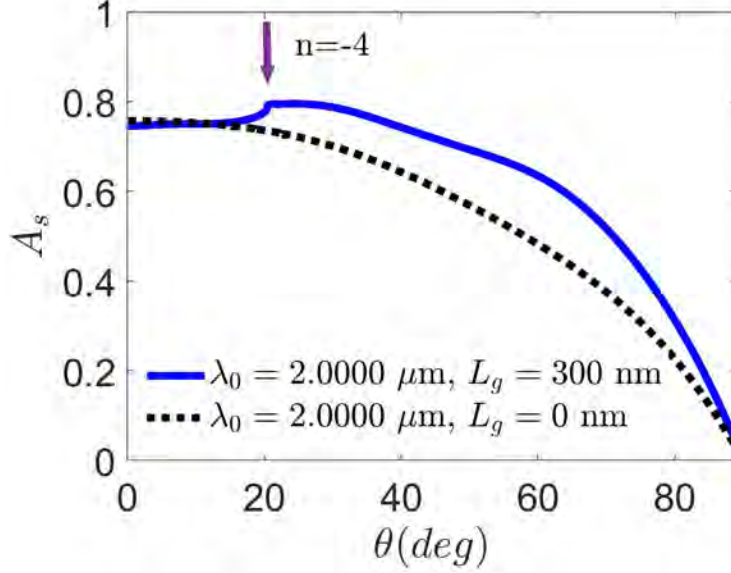
Figure 4.6: Absorptance A_s as a function of incidence angle θ for $\lambda_0 = 2$ μm, when $L = 3$ μm, $L_1 = 0.5L$, $L_g \in \{0, 300\}$ nm, $L_u = 3$ μm, and $\psi = 22°$. A downward arrow identifies the excitation of a Dyakonov surface wave.

respectively, for $\lambda_0 = 2$ μm in Fig. 4.7(a), when $L_g > 0$. The phase speed of this surface wave is less than c_0. The excitation of a a high-phase-speed Dyakoonov surface wave is also indicated in Fig. 4.7(b) at $\theta_1 \simeq 16°$ for $\lambda_0 = 3.7855$ μm when $L_g > 0$, when $k_{xy}^{(-1)} = 1.0116k_0$ differs from the canonical solution $\text{Re}(q) = 0.9872k_0$ by 2.5%.

4.3 Conclusions

Grating-coupled excitation of high-phase-speed Dyakonov surface waves was investigated for the plane-wave illumination of an isotropic dielectric material (air) on top of a one-dimensional uniaxial dielectric surface-relief grating. The absorptances A_p and A_s were computed as functions of the incidence. Those absorptance peaks were identified for which the in-plane wavenumber of some Floquet harmonic matched reasonable well with the wavenumber of a Dyakonov surface wave delivered by the solution of the underlying canonical boundary-value problem.

It was concluded that:

- Both p-polarized and s-polarized plane waves can excite high-phase-speed Dyakonov surface waves.

- Multiple excitations of the high-phase-speed Dyakonov surface waves are also possible.
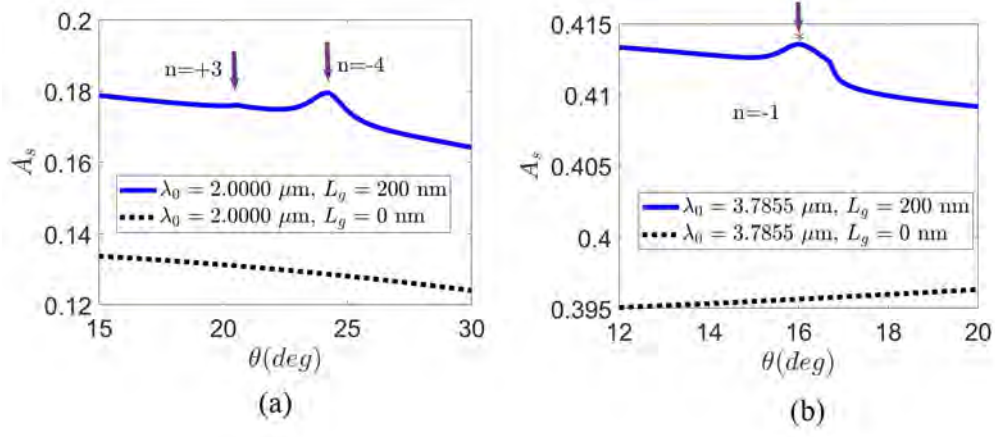
Figure 4.7: Absorptance A_s as a function of incidence angle θ, when $L = 3$ μm, $L_1 = 0.5L$, $L_g \in \{0, 100\}$ nm, $L_u = 200$ nm, and $\psi = 22°$. (a) $\lambda_0 = 2$ μm and (b) $\lambda_0 = 3.7855$ μm. A downward arrow identifies the excitation of a Dyakonov surface wave and an asterisk identified the excitation of high-phase-speed Dyakonov surface wave.

- High-phase-speed Dyakonov surface wave can be excited as a specular and/or a non-specular Floquet harmonic.

Chapter 5

A CTF-based Surface Plasmonic Sensor

The electromagnetic fields of an SPP wave are strong on and in the proximity of the interface but decay away from the interface. This localization property makes them useful for optical sensors because these surface waves are sensitive to the small changes in the electromagnetic properties of the partnering dielectric material near the interface. The surface-plasmonic (i.e., SPP-wave-based) sensors can thus be used to sense pollutants, molecules in analytes, and small concentration of proteins or assays in a solution [1, 2, 16].

The surface-plasmonic sensors operating in the angular interrogation mode [1, 3] measure the change in the direction of propagation of an incident plane wave that excites the SPP wave. However, the SPP wave cannot be excited merely by illuminating a metallic film on top of the partnering dielectric material. The excitation of an SPP wave is due to a resonance phenomenon [32] that is engendered by a match of the SPP wavenumber to the magnitude of the component of the wave vector of the incident plane wave parallel to the interface plane. The grating-coupled configuration can even be used for multiple excitations of an SPP wave [13, 135], thereby providing the opportunity to enhance the reliability and sensitivity of the sensor. The higher reliability is due to the fact that two or more manifestations of surface plasmonic resonance can be used to sense the same analyte. Therefore, SPP-wave-based sensing using the grating coupled-configuration has been studied extensively [156–160].

The optical characteristics of both the metallic and the dielectric partnering materials affect the characteristics of the SPP waves that can be guided by the interface. In the sensing application, the dielectric material plays a critical role not just because the fluid-to-be-sensed usually infiltrates it, but also because of the variety of choices available for it. The partnering dielectric

---

material can be either isotropic [3, 4] or anisotropic [3, 5], and either homogeneous [3, 4] or nonhomogeneous [3, 6]. The usual choice is an isotropic dielectric material [1, 2]. However, anisotropic partnering dielectric materials [17, 18] offer flexibility in designing optical sensors because the permittivity dyadic has more than one scalar parameters to tune the sensitivity.

Therefore, a biaxial dielectric material is chosen that is also porous, for this work. A biaxial dielectric material that is also porous is a columnar thin film (CTF) [84, 90]. The inter-columnar void regions of a CTF have to be infiltrated with the fluid to be sensed [17, 18]. The plan of this chapter is as follows: the boundary-value problem for the grating-coupled configuration is briefly discussed in Sec. 5.1, detailed treatment being available in Chap. 2. Numerical results are presented and discussed in Sec. 5.2 and conclusions are provided in Sec. 5.3.

5.1 Boundary-Value Problem

A schematic of the boundary-value problem is shown in Fig. 5.1. The region $0 < z < L_c$ is occupied by a CTF (whether infiltrated with a fluid or not), the region $L_c + L_g < z < L_t$ by a metal of relative permittivity ε_m, and the half-spaces $z < 0$ and $z > L_t$ are vacuous, where $L_t = L_c + L_g + L_m$. The intermediate region $L_c < z < L_c + L_g$ is occupied by a one-dimensional metallic grating with the CTF inside the troughs of the grating. The grating profile is wholly describable in xz plane (i.e., grating plane), and L is the period along the x axis. The as-
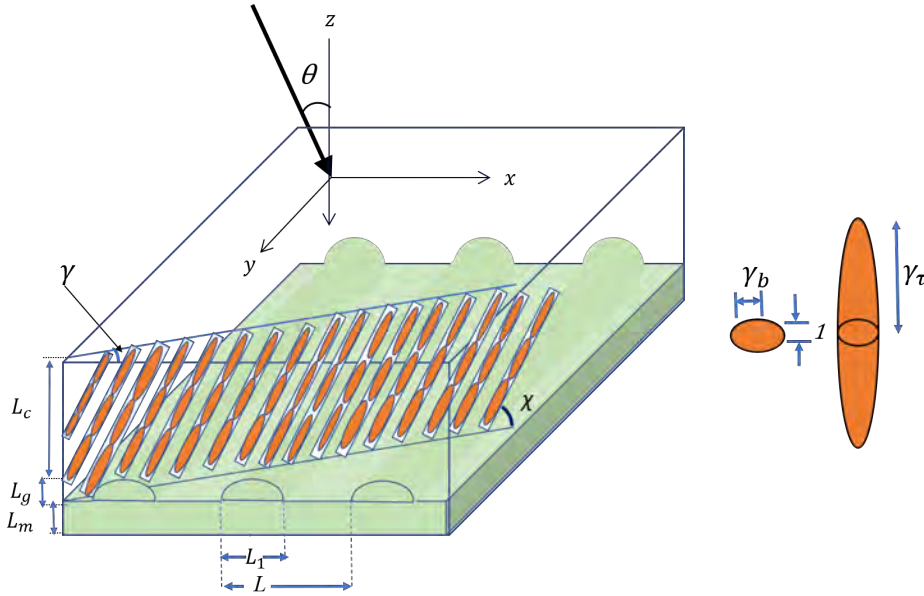
Figure 5.1: Left: Schematic of the boundary-value problem solved for the surface-plasmonic sensor based on grating-coupled configuration. The CTF is symbolically represented by a single row of nanocolumns, each of which is modeled as a string of electrically small ellipsoids with semi-axes in the ratio $1 : \gamma_b : \gamma_\tau$.

deposited CTF is made of a material of refractive index n_s and a fluid of refractive index n_ℓ is present in the void regions of the CTF. The relative permittivity dyadic of the CTF can be written as [13]

$$\underline{\underline{\varepsilon}}_{\text{CTF}} = \underline{\underline{S}}_z \cdot \underline{\underline{S}}_y \cdot \left(\varepsilon_a\, \hat{\mathbf{u}}_z\hat{\mathbf{u}}_z + \varepsilon_b\, \hat{\mathbf{u}}_x\hat{\mathbf{u}}_x + \varepsilon_c\, \hat{\mathbf{u}}_y\hat{\mathbf{u}}_y\right) \cdot \underline{\underline{S}}_y^{-1} \cdot \underline{\underline{S}}_z^{-1}, \tag{5.1}$$

where the principal relative permittivity scalars $\varepsilon_{a,b,c}$ depend on n_s, n_ℓ, and the porosity of the CTF [161].

Without loss of generality, the interface $z = 0$ is illuminated by a plane wave propagating at the polar angle θ with respect to the z axis and propagating in the xz plane. Although the incident plane wave can be arbitrarily polarized, it was fixed to be p-polarized (i.e., $\mathbf{E}_{\text{inc}} \cdot \hat{\mathbf{u}}_y = 0$) because that polarization state is commonly used in SPP-wave-based sensors. Since the plane of incidence (i.e., the xz plane) coincides with the grating plane, the reflected and transmitted electromagnetic fields in the half-spaces $z < 0$ and $z > L_t$, respectively, are independent of y. The rigorous coupled-wave approach (RCWA) [3, 162, 163] was used to calculate the absorptance A_p of the metal-CTF structure as a function of the incidence angle θ of a p-polarized plane wave [135]. In the RCWA, the electric and magnetic field phasors everywhere are expanded as an infinite series of Floquet harmonics of both p- and s-polarization states. For the chosen problem, the Floquet harmonics of order $n \in \{0, \pm 1, \pm 2, \pm 3 \ldots\}$ express the x-dependence of the field phasors using $\exp\left[ik_x^{(n)}x\right]$, where

$$k_x^{(n)} = k_0 \sin\theta + n2\pi/L. \tag{5.2}$$

The relative permittivity dyadic is expanded as a Fourier series with respect to x for every $z \in (0, L_t)$ and substituted in the frequency-domain Maxwell curl postulates. The result is an infinite number of coupled ordinary differential equations. These are truncated so that Floquet harmonics of order $|n| > N_s + 1$, $N_s \geq 1$, are ignored, and a finite number of resulting ordinary differential equations are then solved by applying the piecewise-uniform approximation [3] given in Chap. 2 in the region $0 < z < L_t$. Specular and non-specular reflectances and transmittances of orders $n \in [-N_s, N_s]$ are determined using a stable algorithm, from which the absorptance is obtained by applying the principle of conservation of energy [13, 135]. When the thickness L_m significantly exceeds the skin depth [164] in the chosen metal, the transmitted electric and magnetic fields are negligibly small in magnitude. Care must be taken to ensure that convergent results are obtained as N_s is increased from unity.

5.2   Numerical Results and Discussion

5.2.1   CTF Homogenization

The sensor considered here essentially estimates the change in the refractive index n_ℓ of the fluid infiltrating the CTF because of changes in the relative permittivity scalars $\varepsilon_{a,b,c}$. These three scalars were numerically estimated using a homogenization formalism. There are several homogenization formalisms, including the Maxwell-Garnett formalism [165], the Bragg–Pippard formalism [91], and the Bruggeman formalism [90]. The Bruggeman formalism is more reliable and widely used in optics [166, 167] because it treats all constituent materials equally, unlike the other two formalisms. The Bruggeman formalism was also used in this work to estimate $\varepsilon_{a,b,c}$ as functions of n_ℓ [161]. A Matlab™ code for calculating $\varepsilon_{a,b,c}$ using Bruggeman formalism is provided in Appendix A.6.

Made of a material of refractive index n_s, each nanocolumn of the CTF was represented as a string of electrically small ellipsoids with semi-axes in the ratio $1 : \gamma_b : \gamma_\tau$ so that their shape is characterized by the dyadic [90]

$$\underline{\underline{U}} = \underline{\underline{S}}_z \cdot \underline{\underline{S}}_y \cdot \left(\hat{\mathbf{u}}_z \hat{\mathbf{u}}_z + \gamma_\tau \hat{\mathbf{u}}_x \hat{\mathbf{u}}_x + \gamma_b \hat{\mathbf{u}}_y \hat{\mathbf{u}}_y \right) \cdot \underline{\underline{S}}_y^{-1} \cdot \underline{\underline{S}}_z^{-1}, \tag{5.3}$$

with γ_b in the vicinity of unity and $\gamma_\tau \gg 1$, as shown in Fig. 5.1. The selected uninfiltrated (i.e., $n_\ell = 1$) CTF to have been made by evaporating tantalum oxide with fixed $\chi_v = 15°$; hence, $\chi = 39.77°$. The Bruggeman formalism was implemented here.

Let me introduce the dyadic

$$\underline{\underline{b}} = f \underline{\underline{a}}_s + (1 - f) \underline{\underline{a}}_\ell = \underline{\underline{0}}. \tag{5.4}$$

Here, $\underline{\underline{b}}$ is the volume-fraction-weighted sum of the two polarizability density dyadics [90]

$$\underline{\underline{a}}_{s,\ell} = \varepsilon_0 (\varepsilon_{s,\ell} \underline{\underline{I}} - \underline{\underline{\varepsilon}}_{ref}) \cdot [\underline{\underline{I}} + i\omega \varepsilon_0 \underline{\underline{D}}_{s,\ell} \cdot (\varepsilon_{s,\ell} \underline{\underline{I}} - \underline{\underline{\varepsilon}}_{ref})]^{-1}, \tag{5.5}$$

where $\underline{\underline{D}}_{s,\ell}$ is the depolarization dyadic [90]

$$
\begin{aligned}
\underline{\underline{D}}_{s,\ell} = &\int_{\phi=0}^{\pi/2} \int_{\nu=0}^{\pi/2} \sin\nu \\
&\times \frac{\left(\frac{\cos\nu}{\gamma_\tau^{(s,\ell)}} \right)^2 \hat{\mathbf{u}}_x \hat{\mathbf{u}}_x + \left(\frac{\sin\nu \sin\phi}{\gamma_b^{(s,\ell)}} \right)^2 \hat{\mathbf{u}}_y \hat{\mathbf{u}}_y + (\sin\nu \cos\phi)^2 \hat{\mathbf{u}}_z \hat{\mathbf{u}}_z}{(\sin\nu \cos\phi)^2 \varepsilon_a + \left(\frac{\cos\nu}{\gamma_\tau^{(s,\ell)}} \right)^2 \varepsilon_b + \left(\frac{\sin\nu \sin\phi}{\gamma_b^{(s,\ell)}} \right)^2 \varepsilon_c},
\end{aligned}
\tag{5.6}
$$

computed by using Gauss-Legendre Quadrature integration scheme.

5.2.2 Inverse Bruggeman Formalism

Provided that $\varepsilon_{\mathcal{A}_a}, \varepsilon_{\mathcal{A}_b}, \varepsilon_{\mathcal{A}_c}$ of a CTF have all been measured using appropriate optical experiments and given in Eq. 1.3 of Chap. 1 and $\gamma_\tau > 10$ has been fixed, n_s, f, and γ_b are found by using an inverse Bruggeman homogenization procedure [90]. For CTF, Eq. (5.4) can be written as:

$$\underline{\underline{b}} = b_x(n_s, f, \gamma_b)\hat{\mathbf{u}}_x\hat{\mathbf{u}}_x + b_y(n_s, f, \gamma_b)\hat{\mathbf{u}}_y\hat{\mathbf{u}}_y + b_z(n_s, f, \gamma_b)\hat{\mathbf{u}}_z\hat{\mathbf{u}}_z, \tag{5.7}$$

with

$$\left.\begin{array}{l} b_x(n_s, f, \gamma_b) = 0 \\ b_y(n_s, f, \gamma_b) = 0 \\ b_z(n_s, f, \gamma_b) = 0 \end{array}\right\}, \tag{5.8}$$

solved for known $\varepsilon_{\mathcal{A}_a}, \varepsilon_{\mathcal{A}_b}, \varepsilon_{\mathcal{A}_c}$. The Eqs. (5.8) may computed using any numerical technique for finding the unknowns $\{n_s, f, \gamma_b\}$. Here, a modified Newton–Raphson technique is used to compute $\{n_s^{(k+1)}, f^{(k+1)}, \gamma_b^{(k+1)}\}$ at step $k+1$, using $\{n_s^{(k)}, f^{(k)}, \gamma_b^{(k)}\}$, at step k, as follows:

$$\left.\begin{array}{l} n_s^{(k+1)} = n_s^{(k)} - \dfrac{b_x(n_s^{(k)}, f^{(k)}, \gamma_b^{(k)})}{\frac{\partial}{\partial n_s} b_x(n_s^{(k)}, f^{(k)}, \gamma_b^{(k)})} \\[4ex] f^{(k+1)} = f^{(k)} - \dfrac{b_y(n_s^{(k+1)}, f^{(k)}, \gamma_b^{(k)})}{\frac{\partial}{\partial f} b_y(n_s^{(k+1)}, f^{(k)}, \gamma_b^{(k)})} \\[4ex] \gamma_b^{(k+1)} = \gamma_b^{(k)} - \dfrac{b_z(n_s^{(k+1)}, f^{(k+1)}, \gamma_b^{(k)})}{\frac{\partial}{\partial \gamma_b} b_z(n_s^{(k+1)}, f^{(k+1)} \gamma_b^{(k)})} \end{array}\right\}. \tag{5.9}$$

For the modified Newton–Raphson technique to converge, the most difficult task is to guess the initial estimate that should be sufficiently close to the true solution. The forward Bruggeman formalism may be exploited for finding a suitable initial guess for modified Newton–Raphson technique.

Let ε_a, ε_b, and ε_c denote the estimate of the CTF relative permittivity parameters $\varepsilon_{\mathcal{A}_a, \mathcal{A}_b, \mathcal{A}_c}$. The forward Bruggeman formalism is employed to compute these parameters. The parameters are computed for physically reasonable range of nanoscale parameters i.e., $n_s \in (n_s^L, n_s^U)$, $f \in (f^L, f^U)$, and $\gamma_b \in (\gamma_b^L, \gamma_b^U)$. Then:

1. Fix $n_s = (n_s^L + n_s^U)/2$ and $\gamma_b = (\gamma_b^L + \gamma_b^U)/2$ for a range of f, i.e., $f \in (f^L, f^U)$, identify the new f^+ for which

$$\Delta = \sqrt{(\varepsilon_{\mathcal{A}_a} - \varepsilon_a)^2 + (\varepsilon_{\mathcal{A}_b} - \varepsilon_b)^2 + (\varepsilon_{\mathcal{A}_c} - \varepsilon_c)^2}, \tag{5.10}$$

   is minimized.

2. Update $f = f^+$ and $\gamma_b = (\gamma_b^L + \gamma_b^U)/2$ for $n_s \in (n_s^L, n_s^U)$, identify the new value n_s^+ for

which the value of Δ is minimized.

3. In this step update $f = f^+$ and $n_s = n_s^+$ for a specific range of γ_b i.e., $\gamma_b \in (\gamma_b^L, \gamma_b^U)$, compute Δ and identify the new value of γ_b^+ for which the value of Δ is minimized and update $\gamma_b = \gamma_b^+$.

Repeat the above steps $(1) - (3)$ by substituting $n_s = n_s^+$ and $\gamma_b = \gamma_b^+$ in step (1), and $\gamma_b = \gamma_b^+$ in step (2) until Δ becomes sufficiently small. Numerical experiments indicate that n_s^+, γ_b^+, and f^+ are thought to be the suitable initial estimates for the modified Newton–Raphson technique when $\Delta \ll 0.01$. After evaluating $\{n_s, f, \gamma_b\}$ for a CTF, it is then uniformly infiltrated by a fluid of refractive index n_ℓ. The permittivity dyadic of the fluid-infiltrated CTF shall be

$$\underline{\underline{\varepsilon}}_{CTF} = \underline{\underline{S}}_y \bullet \left(\varepsilon_a \, \hat{\mathbf{u}}_z \hat{\mathbf{u}}_z + \varepsilon_b \, \hat{\mathbf{u}}_x \hat{\mathbf{u}}_x + \varepsilon_c \, \hat{\mathbf{u}}_y \hat{\mathbf{u}}_y \right) \bullet \underline{\underline{S}}_y^{-1} \, , \tag{5.11}$$

The inverse Bruggeman formalism yielded $n_s = 2.2999$, $f = 0.4439$, and $\gamma_b = 2.4322$ for $\chi_v = 15°$. These data were then employed in the forward Bruggeman formalism [161] to find $\varepsilon_{a,b,c}$ as functions of $n_\ell > 1$.

5.2.3   Canonical Boundary-Value Problem

As mentioned previously, the basic principle of a surface-plasmonic sensor is sensing the change in the incidence angle θ where an SPP wave is excited when the refractive index n_ℓ of the infiltrating fluid changes. The excitation of the SPP wave can be best inferred by identifying those peaks in the angular spectrum of A_p that do not change location on the θ axis when the thickness of the partnering dielectric material is changed above a threshold value [168], since SPP waves are localized to their interface. The angular locations of the thickness-independent absorptance peaks must be matched against the SPP waves that are solutions of the underlying canonical boundary-value problem [6, 130]. In this canonical problem, only a single interface between the two partnering materials occupying half spaces is present to rule out the excitation of waveguide modes [27, 133]. Therefore, the solution of the underlying canonical problem are presented before the data calculated for the grating-coupled surface-plasmonic sensor.

In this canonical problem, one half-space is occupied by the fluid-infiltrated CTF whereas a metal occupies the other half-space [12]. Let the SPP wave propagate parallel to the unit vector $\hat{\mathbf{u}}_x$ in the interface plane. The electric and magnetic field phasors vary spatially as $\exp{[i(qx + \alpha z)]}$, with $\text{Im}(\alpha) < 0$ in the fluid-infiltrated CTF and $\text{Im}(\alpha) > 0$ in the metal so that the field phasors decay as $|z| \to \infty$. The complex-valued wavenumber q yields the phase speed and the attenuation rate in the direction of propagation. A combination of search and Newton–Raphson methods [136] was employed to solve the dispersion equation for SPP waves in order to determine the corresponding values of q. The metal was assumed as silver with relative permittivity $\varepsilon_m = -15.4 + 0.4i$ [169] and that the CTF is made by evaporating tantalum oxide

[86]; furthermore, $\gamma = 30°$ and $\lambda_0 = 650$ nm. The code for the program is same as provided in Appendix A.1. Only one solution of the dispersion equation was found for any value of n_ℓ.
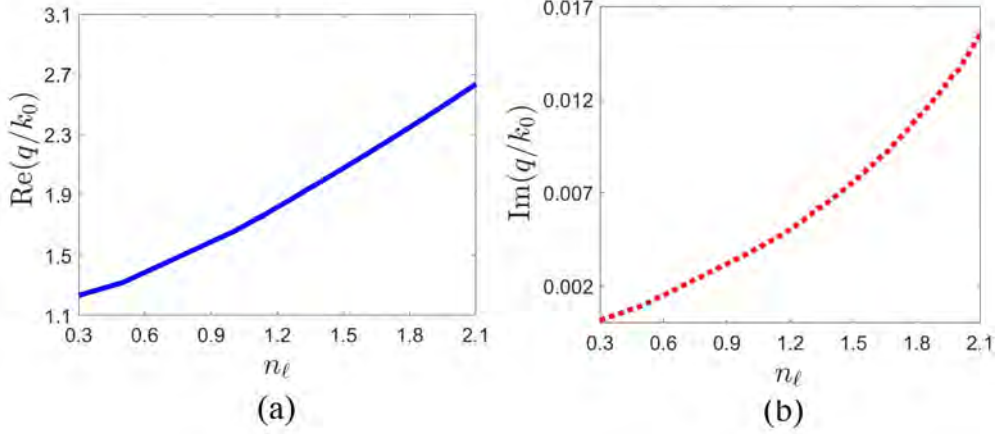
Figure 5.2: Real and imaginary parts of q/k_0 of the SPP wave propagating along the x axis as functions of the refractive index n_ℓ of the infiltrating fluid computed using the canonical boundary-value problem. Whereas $\chi_v = 15°$, $\gamma = 30°$, and $\varepsilon_m = -15.4 + 0.4i$, see Secs. 5.2.1 and 5.2.3 for other relevant parameters.

Thus, only one SPP wave propagating along the x axis can be excited, although it can have multiple excitations in the grating-coupled configuration [13].

The real and imaginary parts of the relative wavenumber q/k_0 of the SPP wave propagating along the x axis are presented in Figs. 5.2(a) and 5.2(b), respectively, as functions of the refractive index n_ℓ. These plots show an approximately linear relationship between q and n_ℓ, which is desirable for a good sensor.

5.2.4 Grating-based Sensor

To delineate the excitation of the SPP wave in the grating-coupled surface-plasmonic sensor as a function of the fluid refractive index n_ℓ, the absorptance A_p was computed the as a function of the incidence angle θ using the RCWA. $N_t = 15$ was fixed after checking that A_p converged within a tolerance limit of $\pm 0.1\%$. As in Secs. 5.2.1 and 5.2.3, $\lambda_0 = 650$ nm, $\chi_v = 15°$, $\gamma = 30°$, $\varepsilon_m = -15.4 + 0.4i$, and $\gamma_\tau = 15$ were fixed. Furthermore, $L_1 = 0.5L$, $L_m = 30$ nm, and $L_g = 20$ nm were also fixed, but L_c was kept variable between 1000 and 4000 nm. A Matlab™ program for computing A_p and A_s is provided in Appendix A.7. The plots in Fig. 5.3 present A_p as a function of θ for $L_c \in \{1000, 2000, 3000, 4000\}$ nm and $n_\ell \in \{1, 1.27, 1.37, 1.43, 1.70\}$ when $L = 500$ nm. Either one or two or three absorptance peaks are present in each angular spectrum. The absorptance peaks with thickness-independent locations on the θ axis were correlated with the data available in Fig. 5.2. For this correlation, it was decided that $|1 - k_x^{(n)}/\mathrm{Re}(q)| \leq 0.05$ for some $n \in [-N_s, N_s]$ at an absorptance peak for that peak to be attributed
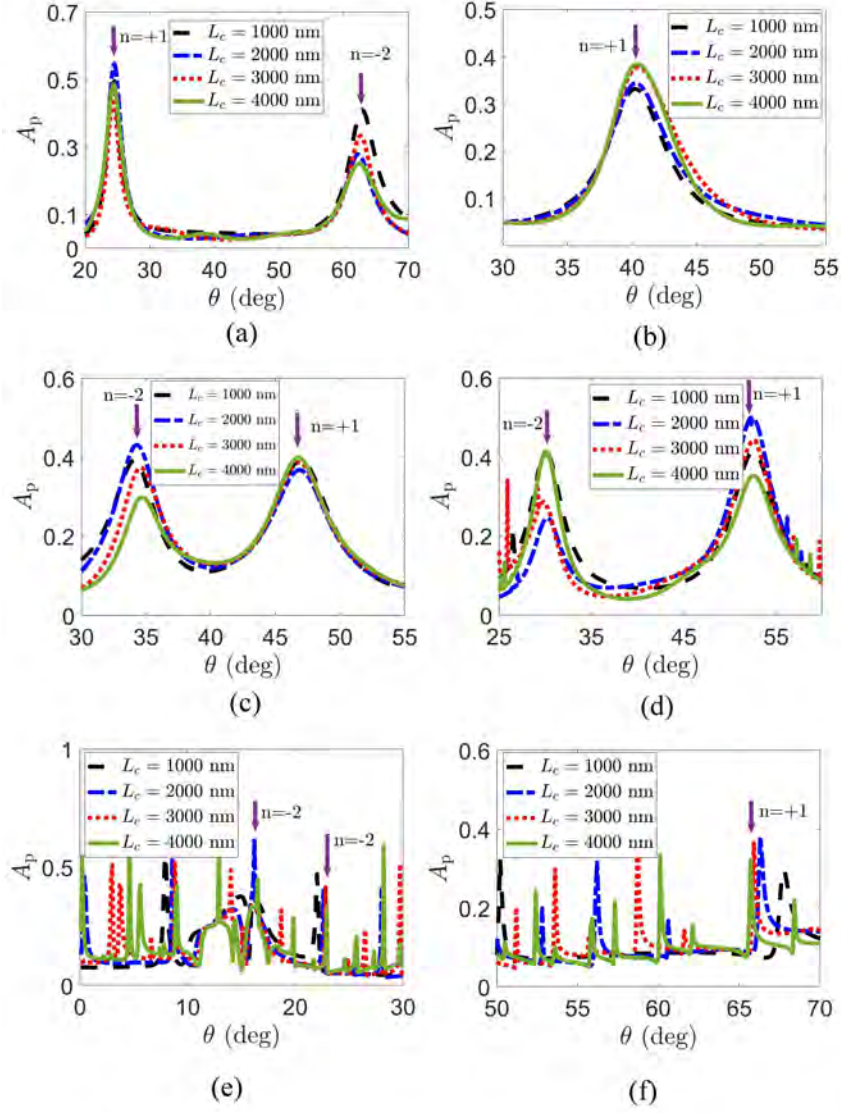
Figure 5.3: Absorptance A_p as a function of incidence angle θ for $L_c \in \{1000, 2000, 3000, 4000\}$ nm and $L = 500$ nm in the grating-coupled configuration. Whereas (a) $n_\ell = 1$, (b) $n_\ell = 1.27$, (c) $n_\ell = 1.37$, (d) $n_\ell = 1.43$, and (e, f) $n_\ell = 1.70$, see Secs. 5.2.1 and 5.2.4 for other relevant parameters. A downward arrow identifies the excitation of the SPP wave as a Floquet harmonic of order n, which is indicated alongside the arrow.

to the excitation of an SPP wave as a Floquet harmonic of order n [13]. When $n_\ell = 1$ (i.e., air infiltrates the CTF), Fig. 5.3(a) shows that the SPP wave with $q = (1.6561 + 0.0037i)k_0$ is excited at

(i) $\theta_1 \simeq 24.4°$ because the in-plane wavenumber $k_x^{(1)} = 1.7131k_0$ of the Floquet harmonic of order $n = +1$, and

71

(ii) $\theta_2 \simeq 62.6°$ because the in-plane wavenumber $k_x^{(-2)} = 1.7122k_0$ of the Floquet harmonic of order $n = -2$

match $\text{Re}(q)$ well according to the 5%-criterion adopted by here. This double excitation of the SPP wave is advantageous for reliable sensing with schema relying on artificial neural networks [170].

The absorptance spectrums in Fig. 5.3(b) illustrate the excitation of an SPP wave for $n_\ell = 1.27$ at $\theta_1 \simeq 40.5°$, when the in-plane wavenumber $k_x^{(1)} = 1.9494k_0$ of the Floquet harmonic of order $n = +1$ matches the solution of the canonical problem with $q = (1.8753 + 0.0056i)k_0$. There is no evidence for the second excitation of the SPP wave for $n_\ell = 1.27$.

However, Fig. 5.3(c) again shows that the excitation of the SPP wave is possible for two values of the incidence angle as two different Floquet harmonics for $n_\ell = 1.37$. The first excitation occurs at $\theta_1 \simeq 34.6°$, when the in-plane wavenumber $k_x^{(-2)} = 2.0322k_0$ matches the canonical solution with $q = (1.9618 + i0.0064i)k_0$. The second excitation occurs at $\theta_2 \simeq 46.7°$, when $k_x^{(1)} = 2.0278k_0$ of the Floquet harmonic of order $n = +1$ is a good match. When $n_\ell = 1.43$, the absorptance spectrums in Fig. 5.3(d) demonstrate that the SPP wave with $q = (2.0142 + 0.0069i)k_0$ is excited at

(i) $\theta_1 \simeq 30.1°$ because the in-plane wavenumber $k_x^{(-2)} = 2.0985k_0$ of the Floquet harmonic of order $n = -2$, and

(ii) $\theta_2 \simeq 52.6°$ because the in-plane wavenumber $k_x^{(1)} = 2.0944k_0$ of the Floquet harmonic of order $n = +1$

match $\text{Re}(q)$ reasonably well.

Finally, when $n_\ell = 1.70$, Figs. 5.3(e) and 5.3(f) demonstrate that the SPP wave with $q = (2.2555 + 0.0097i)k_0$ is excited at

(i) $\theta_1 \simeq 16.5°$ because the in-plane wavenumber $k_x^{(-2)} = 2.3160k_0$ of the Floquet harmonic of order $n = -2$,

(ii) $\theta_2 \simeq 22.9°$ because the in-plane wavenumber $k_x^{(-2)} = 2.2109k_0$ of the Floquet harmonic of order $n = -2$, and

(iii) $\theta_3 \simeq 65.7°$ because the in-plane wavenumber $k_x^{(1)} = 2.2114k_0$ of the Floquet harmonic of order $n = +1$

match $\text{Re}(q)$ reasonably well. Contained in this triple excitation is a doublet: the same SPP wave is excited at two different angular locations but as the same Floquet harmonic ($n = -2$ when $n_\ell = 1.70$). It was observed that the excitation at one angle of incidence is less efficient than at the other in a doublet. In Fig. 5.3(e), the doublet appears at $\theta_1 \simeq 16.5°$ and $\theta_2 \simeq 22.9°$ when $n_\ell = 1.70$, with higher A_p and, therefore, stronger excitation at $\theta_1 \simeq 16.5°$ than at $\theta_2 \simeq 22.9°$. Evidence of the doublet in the grating-coupled configuration has already

been reported [13]. The triple excitation of the SPP wave is going to be even more advantageous for reliable sensing than double excitation, in schema relying on artificial neural networks [170]. The results of Fig. 5.3 allow to conclude that, as θ is varied, the SPP wave can be
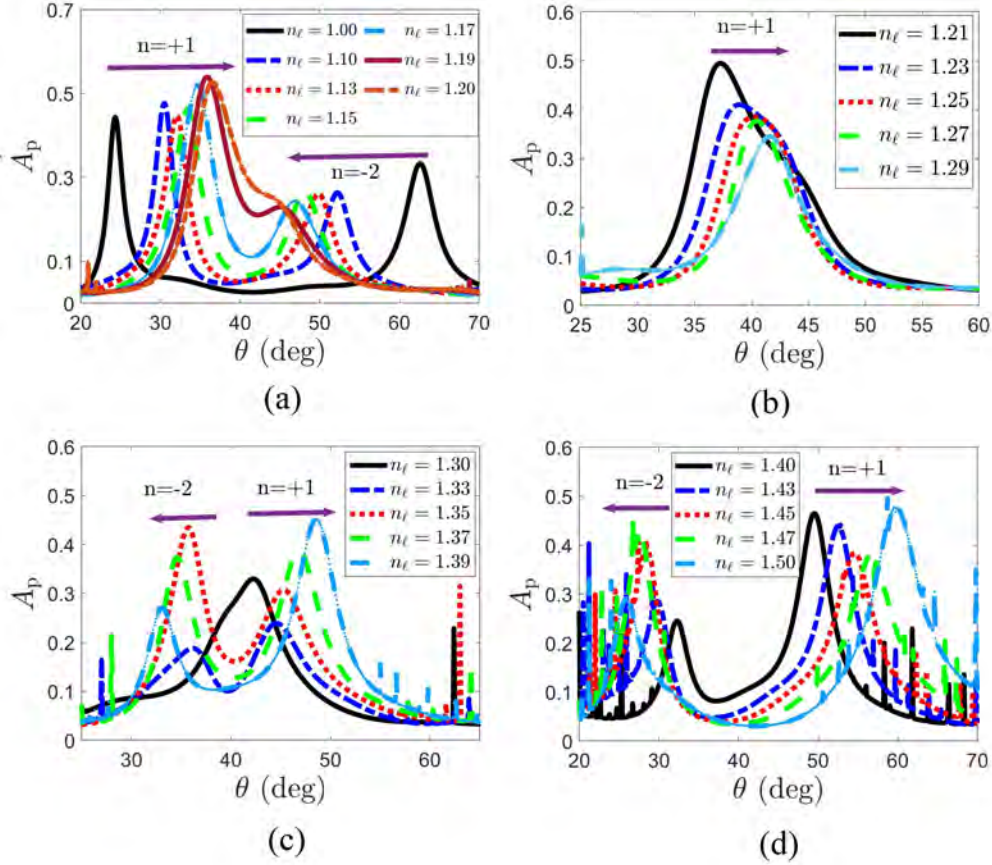
Figure 5.4: Absorptance A_p as a function of incidence angle θ when (a) $n_\ell \in [1.00, 1.20]$, (b) $n_\ell \in [1.21, 1.29]$, (c) $n_\ell \in [1.30, 1.39]$, and (d) $n_\ell \in [1.40, 1.50]$. Whereas $L_c = 3000$ nm and $L = 500$ nm, see Secs. 5.2.1 and 5.2.4 for other relevant parameters. The horizontal arrows show the direction of the shift of peaks representing the excitation of the SPP wave.

multiply excited, depending upon the value of the refractive index n_ℓ of the infiltrating fluid. In order to examine the effect of n_ℓ in detail, Fig. 5.4 shows the angular spectrums of A_p when $L_\mathrm{c} = 3000$ nm and $L = 500$ nm for diverse values of n_ℓ; all other parameters are the same as mentioned at the beginning of Sec. 5.2.4.

Figure 5.4(a) contains two absorptance peaks indicating SPP-wave excitation when $n_\ell \in [1.00, 1.20]$. For each n_ℓ, one peak is for $n = +1$ when $k_\mathrm{x}^{(1)} \simeq \mathrm{Re}(q)$ and the other peak is for $n = -2$ when $k_\mathrm{x}^{(-2)} \simeq \mathrm{Re}(q)$, where q is the wavenumber of the possible SPP wave gleaned from Fig. 5.2. Figure 5.4(b) has a solitary absorptance peak signifying the excitation of the SPP

wave as a Floquet harmonic of order $n = +1$ when $n_\ell \in [1.21, 1.29]$. A similar absorptance peak for $n = -2$ is absent, and it was found that double excitation of the SPP wave is not possible for $n_\ell \in [1.20, 1.29]$. When $n_\ell = 1.30$, the absorptance peak for $n = +1$ is not present in Fig. 5.4(c). Two absorptance peaks for each value of n_ℓ appear again in Figs. 5.4(c) and (d) when $n_\ell \in [1.31, 1.50]$: one peak for $n = +1$ when $k_x^{(1)} \simeq \text{Re}(q)$ and the second peak for $n = -2$ when $k_x^{(-2)} \simeq \text{Re}(q)$. The shifts in the angular locations of the two absorptance peaks indicate that these peaks begin far apart from each other from small values of n_ℓ and comes closer as n_ℓ increases. At intermediates value of n_ℓ, the peaks merge and only one peak is observed. When n_ℓ increases further, the single peak divides into two peaks that get farther apart when n_ℓ is increased further. To analyze the usefulness of the peaks for optical sensing, the sensitivity was computed as

$$S = \frac{\Delta\theta}{\Delta n_\ell}, \tag{5.12}$$

where θ is the n_ℓ-dependent angular location of an absorptance peak and $\Delta\theta$ is the change in θ when the refractive index of the infiltrating fluid changes by Δn_ℓ. The sensitivity was computed from the absorptance plots for the excitation of the SPP wave as a Floquet harmonic of order $n \in \{-2, 1\}$, and is presented in Fig. 5.5 as a function of n_ℓ for $L_c = 3000$ nm and $L = 500$ nm. Additionally, S was computed from the canonical problem by solving $\text{Re}(q) = k_0 \sin\theta + 2n\pi/L$ for θ as a function of n_ℓ and then using Eq. (5.12).

The predicted sensitivity and the sensitivity computed from the absorptance spectrums are in good agreement. From Fig. 5.5, it was observe that the sensitivities of the absorptance peaks corresponding to $n = +1$ are higher than those of the absorptance peaks corresponding to $n = -2$.

So far, the presented results are in an analytical sense that tell the angular location θ of an absorptance peak (that indicates the excitation of an SPP wave) when n_ℓ is known. However, in practice, the reverse task have to accomplish, i.e., find the value of n_ℓ from the knowledge of the angular location of the peak absorptance. To make this easier, Fig. 5.6 shows θ as a function of n_ℓ for both types of absorptance peaks in Fig. 5.4. Once the angular spectrum of absorptance has been measured for an unknown fluid, the angular locations of the absorptance peaks can be found and then those locations can be used to find n_ℓ from Fig. 5.6. The requirement of matching two values of θ (for many values of n_ℓ) with one value of n_ℓ makes the measurement of the refractive index more reliable than the case when only one absorptance peak is present.

There is only one absorptance peak indicating SPP-wave excitation for $n_\ell \in [1.21, 1.31] \cup [1.92, 2.21]$, two such absorptance peaks for $n_\ell \in [0.3, 1.20] \cup [1.32, 1.60] \cup [1.68, 1.69] \cup [1.75, 1.91]$, and three absorptance peaks $n_\ell \in [1.61, 1.67] \cup [1.70, 1.74]$. When three absorptance peaks are possible, two of those peaks form a doublet because both of those peaks satisfy the 5%-criterion for the same n [13]. The doublet is for $n = +1$ when $n_\ell \in [1.61, 1.67]$, but for $n = -2$ when $n_\ell \in [1.70, 1.74]$.

The n_ℓ-ranges for single, double, and triple excitation of the SPP wave depends upon the selection of grating period L. Thus, for $L = 600$ nm, it was determined that single excitation
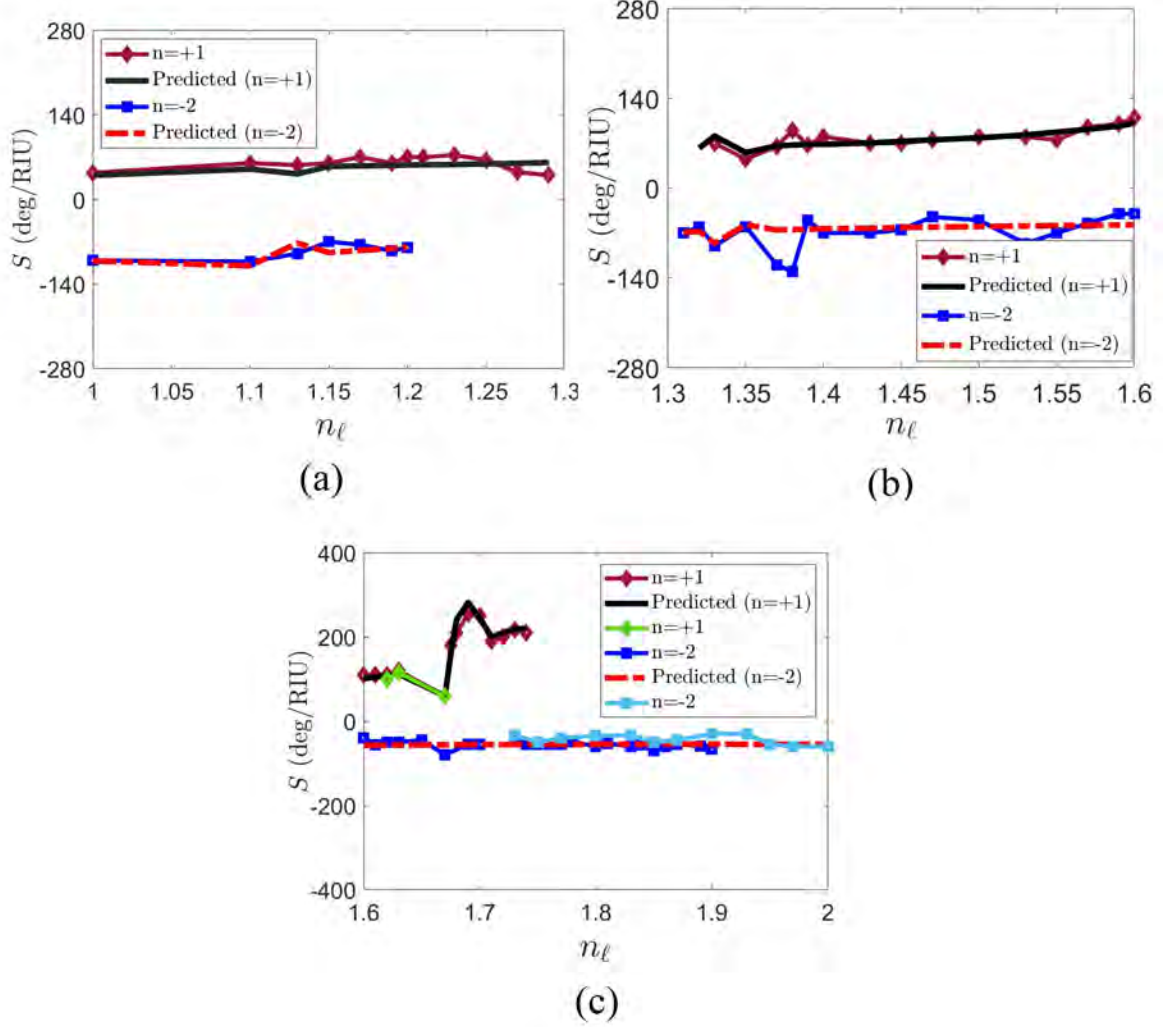
Figure 5.5: Sensitivity S as a function of the refractive index n_ℓ of the infiltrating fluid. The sensitivity, given by Eq. (5.12), was computed from the absorptance plots like the ones given in Fig. 5.4 with $L_c = 3000$ nm and $L = 500$ nm. Doublet excitation is possible for some ranges of n_ℓ in Fig. 5.5(c). The predicted sensitivity was computed using the solutions of the canonical problem in $\mathrm{Re}(q) = k_0 \sin\theta + 2n\pi/L$ to find predicted θ as a function of n_ℓ. All parameters were kept the same as for Fig. 5.4.

occurs for $n_\ell \in [1.30, 1.31] \cup [1.92, 2.45]$, double excitation for $n_\ell \in [0.3, 1.29] \cup [1.46, 1.91]$, and triple excitation for $n_\ell \in [1.33, 1.45]$. Likewise, for $L = 700$ nm, single excitation occurs for $n_\ell = 1.33$, double excitation for $n_\ell \in [1.30, 1.32] \cup [1.95, 2.50]$, and triple excitation for $n_\ell \in [0.3, 1.29] \cup [1.90, 1.94]$. Therefore, L should be chosen to obtain double or triple excitation for the suspected range of n_ℓ for a certain fluid.
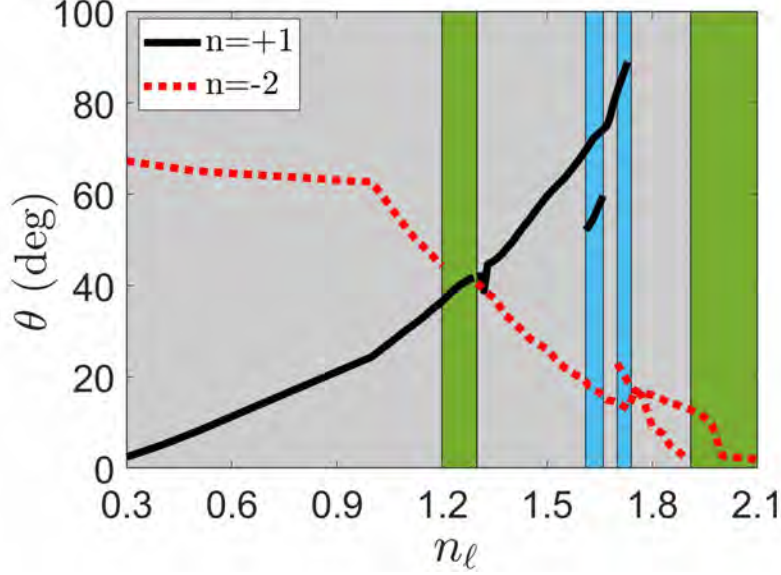
Figure 5.6: The angular location θ of an absorptance peak indicating the excitation of the SPP wave, as a function of the refractive index $n_\ell \in [0.3, 2.5]$ of the infiltrating fluid. All parameters are the same as for Fig. 5.4. Triple excitation of the SPP wave occurs in the blue-shaded regions, double excitation in the grey-shaded regions, and single excitation in the green-shaded regions.

Figure 5.6 indicates that multiple excitation can result in ambiguity when determining n_ℓ. For instance, if $\theta_1 \simeq 27°$ and $\theta_2 \simeq 58°$ are found for a sample, then both $n_\ell = 1.05$ and $n_\ell = 58$ are possible according to Fig. 5.6. The ambiguity can be eliminated by repeating the experiment after diluting the sample. Another way to eliminate the ambiguity is by incorporating A_p-vs.-θ data for a wide enough θ-range in a schema comprising an artificial neural network [170]. Yet another way may be to use two or more sensors with different values of the grating period L.

Before concluding this section, address two issues. First, the air/CTF/metal structure can function as an open-face waveguide [27, 133, 171] whose modes can also be used for sensing an infiltrant fluid. However, as the propagation characteristics of a waveguide mode will depend strongly on the CTF thickness L_c, the angular location of an absorptance peak due to the excitation of that waveguide mode will be highly susceptible to a change in L_c. In contrast, the angular location of an absorptance peak due to the excitation of an SPP wave guided by the metal/CTF interface is weakly dependent on L_c (beyond a threshold value) [18], which confers the advantage of reliability against manufacturing variabilities. Second, although the air/CTF interface could guide surface waves [3], any pertinent solutions were not found for the relevant canonical boundary-value problem [12, 45] for the chosen CTF, whether infiltrated or not.

5.3 Conclusions

An optical sensor was theoretically analyzed for the plane-wave illumination of a CTF on top of a one-dimensional metallic surface-relief grating. The incident plane wave was taken to be p polarized and the plane of incidence to coincide with the grating plane but not necessarily with the morphologically significant plane of the CTF. The absorptance was computed as a function of the angle of incidence for different thicknesses of the CTF, using the rigorous coupled-wave approach. The thickness-independent absorptance peaks were identified and the in-plane wavenumbers of the possible Floquet harmonics were compared with the wavenumber of the SPP wave predicted by the associated canonical boundary-value problem. The change in the angular location of the the absorptance peak representing SPP-wave excitation as a function of the refractive index of the fluid infiltrating the CTF was determine to find the sensitivity.

- Double and triple excitations of the same SPP wave were found to be possible, depending on the refractive index of the fluid, which can help increase the reliability of results by sensing the same fluid with more than one excitations of the SPP wave, possibly with schema that incorporate artificial neural networks.

- In multiple excitations, the same SPP wave is excited as Floquet harmonic of various orders. It is even possible that the excitation occurs at different angles of incidence but as the Floquet harmonic of the same order; however, all excitations are not going to be equally efficient.

- It is concluded that higher sensitivity can be achieved using the grating-coupled configuration than a prism-coupled configuration [17, 18, 89].

Chapter 6

Conclusions and Suggestions for Future Work

6.1   Conclusions

The major goal of this dissertation was to explore the effect of morphology of an anisotropic material on the excitation of SPP waves and Dyakonov surface waves. Moreover, I have explored the characteristics of the optical sensors based on SPP waves in the grating-coupled configuration. In this chapter, I am going to sum up the most important contributions of this thesis.

The excitation of SPP waves and Dyakonov surface waves guided by the interfaces of two dissimilar materials were theoretically studied. In all the boundary-value problems investigated for this thesis, at least one of the partnering materials was supposed to be anisotropic coupled with one-dimensional grating. The anisotropic material could be biaxial or uniaxial. The biaxial material used here was a columnar thin film (CTF) made of tantalum oxide, and uniaxial material was a laminar composite material comprising alternating electrically thin sheets of aluminum-doped zinc oxide (AZO) and silicon. The excitation of SPP waves by a CTF grown on a one-dimensional metallic grating had been studied by Chiadini *et al.* [13]. In their study, it was shown that a CTF on top of a metal grating can support excitation of the SPP waves of different orders with *p*-polarized incident plane wave, but it does not support SPP waves with *s*-polarized incident plane wave. Their study also showed that the excitation of doublet (the SPP wave with same wavenumber and order excited at two distinct angular locations) was possible but their excitation efficiency was dependent upon the angle of incidence. However, they considered only a special geometrical configuration where the grating plane was congruent with the morphologically significant plane of the CTF.

For the work reported in this thesis, the incidence plane, the grating plane, and the morphologically significant plane of the CTF were oriented arbitrarily with respect to each other. When the grating plane and morphologically significant plane of the CTF are taken to be non-congruent, the surface wave cannot be accorded a specific polarization state; labeling its polar-

78

ization state as hybrid [123] is inapt [124]. Therefore, it was possible to excite the surface wave using *s*-polarized incident light as well when the plane of incidence, the grating plane, and the morphologically significant plane were all different. To delineate the excitation of surface waves in the grating-coupled configuration, the absorptance for *p*- and *s*-polarized incident light was computed as a function of the incidence angle θ using the rigorous coupled-wave approach (RCWA). The excitation of the surface wave was inferred by identifying those peaks in the angular spectrum of absorptance that did not change location on the θ axis when the thickness of the partnering dielectric material was changed above a threshold value [168]. The angular locations of the thickness-independent absorptance peaks were matched with the solutions of the underlying canonical boundary-value problem [6, 130]. The solution of boundary-value problem for excitation of SPP waves guided by a CTF deposited on a one-dimensional metallic surface-relief grating employing the RCWA is presented in Chap. 2. A plane wave of either *p*- or *s*-polarization state was considered as incident wave on an interface consisting of CTF and metallic surface-relief grating. The present investigation confirmed that the Floquet harmonics of different orders can be excited by incidence of *p*-polarized light at various incident angles in a co-planer configuration i.e., when all planes coincide with each other. However, my investigation revealed that the excitation of surface wave by an *s*-polarized incident light is also possible when the plane of incidence, the grating plane, and the morphologically significant plane do not coincide with each other. Multiple excitations of the same SPP wave at different angular location for *p*-polarized as well as *s*-polarized incidence were found.

In Chap. 3, an interface consisting of a CTF deposited on a one-dimensional dielectric surface-relief grating was considered and the excitation of Dyakonov surface waves were confirmed in this configuration. No, one or multiple excitations of the same Dyakonov surface wave were found.

In Chap. 4, an interface of air and a uniaxial material was considered for demonstrating the excitation of high-phase-speed Dyakonov surface waves in the grating-coupled configuration. Multiple high-phase-speed Dyakonov surface waves were found to be excited with both *p*-polarized and *s*-polarized incident plane waves as a specular and/or a non-specular Floquet harmonics.

In Chap. 5, an optical sensor was proposed and investigated using a CTF on top of a one-dimensional metallic surface-relief grating. The incident plane wave was taken to be *p*-polarized and the plane of incidence coincided with the grating plane but not with the morphologically significant plane of the CTF. The change in the angular location of the absorptance peaks representing the SPP-wave excitation as a function of the refractive index of the fluid infiltrating the CTF was determined to find the sensitivity of the sensor. It was seen that higher sensitivity can be achieved using the grating-coupled configuration than a prism-coupled configuration [17, 18, 89].

In summary, it was found that

(i) the excitation of surface wave by an *s*-polarized incident light is also possible when the

plane of incidence, the grating plane, and the morphologically significant plane do not coincide with each other;

(ii) no, one, or multiple SPP-wave excitations are possible for *p*-polarized and *s*-polarized incidence;

(iii) multiple excitations of Dyakonov surface wave are possible for *p*-polarized incidence only;

(iv) the CTF-based grating-coupled configuration can be used for optical sensors to achieve higher sensitivity as compared to a prism-coupled configuration;

(v) the excitation of multiple high-phase-speed Dyakonov surface waves with a plane-wave illumination is possible when a partnering dielectric material is a uniaxially anisotropic; and

(vi) high-phase-speed Dyakonov surface wave can be excited as a specular and/or a non-specular Floquet harmonic for *p*-polarized and *s*-polarized incidence.

6.2 Suggestions for Future Work

The study of surface waves in the grating-coupled configuration is still in its infancy, and there is considerable room available to work both theoretically and experimentally. The work reported in this thesis can be used to gain further understanding of surface waves and to analyze other cases for the excitation of Dyakonov surface waves.

The grating-coupled configurations are attractive in sensing applications because these devices offer much higher miniaturization and integration capabilities. Below, I describe a few important grating- problems that can be solved easily based on the formulation provided in this thesis. The solution to these problems can further enhance our understanding of the properties of surface waves and their applications.

6.2.1 Excitation of Surface Waves with CTF/CTF Interface

The interface of a CTF with another CTF provides a phenomenologically rich landscape for Dyakonov surface waves. The mathematical formulation provided in Chap. 2 and Chap. 3 can be employed to tackle this problem. The present work suggests that a CTF/CTF interface will provide more degree of freedom on control parameters and one may obtain interesting results. Experimental data for various CTFs fabricated of titanium, tantalum and zirconium oxides are available that can be used for this problem. Experimetally, it is possible to fabricate the grating-coupled configuration for two different CTFs.

6.2.2   Optical Sensors based on Surface Waves with 2D-Gratings

The work reported in this thesis was based on one-dimensional surface-relief gratings. We considered the grating plane, the incidence plane, and the morphologically planes to be non-congruent. However, if 1D-grating is replaced by 2D-grating, similar results for the excitation of surface waves (both SPP and Dyakonov waves) can be obtained without rotating the grating plane. However, this configuration will increase the possibilities of exciting multiple SPP waves and waveguide modes. Subsequently, the guided-wave propagation could occur in several directions that are not restricted to lie in the incidence plane. The 2D-gratings can be made experimentally and the proposed optical sensor can be designed.

6.2.3   Optical Sensor based on Dyakonov Surface Waves

SPP-wave based optical sensor has been discussed in Chap. 5. Similarly, an optical sensor exploiting Dyakonov surface waves can be designed. This sensor can provide more flexibility than the one based on SPP waves since the fluid-to-be sensed can either infiltrate the partnering CTF or can be the partnering isotorpic dielectric material or both. This can be done theoretically with the same formulation as provided in Chap. 5, except the permittivity of the metal will require to be replaced with of the suitable dielectric material.

Appendix A

Matlab™ Codes

A.1 Newton-Raphson Method to Find q in the Canonical Boundary-Value Problem

```matlab
%****** *** Canonical Solution for Metal/CTF Interface ************%
 % *******   Half space z > 0 occupied by a metal     ********%
% **************    z < 0 occupied by a CTF     **************%
clc
clear all
format long
%************ Defining Inputs    **************%
nm=10^-9;  % nanometers
lambda0 = 633*nm;
knot=(2*pi)/lambda0;   % Free space wave umber
psi= 30*pi/180
 delta=10^(-14);
 error=10^(-8);  % Defining error
 %************      Initial guess **************%
 q=(1+0.01*1i)*knot;
 %*****************       Newton Raphson Method    *************%
 for i=1:200
detM=fun_ctf(q, lambda0, psi);  % Findind determinent of matrix M
detMd=fun_ctf(q+delta*q, lambda0,psi);
 dff=(detMd-detM)/(delta*q);  % Findind derivative of det{M}
 f=q-detM/dff;   % Newton-Raphson Method
err=abs(detM);
%*******      checking the amount of error at each iteration
    *********%
```

```matlab
if err<=error
break
end
% Update q
q=f;
disp(q/knot);
disp(i);
 end

%******** Function for Solving the Dispersion Equation **********%
function detr= fun_ctf(q, lambda0, psi)
%********    Defining Inputs   ********%
muo=4*pi*10^-7;        % Free space permeability
epso = 8.854*10^-12;   % Free space permittivity
eta0 =sqrt(muo/epso);  %Impedence of free space
gamma = (30*pi)/180;
chiv=20*pi/180;
chi=atan(3.1056*tan(chiv));
v=2*chiv/pi;
epsa= (1.1961 +1.5439*v - 0.7719*v^2)^2;
epsb= (1.4600 + 1.0400*v-0.5200*v^2)^2;
epsc= (1.3532 + 1.2296*v - 0.6148*v^2)^2;
ns=0.05096+1i*3.92451;
knot=(2*pi)/lambda0;
omg=knot/sqrt(muo*epso);
% ************* [P] Matrix for CTF **************************%
pa_11=(q*(epsa-epsb)*cos(gamma)*cos(chi)*cos(psi)*sin(chi))/(epsa*
    cos(chi)^2+epsb*sin(chi)^2);
pa_12=(q*(epsa-epsb)*cos(chi)*cos(psi)*sin(gamma)*sin(chi))/(epsa*
    cos(chi)^2+epsb*sin(chi)^2);
pa_13=((q^2)*cos(psi)*sin(psi))/(epso*omg*(epsa*cos(chi)^2+epsb*sin(
    chi)^2));
pa_14=omg*muo-(q^2*cos(psi)^2)/(omg*epso*(epsa*cos(chi)^2+epsb*sin(
    chi)^2));
pa_21=(q*(epsa-epsb)*cos(gamma)*cos(chi)*sin(chi)*sin(psi))/(epsa*
    cos(chi)^2+epsb*sin(chi)^2);
pa_22=(q*(epsa-epsb)*cos(chi)*sin(gamma)*sin(chi)*sin(psi))/(epsa*
    cos(chi)^2+epsb*sin(chi)^2);
pa_23=-omg*muo+(q^2*sin(psi)^2)/(omg*epso*(epsa*cos(chi)^2+epsb*sin(
    chi)^2));
```

```
pa_24=-((q^2)*cos(psi)*sin(psi))/(omg*epso*(epsa*cos(chi)^2+epsb*sin
    (chi)^2));
pa_31 = (omg*epso*cos(gamma)*((epsb*epsc)+(epsa*(epsc-2*epsb))+(epsa
    -epsb)*epsc*cos(2*chi))*sin(gamma))/(2*(epsa*cos(chi)^2+epsb*sin(
    chi)^2))-((q^2)*cos(psi)*sin(psi))/(omg*muo);
pa_32=-omg*epso*epsc*cos(gamma)^2+((q^2)*cos(psi)^2)/(omg*muo)-omg*
    epso*(sin(gamma)^2)*(epsb*cos(chi)^2+epsa*sin(chi)^2)+(omg*epso
    *((epsa-epsb)^2)*(cos(chi)^2)*(sin(gamma)^2)*(sin(chi)^2))/(epsa*
    cos(chi)^2+epsb*sin(chi)^2);
pa_33=(q*(epsa-epsb)*cos(chi)*sin(gamma)*sin(chi)*sin(psi))/(epsa*
    cos(chi)^2+epsb*sin(chi)^2);
pa_34=(q*(-epsa+epsb)*cos(chi)*sin(gamma)*sin(chi)*cos(psi))/(epsa*
    cos(chi)^2+epsb*sin(chi)^2);
pa_41=omg*epso*epsc*sin(gamma)^2+(omg*epso*epsa*epsb*cos(gamma)^2)/(
    epsa*cos(chi)^2+epsb*sin(chi)^2)-q^2*sin(psi)^2/(omg*muo);
pa_42=(omg*epso*(2*epsa*epsb-epsa*epsc-epsb*epsc-(epsa-epsb)*epsc*
    cos(2*chi))*sin(2*gamma))/(4*(epsa*cos(chi)^2+epsb*sin(chi)^2))
    +((q^2)*cos(psi)*sin(psi))/(omg*muo);
pa_43= (q*(-epsa+epsb)*cos(gamma)*sin(chi)*sin(psi)*cos(chi))/(epsa*
    cos(chi)^2+epsb*sin(chi)^2);
pa_44=(q*(epsa-epsb)*cos(gamma)*cos(chi)*cos(psi)*sin(chi))/(epsa*
    cos(chi)^2+epsb*sin(chi)^2);
pa=[pa_11 pa_12 pa_13 pa_14; pa_21 pa_22 pa_23 pa_24; pa_31 pa_32
    pa_33 pa_34; pa_41 pa_42 pa_43 pa_44];
%*** Selection of Eigenvalues and Eigenvectors  for z<0 ****%
[Ga, Da]=eig(pa);
D2a=diag(Da);
Da_imag=imag(D2a);
Da_real=real(D2a);
[D3a, sortindex3]=sort(Da_imag,'descend');
Da_real1=Da_real(sortindex3);
Da=Da_real1+1i*D3a;
Dam=diag(Da);
tna=Ga(:,sortindex3);
t1=tna(1:4,1);
t2=tna(1:4,2);
%%
%****** Selection of eigenvalues and eigenvectors z>0 *******%
alpha_s=sqrt(knot^2*ns^2-q^2);
```

```
if imag(alpha_s)<0
    alpha_ss=-alpha_s;
    alpha_s=alpha_ss;
end
 fn=[-sin(psi) alpha_s*cos(psi)/knot; cos(psi) alpha_s*sin(psi)/knot
    ; alpha_s*cos(psi)/(knot*eta0) ns^2*sin(psi)/eta0;
    alpha_s*sin(psi)/(knot*eta0)  -ns^2*cos(psi)/eta0];
M=[t1 t2 -fn ];  %Finding the matrix M
detr=det(M);      %Finding determinent of M
end
```

A.2 Absorptance A_p in the Grating-Coupled Configuration for $\psi = \gamma = 0°$

```
clc
clear all
close all
global epctf epm  d1 d2 d3  L L1  z1 z2 z3 N_ts  ;
%******* Defining Variables *******%
mu_0=4*pi*10^-7;
ep_0 = 8.854*10^-12;
nm=10^(-9);
lambda_0 = 633*nm;
eta_0 =sqrt(mu_0/ep_0);
epm=(0.05096+3.9245*1i)^2;
L = 900*nm;
for dd=1:3
    if dd==1
        d1 =1000*nm;
    elseif dd==2
        d1 =2000*nm;
    else
        d1 =3000*nm;
    end
    d2 = d1 + 20*nm;
d3 = d2 + 30*nm;
L1 = 0.5*L;
N_ts = 15;
Nd = 50;
Ng = 30;
```

```matlab
Nm=10;
Ns = Nd + Ng;
gamma_deg = (30*pi)/180;
sz = [cos(gamma_deg) -sin(gamma_deg) 0 ; sin(gamma_deg) cos(
    gamma_deg) 0; 0 0 1];
chiv=20*pi/180;
        chi=atan(3.1056*tan(chiv));
        v=2*chiv/pi;
        sy= [cos(chi) 0 -sin(chi); 0 1 0; sin(chi) 0  cos(chi)];
        epa= (1.1961 +1.5439*v - 0.7719*v^2)^2;
        epb= (1.4600 + 1.0400*v-0.5200*v^2)^2;
        epc= (1.3532 + 1.2296*v - 0.6148*v^2)^2;
      epref=[epb 0 0; 0 epc 0; 0 0 epa];
        epctf=sz*sy*epref*inv(sy)*inv(sz);
knot=(2*pi)/lambda_0;
vv=1;
psi=30*pi/180;
% ****** End Defining Variables   ******%
%%
di=0;
dt=0.1;
df=89;
vv= 1;
for NN=di:dt:df
    theta=NN*pi/180;
     disp(NN);
     y1=0;
%****** Begin Finging wavenumbers *****%
    for n1=-N_ts:1:N_ts
        y1=y1+1;
        kxnn(y1)=knot*cos(psi)*sin(theta)+(n1*2*pi)/L;
        if knot^2 >= kxnn(y1)^2
            kzn(y1) = sqrt(knot^2 - kxnn(y1)^2);
  elseif  knot^2 < kxnn(y1)^2
            kzn(y1) = 1i*sqrt(-knot^2 + kxnn(y1)^2);
  end
  end
kx = diag(kxnn);
%************ End Finging wavenumbers ********************%
```

```matlab
%************** Finding Y Matrices ****************%
 ype=[-diag((1/knot).*kzn) ];
yne=[diag((1/knot).*kzn) ];
yph=[ -eye(2*N_ts+1) ];
ynh=[-eye(2*N_ts+1) ];
 ypos=[ype;yph];
 yneg=[yne;ynh];
 Z1=[ype;yph];
 temp1=(Ns+Nm+1:-1:1);
 mm=length(temp1);
 matrix_zz{Nd+Ng+Nm+1} = Z1;
 for n=Ns+Nm:-1:1
%%
%********************** Permittivity For metal Region
      *************%
 if n>Ns
     delta(n)=(d3-d2)/Nm;
        x1 = d2- (d2 - d3)*(n - Ns)/Nm;
         x2 = d2 - (d2 - d3)*(n - 1 - Ns)/Nm;
         z1 = 0.5*(x1 + x2);
for n3=0:2*N_ts
    eparxx(n3+1)=permctf(z1,n3,0,epm,d1,d2,L,L1);
    eparxxn(n3+1)=permctf(z1,-n3,0,epm,d1,d2,L,L1);
    eparxy(n3+1)=permctf(z1,n3,0,0,d1,d2,L,L1);
    eparxyn(n3+1)=permctf(z1,-n3,0,0,d1,d2,L,L1);
    eparxz(n3+1)=permctf(z1,n3,0,0,d1,d2,L,L1);
    eparxzn(n3+1)=permctf(z1,-n3,0,0,d1,d2,L,L1);
    eparyx(n3+1)=permctf(z1,n3,0,0,d1,d2,L,L1);
    eparyxn(n3+1)=permctf(z1,-n3,0,0,d1,d2,L,L1);
    eparyy(n3+1)=permctf(z1,n3,0,epm,d1,d2,L,L1);
    eparyyn(n3+1)=permctf(z1,-n3,0,epm,d1,d2,L,L1);
    eparyz(n3+1)=permctf(z1,n3,0,0,d1,d2,L,L1);
    eparyzn(n3+1)=permctf(z1,-n3,0,0,d1,d2,L,L1);
    eparzx(n3+1)=permctf(z1,n3,0,0,d1,d2,L,L1);
    eparzxn(n3+1)=permctf(z1,-n3,0,0,d1,d2,L,L1);
    eparzy(n3+1)=permctf(z1,n3,0,0,d1,d2,L,L1);
    eparzyn(n3+1)=permctf(z1,-n3,0,0,d1,d2,L,L1);
    eparzz(n3+1)=permctf(z1,n3,0,epm,d1,d2,L,L1);
    eparzzn(n3+1)=permctf(z1,-n3,0,epm,d1,d2,L,L1);
```

```matlab
end
    exx=toeplitz(eparxx,eparxxn);
    exy=toeplitz(eparxy,eparxyn);
    exz=toeplitz(eparxz,eparxzn);
    eyx=toeplitz(eparyx,eparyxn);
    eyy=toeplitz(eparyy,eparyyn);
    eyz=toeplitz(eparyz,eparyzn);
    ezx=toeplitz(eparzx,eparzxn);
    ezy=toeplitz(eparzy,eparzyn);
    ezz=toeplitz(eparzz,eparzzn);
%*************** End Metal Permittivity ******************%
elseif   n<=Nd+Ng && n>Nd
         % ********** Start Grating Permittivity **************%%%
          delta(n)=(d2-d1)/Ng;
         x3 = d1 - (d1 - d2)*(n - Nd)/Ng;
         x4 = d1 - (d1 - d2)*(n - 1 - Nd)/Ng;
         z2 = 0.5*(x3 + x4);
  for q3=0:2*N_ts
    eparxx(q3+1)=permctf(z2,q3,epctf(1,1),epm,d1,d2,L,L1);
    eparxxn(q3+1)=permctf(z2,-q3,epctf(1,1),epm,d1,d2,L,L1);
     eparxy(q3+1)=permctf(z2,q3,epctf(1,2),0,d1,d2,L,L1);
    eparxyn(q3+1)=permctf(z2,-q3,epctf(1,2),0,d1,d2,L,L1);
     eparxz(q3+1)=permctf(z2,q3,epctf(1,3),0,d1,d2,L,L1);
    eparxzn(q3+1)=permctf(z2,-q3,epctf(1,3),0,d1,d2,L,L1);
     eparyx(q3+1)=permctf(z2,q3,epctf(2,1),0,d1,d2,L,L1);
    eparyxn(q3+1)=permctf(z2,-q3,epctf(2,1),0,d1,d2,L,L1);
    eparyy(q3+1)=permctf(z2,q3,epctf(2,2),epm,d1,d2,L,L1);
    eparyyn(q3+1)=permctf(z2,-q3,epctf(2,2),epm,d1,d2,L,L1);
     eparyz(q3+1)=permctf(z2,q3,epctf(2,3),0,d1,d2,L,L1);
    eparyzn(q3+1)=permctf(z2,-q3,epctf(2,3),0,d1,d2,L,L1);
     eparzx(q3+1)=permctf(z2,q3,epctf(3,1),0,d1,d2,L,L1);
    eparzxn(q3+1)=permctf(z2,-q3,epctf(3,1),0,d1,d2,L,L1);
    eparzy(q3+1)=permctf(z2,q3,epctf(3,2),0,d1,d2,L,L1);
    eparzyn(q3+1)=permctf(z2,-q3,epctf(3,2),0,d1,d2,L,L1);
    eparzz(q3+1)=permctf(z2,q3,epctf(3,3),epm,d1,d2,L,L1);
    eparzzn(q3+1)=permctf(z2,-q3,epctf(3,3),epm,d1,d2,L,L1);
end
exx=toeplitz(eparxx,eparxxn);
exy=toeplitz(eparxy,eparxyn);
```

```matlab
exz=toeplitz(eparxz,eparxzn);
eyx=toeplitz(eparyx,eparyxn);
eyy=toeplitz(eparyy,eparyyn);
eyz=toeplitz(eparyz,eparyzn);
ezx=toeplitz(eparzx,eparzxn);
ezy=toeplitz(eparzy,eparzyn);
ezz=toeplitz(eparzz,eparzzn);
  %************* Permittivity for  CTF *************%
 elseif  n<= Nd
            delta(n)=d1/Nd;
            x5 = (d1)*n/Nd;
            x6 = (d1)*(n- 1)/Nd;
            z3 = 0.5*(x5 + x6);
 for  j1 =0:2*N_ts
    eparxx(j1+1)=permctf(z3,j1,epctf(1,1),0,d1,d2,L,L1);
    eparxxn(j1+1)=permctf(z3,-j1,epctf(1,1),0,d1,d2,L,L1);
    eparxy(j1+1)=permctf(z3,j1,epctf(1,2),0,d1,d2,L,L1);
    eparxyn(j1+1)=permctf(z3,-j1,epctf(1,2),0,d1,d2,L,L1);
     eparxz(j1+1)=permctf(z3,j1,epctf(1,3),0,d1,d2,L,L1);
    eparxzn(j1+1)=permctf(z3,-j1,epctf(1,3),0,d1,d2,L,L1);
    eparyx(j1+1)=permctf(z3,j1,epctf(2,1),0,d1,d2,L,L1);
    eparyxn(j1+1)=permctf(z3,-j1,epctf(2,1),0,d1,d2,L,L1);
    eparyy(j1+1)=permctf(z3,j1,epctf(2,2),0,d1,d2,L,L1);
    eparyyn(j1+1)=permctf(z3,-j1,epctf(2,2),0,d1,d2,L,L1);
     eparyz(j1+1)=permctf(z3,j1,epctf(2,3),0,d1,d2,L,L1);
    eparyzn(j1+1)=permctf(z3,-j1,epctf(2,3),0,d1,d2,L,L1);
    eparzx(j1+1)=permctf(z3,j1,epctf(3,1),0,d1,d2,L,L1);
    eparzxn(j1+1)=permctf(z3,-j1,epctf(3,1),0,d1,d2,L,L1);
    eparzy(j1+1)=permctf(z3,j1,epctf(3,2),0,d1,d2,L,L1);
    eparzyn(j1+1)=permctf(z3,-j1,epctf(3,2),0,d1,d2,L,L1);
    eparzz(j1+1)=permctf(z3,j1,epctf(3,3),0,d1,d2,L,L1);
    eparzzn(j1+1)=permctf(z3,-j1,epctf(3,3),0,d1,d2,L,L1);
end
exx=toeplitz(eparxx,eparxxn);
exy=toeplitz(eparxy,eparxyn);
exz=toeplitz(eparxz,eparxzn);
eyx=toeplitz(eparyx,eparyxn);
eyy=toeplitz(eparyy,eparyyn);
eyz=toeplitz(eparyz,eparyzn);
```

```matlab
ezx=toeplitz(eparzx,eparzxn);
ezy=toeplitz(eparzy,eparzyn);
ezz=toeplitz(eparzz,eparzzn);
 end
   epsilon{n}=ezz;
   b1{n}=z1;
   b2{n}=z2;
   b3{n}=z3;
%************    Calculating P Matrix     *********%
 p_11=-kx*inv(ezz)*ezx;
 p_14=knot*eye(2*N_ts+1)-(1/knot)*kx*inv(ezz)*kx;
 p_41=knot*exx-knot*exz*inv(ezz)*ezx;
 p_44=-exz*inv(ezz)*kx;
 pp=[p_11 p_14; p_41 p_44];
 %******************** End P Matrix *******************%
         [G1,D1] = eig(pp);
         D2=diag(D1);
         D_imag=imag(D2);
         D_real=real(D2);
         [D3, sortindex3]=sort(D_imag,'descend');
         D_real1=D_real(sortindex3);
         D=D_real1+1i*D3;
         Dm=diag(D);
         Du{n}=diag(D(1:2*N_ts+1));
         Dl{n}=diag(D(2*N_ts+2:4*N_ts+2));
         G=G1(:,sortindex3);
    if   n==Ns+Nm
         W=inv(G)*Z1;
    else
         W=inv(G)*Z;
    end
  wu{n}=W(1:2*N_ts+1,1:2*N_ts+1);
  wl{n}=W(2*N_ts+2:4*N_ts+2,1:2*N_ts+1);
  Z=G*[eye(2*N_ts+1);expm(-1i*delta(n)*Dl{n})*wl{n}*inv(wu{n})* expm
      (1i*delta(n)*Du{n})];
  matrix_zz{n} = [Z];
  end
    %%
% ************** Finging T0 and R  for Incidence Ap
```

```matlab
 **************%
    Ap=zeros(2*N_ts+1,1);
    Ap(N_ts+1,1)=1;
    zu=Z(1:2*N_ts+1, 1:2*N_ts+1);
    zl=Z(2*N_ts+2:4*N_ts+2,1:2*N_ts+1);
    f1=[zu  -yne; zl  -ynh];
    YP=[ype;yph];
    TR=inv(f1)*YP*Ap;
    T0=TR(1:2*N_ts+1,1);
    R=TR(2*N_ts+2:4*N_ts+2,1);
    matrix_tt{1}=T0;
%******* calculating T matrix   *********************%
  T=T0;
   for nnn=1:Nd+Ng+Nm
       T=inv(wu{nnn})*expm(1i*delta(nnn)*Du{nnn})*T;
  matrix_tt{nnn+1}=T;
 end
   %********************* End T Matrix  *****************%
    sumR=0;
    sumT=0;
  for  n1=1:2*N_ts+1
     kzr=real(kzn./(knot*cos(theta)));
     Rpp=(abs(R(n1)')^2)*kzr(n1);
     Tpp=(abs(T(n1)')^2)*kzr(n1);
     sumR=sumR+Rpp;
     sumT=sumT+Tpp;
  end
    App(vv)=1-(sumR+sumT);
    vv=vv+1;
end
if dd==1;
h1= plot(di:dt:df,  App, 'k','linewidth',4);
elseif dd==2;
h2= plot(di:dt:df,  App, '-.b','linewidth',4);
else
h3= plot(di:dt:df,  App, ':r','linewidth',4);
end
hold all
```

```
end
 xlabel('$\theta$ (deg)','IN_tserpreter','latex', 'FoN_tsSize', 24);
 ylabel('$A_{p}$','IN_tserpreter','latex','FoN_tsSize', 24);
 ax=gca;
 ax.FoN_tsSize=20;
 h = legend([h1,h2,h3],{'L_{c}= 1000 nm','L_{c}= 2000 nm','L_{c}=
    3000 nm'}, 'location' ,'north');
 h.IN_tserpreter = 'latex'
 set(h,'IN_tserpreter','tex')
 legend show

%******** Function for Finding Permittivity   ********%
function epsn= eps_ctf(z,n,epd,epm,d1,d2,L,L1)
CD=d2-d1;
y=(L1/pi)*asin((d2-z)/CD);
B=epm-epd;
%%
%********    Permittivity for n=0    ********%
 if n == 0
    if z<=d1
        epsn=epd;
 elseif z<d2 && z>d1
         epsn =(epd*(L - L1 + 2*y) +epm*(L1 - 2*y))/L;
 elseif z>=d2
         epsn=epm;
 end
 end
 %%
% ********    Permittivity for n#0   ********%
 if n~= 0
    if z<d2 && z>d1
         epsn = (B*exp(-1i*n*(L1 - y)*2*pi/L) -B*exp(-1i*n*y*2*pi/L))
            * 1i/(n*2*pi);
 elseif z<=d1
         epsn=0;
   elseif z>=d2
         epsn=0;
 end
 end
end
```

A.3 Absorptance A_p and A_s in the Grating-Coupled Configuration

```matlab
clc
clear all
close all
global epctf epm  d1 d2 d3  L L1  z1 z2 z3 N_ts  ;
%******* Defining Variables *******%
mu_0=4*pi*10^-7;              % Permability of free space
ep_0 = 8.854*10^-12;         % Permitivity of free space
nm=10^(-9);
lambda_0 = 633*nm;           % Free space wavelength
eta_0 =sqrt(mu_0/ep_0);      % Impedance of the free space
epm=(0.05096+3.9245*1i)^2;   % Permittivity of metal
L = 900*nm;
for dd=1:3
    if dd==1
        d1 =1000*nm;    % Thickness of CTF
    elseif dd==2
        d1 =2000*nm;
    else
        d1 =3000*nm;
    end
    d2 = d1 + 20*nm;   % Grating thickness
d3 = d2 + 30*nm;          % Metal  film thickness
L1 = 0.5*L;
N_ts = 15;
Nd = 50;
Ng = 30;
Nm=10;
Ns = Nd + Ng;
gamma_deg = (30*pi)/180;    %Angle of morphology
sz = [cos(gamma_deg) -sin(gamma_deg) 0 ; sin(gamma_deg) cos(
   gamma_deg) 0; 0 0 1];
chiv=20*pi/180; % Vapor deposition angle
        chi=atan(3.1056*tan(chiv));
        v=2*chiv/pi;
        sy= [cos(chi) 0 -sin(chi); 0 1 0; sin(chi) 0  cos(chi)];
  % CTF Permittivity
```

```matlab
         epa= (1.1961 +1.5439*v - 0.7719*v^2)^2;
         epb= (1.4600 + 1.0400*v-0.5200*v^2)^2;
         epc= (1.3532 + 1.2296*v - 0.6148*v^2)^2;
       epref=[epb 0 0; 0 epc 0; 0 0 epa];
         epctf=sz*sy*epref*inv(sy)*inv(sz);
knot=(2*pi)/lambda_0;  % wave number of free space
vv=1;
psi=30*pi/180;  % incident angle
% ****** End Defining Variables  ******%
%%
di=0;
dt=0.1;
df=89;
vv= 1;
for NN=di:dt:df
   theta=NN*pi/180;
    disp(NN);
    y1=0;
%****** Begin Finging wavenumbers *****%
 for n1=-N_ts:1:N_ts
      y1=y1+1;
      kxnn(y1)=knot*cos(psi)*sin(theta)+(n1*2*pi)/L;
      ky=knot*sin(psi)*sin(theta);
      kxy(y1)=sqrt(kxnn(y1)^2+ky^2);
  if ky==0 && kxnn(y1)<0
       kxy(y1)=-sqrt(kxnn(y1)^2+ky^2);
     else
      kxy(y1)=sqrt(kxnn(y1)^2+ky^2);
      end
  if knot^2 >= kxy(y1)^2
           kzn(y1) = sqrt(knot^2 - kxy(y1)^2);
 elseif knot^2 < kxy(y1)^2
          kzn(y1) = 1i*sqrt(-knot^2 + kxy(y1)^2);
  end
     end
kx = diag(kxnn);
%************ End Finging wavenumbers *********************%
%************* Finding Y Matrices ****************%
yph=[-diag((1/knot).*kzn.*kxnn./kxy)   diag(ky./kxy); -diag((1/knot)
```

```matlab
          .* kzn .* ky ./ kxy )   -diag ( kxnn ./ kxy )   ];
ynh=[ diag ((1/ knot ) .* kzn .* kxnn ./ kxy )  diag ( ky ./ kxy ); diag ((1/ knot ) .*
    kzn .* ky ./ kxy )    -diag ( kxnn ./ kxy )  ];
ype=[-diag ( ky ./ kxy )      -diag ((1/ knot ) .* kzn .* kxnn ./ kxy ); diag ( kxnn ./
    kxy )  -diag ((1/ knot ) .* kzn .* ky ./ kxy )];
yne=[-diag ( ky ./ kxy )   diag ((1/ knot ) .* kzn .* kxnn ./ kxy ); diag ( kxnn ./ kxy )
      diag ((1/ knot ) .* kzn .* ky ./ kxy )];
 ypos =[ ype ; yph ];
 yneg =[ yne ; ynh ];
 Z1=[ ype ; yph ];
 temp1 =( Ns+Nm+1: -1:1);
 mm=length ( temp1 );
 matrix_zz {Nd+Ng+Nm+1} = Z1;
 for  n=Ns+Nm: -1:1
%%
%********************* Permittivity For metal Region
    *************%
 if  n>Ns
        delta (n) =( d3-d2 )/Nm;
        x1 = d2- (d2 - d3 ) *(n - Ns )/Nm;
        x2 = d2 - (d2 - d3 ) *(n - 1 - Ns )/Nm;
        z1 = 0.5 *( x1 + x2 );
for  n3 =0:2* N_ts
    eparxx ( n3+1)=permctf (z1 , n3 ,0 , epm , d1 , d2 , L , L1 );
    eparxxn ( n3+1)=permctf (z1 ,- n3 ,0 , epm , d1 , d2 , L , L1 );
    eparxy ( n3+1)=permctf (z1 , n3 ,0 ,0 , d1 , d2 , L , L1 );
    eparxyn ( n3+1)=permctf (z1 ,- n3 ,0 ,0 , d1 , d2 , L , L1 );
    eparxz ( n3+1)=permctf (z1 , n3 ,0 ,0 , d1 , d2 , L , L1 );
    eparxzn ( n3+1)=permctf (z1 ,- n3 ,0 ,0 , d1 , d2 , L , L1 );
    eparyx ( n3+1)=permctf (z1 , n3 ,0 ,0 , d1 , d2 , L , L1 );
    eparyxn ( n3+1)=permctf (z1 ,- n3 ,0 ,0 , d1 , d2 , L , L1 );
    eparyy ( n3+1)=permctf (z1 , n3 ,0 , epm , d1 , d2 , L , L1 );
    eparyyn ( n3+1)=permctf (z1 ,- n3 ,0 , epm , d1 , d2 , L , L1 );
    eparyz ( n3+1)=permctf (z1 , n3 ,0 ,0 , d1 , d2 , L , L1 );
    eparyzn ( n3+1)=permctf (z1 ,- n3 ,0 ,0 , d1 , d2 , L , L1 );
    eparzx ( n3+1)=permctf (z1 , n3 ,0 ,0 , d1 , d2 , L , L1 );
    eparzxn ( n3+1)=permctf (z1 ,- n3 ,0 ,0 , d1 , d2 , L , L1 );
    eparzy ( n3+1)=permctf (z1 , n3 ,0 ,0 , d1 , d2 , L , L1 );
    eparzyn ( n3+1)=permctf (z1 ,- n3 ,0 ,0 , d1 , d2 , L , L1 );
```

```matlab
    eparzz(n3+1)=permctf(z1,n3,0,epm,d1,d2,L,L1);
    eparzzn(n3+1)=permctf(z1,-n3,0,epm,d1,d2,L,L1);
end
     exx=toeplitz(eparxx,eparxxn);
     exy=toeplitz(eparxy,eparxyn);
    exz=toeplitz(eparxz,eparxzn);
    eyx=toeplitz(eparyx,eparyxn);
     eyy=toeplitz(eparyy,eparyyn);
     eyz=toeplitz(eparyz,eparyzn);
    ezx=toeplitz(eparzx,eparzxn);
    ezy=toeplitz(eparzy,eparzyn);
    ezz=toeplitz(eparzz,eparzzn);
%*************** End Metal Permittivity ********************%
elseif   n<=Nd+Ng && n>Nd
        % ********** Start Grating Permittivity **************%%%
         delta(n)=(d2-d1)/Ng;
         x3 = d1 - (d1 - d2)*(n - Nd)/Ng;
         x4 = d1 - (d1 - d2)*(n - 1 - Nd)/Ng;
         z2 = 0.5*(x3 + x4);
  for q3=0:2*N_ts
    eparxx(q3+1)=permctf(z2,q3,epctf(1,1),epm,d1,d2,L,L1);
    eparxxn(q3+1)=permctf(z2,-q3,epctf(1,1),epm,d1,d2,L,L1);
    eparxy(q3+1)=permctf(z2,q3,epctf(1,2),0,d1,d2,L,L1);
    eparxyn(q3+1)=permctf(z2,-q3,epctf(1,2),0,d1,d2,L,L1);
    eparxz(q3+1)=permctf(z2,q3,epctf(1,3),0,d1,d2,L,L1);
    eparxzn(q3+1)=permctf(z2,-q3,epctf(1,3),0,d1,d2,L,L1);
    eparyx(q3+1)=permctf(z2,q3,epctf(2,1),0,d1,d2,L,L1);
    eparyxn(q3+1)=permctf(z2,-q3,epctf(2,1),0,d1,d2,L,L1);
    eparyy(q3+1)=permctf(z2,q3,epctf(2,2),epm,d1,d2,L,L1);
    eparyyn(q3+1)=permctf(z2,-q3,epctf(2,2),epm,d1,d2,L,L1);
    eparyz(q3+1)=permctf(z2,q3,epctf(2,3),0,d1,d2,L,L1);
    eparyzn(q3+1)=permctf(z2,-q3,epctf(2,3),0,d1,d2,L,L1);
    eparzx(q3+1)=permctf(z2,q3,epctf(3,1),0,d1,d2,L,L1);
    eparzxn(q3+1)=permctf(z2,-q3,epctf(3,1),0,d1,d2,L,L1);
    eparzy(q3+1)=permctf(z2,q3,epctf(3,2),0,d1,d2,L,L1);
    eparzyn(q3+1)=permctf(z2,-q3,epctf(3,2),0,d1,d2,L,L1);
    eparzz(q3+1)=permctf(z2,q3,epctf(3,3),epm,d1,d2,L,L1);
    eparzzn(q3+1)=permctf(z2,-q3,epctf(3,3),epm,d1,d2,L,L1);
end
```

```matlab
exx=toeplitz(eparxx,eparxxn);
exy=toeplitz(eparxy,eparxyn);
exz=toeplitz(eparxz,eparxzn);
eyx=toeplitz(eparyx,eparyxn);
eyy=toeplitz(eparyy,eparyyn);
eyz=toeplitz(eparyz,eparyzn);
ezx=toeplitz(eparzx,eparzxn);
ezy=toeplitz(eparzy,eparzyn);
ezz=toeplitz(eparzz,eparzzn);
    %************* Permittivity for  CTF *************%
 elseif  n<= Nd
            delta(n)=d1/Nd;
            x5 = (d1)*n/Nd;
            x6 = (d1)*(n- 1)/Nd;
            z3 = 0.5*(x5 + x6);
 for  j1 =0:2*N_ts
    eparxx(j1+1)=permctf(z3,j1,epctf(1,1),0,d1,d2,L,L1);
    eparxxn(j1+1)=permctf(z3,-j1,epctf(1,1),0,d1,d2,L,L1);
    eparxy(j1+1)=permctf(z3,j1,epctf(1,2),0,d1,d2,L,L1);
    eparxyn(j1+1)=permctf(z3,-j1,epctf(1,2),0,d1,d2,L,L1);
    eparxz(j1+1)=permctf(z3,j1,epctf(1,3),0,d1,d2,L,L1);
    eparxzn(j1+1)=permctf(z3,-j1,epctf(1,3),0,d1,d2,L,L1);
    eparyx(j1+1)=permctf(z3,j1,epctf(2,1),0,d1,d2,L,L1);
    eparyxn(j1+1)=permctf(z3,-j1,epctf(2,1),0,d1,d2,L,L1);
    eparyy(j1+1)=permctf(z3,j1,epctf(2,2),0,d1,d2,L,L1);
    eparyyn(j1+1)=permctf(z3,-j1,epctf(2,2),0,d1,d2,L,L1);
    eparyz(j1+1)=permctf(z3,j1,epctf(2,3),0,d1,d2,L,L1);
    eparyzn(j1+1)=permctf(z3,-j1,epctf(2,3),0,d1,d2,L,L1);
    eparzx(j1+1)=permctf(z3,j1,epctf(3,1),0,d1,d2,L,L1);
    eparzxn(j1+1)=permctf(z3,-j1,epctf(3,1),0,d1,d2,L,L1);
    eparzy(j1+1)=permctf(z3,j1,epctf(3,2),0,d1,d2,L,L1);
    eparzyn(j1+1)=permctf(z3,-j1,epctf(3,2),0,d1,d2,L,L1);
    eparzz(j1+1)=permctf(z3,j1,epctf(3,3),0,d1,d2,L,L1);
    eparzzn(j1+1)=permctf(z3,-j1,epctf(3,3),0,d1,d2,L,L1);
end
exx=toeplitz(eparxx,eparxxn);
exy=toeplitz(eparxy,eparxyn);
exz=toeplitz(eparxz,eparxzn);
eyx=toeplitz(eparyx,eparyxn);
```

```matlab
eyy=toeplitz(eparyy,eparyyn);
eyz=toeplitz(eparyz,eparyzn);
ezx=toeplitz(eparzx,eparzxn);
ezy=toeplitz(eparzy,eparzyn);
ezz=toeplitz(eparzz,eparzzn);
 end
   epsilon{n}=ezz;
   b1{n}=z1;
   b2{n}=z2;
   b3{n}=z3;
%************    Calculating P Matrix      *********%
 p_11=-kx*inv(ezz)*ezx;
 p_12=-kx*inv(ezz)*ezy;
 p_13=(ky/knot)*kx*inv(ezz);
 p_14=knot*eye(2*N_ts+1)-(1/knot)*kx*inv(ezz)*kx;
 p_21=-ky*inv(ezz)*ezx;
 p_22=-ky*inv(ezz)*ezy;
 p_23=-knot*eye(2*N_ts+1)+(ky^2/knot)*inv(ezz);
 p_24=-(ky/knot)*inv(ezz)*kx;
 p_31=-knot*eyx+knot*eyz*inv(ezz)*ezx-(ky/knot)*kx;
 p_32=(1/knot)*kx^2-knot*eyy+knot*eyz*inv(ezz)*ezy;
 p_33=-ky*eyz*inv(ezz);
 p_34=eyz*inv(ezz)*kx;
 p_41=knot*exx-knot*exz*inv(ezz)*ezx-(ky^2/knot)*eye(2*N_ts+1);
 p_42=knot*exy-knot*exz*inv(ezz)*ezy+(ky/knot)*kx;
 p_43=ky*exz*inv(ezz);
 p_44=-exz*inv(ezz)*kx;
 p=[p_11 p_12 p_13 p_14; p_21 p_22 p_23 p_24; p_31 p_32 p_33 p_34;
    p_41 p_42 p_43 p_44];
%******************** End P Matrix *******************%
[G1,D1] = eig(p);
D2=diag(D1);
D_imag=imag(D2);
D_real=real(D2);
[D3, sortindex3]=sort(D_imag,'descend');
D_real1=D_real(sortindex3);
D=D_real1+1i*D3;
Dm=diag(D);
Du{n}=diag(D(1:(4*N_ts)+2));
```

```matlab
Dl{n}=diag(D((4*N_ts)+3:(8*N_ts)+4));
G=G1(:,sortindex3);
            if    n==Ns+Nm
                W=inv(G)*Z1;
            else
                W=inv(G)*Z;
             end
wu{n}=W(1:4*N_ts+2,1:4*N_ts+2);
wl{n}=W(4*N_ts+3:8*N_ts+4,1:4*N_ts+2);
Z=G*[eye(4*N_ts+2);expm(-1i*delta(n)*Dl{n})*wl{n}*inv(wu{n})* expm(1
    i*delta(n)*Du{n})];
 matrix_zz{n} = [Z];
  end
    %%
% *******   Finging T0 and R  for Incidence Ap  *******%
Ap=zeros(4*N_ts+2,1);
Ap(3*N_ts+2,1)=1;
zu=Z(1:4*N_ts+2,  1:4*N_ts+2);
 zl=Z(4*N_ts+3:8*N_ts+4,1:4*N_ts+2);
 f1=[zu  -yne; zl  -ynh];
YP=[ype;yph];
TR=inv(f1)*YP*Ap;
T0=TR(1:4*N_ts+2,1);
R=TR(4*N_ts+3:8*N_ts+4,1);
 matrix_tt{1}=T0;
 %******* calculating T matrix   *******************%
  T=T0;
 for nnn=1:Nd+Ng+Nm
      T=inv(wu{nnn})*expm(1i*delta(nnn)*Du{nnn})*T;
 matrix_tt{nnn+1}=T;
end
  %******** End T Matrix  *******%


  %********   $p$ Incident , $s$ Reflected   *******%
    rs=R(1:2*N_ts+1,1);
  %******** $p$ Incident , $p$ Reflected   *******%
     rp=R(2*N_ts+2:4*N_ts+2,1);
  %********  $p$ Incident , $s$ Transmitted *******%
```

```matlab
      ts=T(1:2*N_ts+1,1);
  %********     $p$ Incident , $p$ Reflected    ********%
      tp=T(2*N_ts+2:4*N_ts+2,1);
sumR=0;
sumT=0;
 for   n1=1:2*N_ts+1
      kzr=real(kzn./(knot*cos(theta)));
      Rsp=(abs(rs(n1)')^2)*kzr(n1);
      Rpp=(abs(rp(n1)')^2)*kzr(n1);
      Tsp=(abs(ts(n1)')^2)*kzr(n1);
      Tpp=(abs(tp(n1)')^2)*kzr(n1);
      sumR=sumR+Rpp+Rsp;
      sumT=sumT+Tpp+Tsp;
  end
    % *********** Finging T0 and R  for Incidence As*************%
As=zeros(4*N_ts+2,1);
As(N_ts+1,1)=1;
zus=Z(1:4*N_ts+2, 1:4*N_ts+2);
zls=Z(4*N_ts+3:8*N_ts+4,1:4*N_ts+2);
f1s=[zus  -yne; zls   -ynh];
YPs=[ype;yph];
TRs=inv(f1s)*YPs*As;
T0s=TRs(1:4*N_ts+2,1);
Rs=TRs(4*N_ts+3:8*N_ts+4,1);
matrix_tts{1}=T0s;
  %%
Ts=T0s;
   %****************** calculating T matrix   ***************%
for  nnn=1:Nd+Ng+Nm
      Ts=inv(wu{nnn})*expm(1i*delta(nnn)*Du{nnn})*Ts;
matrix_tts{nnn+1}=Ts;
end
  %********************** End T Matrix   ******************%
    %%
    %********     $s$ Incident , $s$ Reflected   ******** %
    rs1=Rs(1:2*N_ts+1,1);
    %********     $s$ Incident , $p$ Reflected   ******** %
    rp1=Rs(2*N_ts+2:4*N_ts+2,1);
    %********     $s$ Incident , $s$ Transmitted  ******** %
```

```matlab
        ts1=Ts(1:2*N_ts+1,1);
        %********* $s$ Incident , $p$ Transmitted  ******** %
        tp1=Ts(2*N_ts+2:4*N_ts+2,1);
    sumRs=0;
    sumTs=0;
     for   n1=1:2*N_ts+1
        kzr=real(kzn./(knot*cos(theta)));
        Rss=(abs(rs1(n1)')^2)*kzr(n1);
        Rps=(abs(rp1(n1)')^2)*kzr(n1);
        Tss=(abs(ts1(n1)')^2)*kzr(n1);
        Tps=(abs(tp1(n1)')^2)*kzr(n1);
        sumRs=sumRs+Rss+Rps;
        sumTs=sumTs+Tss+Tps;
    end
      %*********   Absorptance As            ******** %
       Ass(vv)=1-(sumRs+sumTs);
      %*********   Absorptance Ap    ******** %
       App(vv)=1-(sumR+sumT);
      vv=vv+1;
end
if dd==1;
h1= plot(di:dt:df,   App, 'k','linewidth',4);
elseif dd==2;
h2= plot(di:dt:df,   App, '-.b','linewidth',4);
else
h3= plot(di:dt:df,   App, ':r','linewidth',4);
end
hold all

end
xlabel('$\theta$ (deg)','IN_tserpreter','latex', 'FoN_tsSize', 24);
 ylabel('$A_{p}$','IN_tserpreter','latex','FoN_tsSize', 24);
 ax=gca;
 ax.FoN_tsSize=20;
h = legend([h1,h2,h3],{'L_{c}= 1000 nm','L_{c}= 2000 nm','L_{c}=
    3000 nm'}, 'location' ,'north');
h.IN_tserpreter = 'latex'
set(h,'IN_tserpreter','tex')
legend show
```

```matlab
%******** Function for Finding Permittivity ********%
function epsn= eps_ctf(z,n,epd,epm,d1,d2,L,L1)
CD=d2-d1;
y=(L1/pi)*asin((d2-z)/CD);
B=epm-epd;
%%
%******** Permittivity for n=0 ********%
  if n == 0
     if z<=d1
        epsn=epd;
  elseif z<d2 && z>d1
         epsn =(epd*(L - L1 + 2*y) +epm*(L1 - 2*y))/L;
  elseif z>=d2
         epsn=epm;
  end
  end
 %%
% ******** Permittivity for n#0 ********%
 if n~= 0
    if z<d2 && z>d1
         epsn = (B*exp(-1i*n*(L1 - y)*2*pi/L) -B*exp(-1i*n*y*2*pi/L))
            * 1i/(n*2*pi);
  elseif z<=d1
         epsn =0;
   elseif z>=d2
         epsn =0;
  end
  end
end
```

A.4 Newton-Raphson Method to Find q in the Canonical Boundary-Value Problem

```matlab
%****** *** Canonical Solution for Glass/CTF Interface ************%
 % ***************   z > 0 occupied by a glass   **************%
% ***************   z < 0 occupied by a CTF   **************%
 clc
 clear all
 format long
%************ Defining Inputs   **************%
```

```matlab
nm=10^-9;
lambda0 = 633*nm;
knot=(2*pi)/lambda0;
psi= 30*pi/180
 delta=10^(-14);
 error=10^(-8);
 %************    Initial  guess  ************%
 q=(1+0.01*1i)*knot;
 %*****************       Newton  Raphson  Method    *************%
  for  i=1:200
detM=fun_dyak(q, lambda0, psi);
detMd=fun_dyak(q+delta*q, lambda0,psi);
 dff=(detMd-detM)/(delta*q);
 f=q-detM/dff;
err=abs(detM);
%*******     checking  the  amount  of  error  at  each  iteration
    *********%
if  err<=error
break
end
q=f;
disp(q/knot);
disp(i);
 end

%************* Function  for  Solving  the  Dispersion  Equation
    *********%
function  detr= fun_dyak(q, lambda0, psi)
%***************       Defining  Inputs   *******************%
% permesbility  of  free  space
muo=4*pi*10^-7;
%free  space  permittivity
epso = 8.854*10^-12;
eta0 =sqrt(muo/epso);
gamma = (15*pi)/180;
chiv=20*pi/180;
chi=atan(3.1056*tan(chiv));
v=2*chiv/pi;
epsa= (1.1961 +1.5439*v - 0.7719*v^2)^2;
epsb= (1.4600 + 1.0400*v-0.5200*v^2)^2;
```

```matlab
epsc= (1.3532 + 1.2296*v - 0.6148*v^2)^2;
ns=1.5+0.001*1i;
knot=(2*pi)/lambda0;
omg=knot/sqrt(muo*epso);
% ************* [P] Matrix for CTF *************************%
pa_11=(q*(epsa-epsb)*cos(gamma)*cos(chi)*cos(psi)*sin(chi))/(epsa*
    cos(chi)^2+epsb*sin(chi)^2);
pa_12=(q*(epsa-epsb)*cos(chi)*cos(psi)*sin(gamma)*sin(chi))/(epsa*
    cos(chi)^2+epsb*sin(chi)^2);
pa_13=((q^2)*cos(psi)*sin(psi))/(epso*omg*(epsa*cos(chi)^2+epsb*sin(
    chi)^2));
pa_14=omg*muo-(q^2*cos(psi)^2)/(omg*epso*(epsa*cos(chi)^2+epsb*sin(
    chi)^2));
pa_21=(q*(epsa-epsb)*cos(gamma)*cos(chi)*sin(chi)*sin(psi))/(epsa*
    cos(chi)^2+epsb*sin(chi)^2);
pa_22=(q*(epsa-epsb)*cos(chi)*sin(gamma)*sin(chi)*sin(psi))/(epsa*
    cos(chi)^2+epsb*sin(chi)^2);
pa_23=-omg*muo+(q^2*sin(psi)^2)/(omg*epso*(epsa*cos(chi)^2+epsb*sin(
    chi)^2));
pa_24=-((q^2)*cos(psi)*sin(psi))/(omg*epso*(epsa*cos(chi)^2+epsb*sin
    (chi)^2));
pa_31 = (omg*epso*cos(gamma)*((epsb*epsc)+(epsa*(epsc-2*epsb))+(epsa
    -epsb)*epsc*cos(2*chi))*sin(gamma))/(2*(epsa*cos(chi)^2+epsb*sin(
    chi)^2))-((q^2)*cos(psi)*sin(psi))/(omg*muo);
pa_32=-omg*epso*epsc*cos(gamma)^2+((q^2)*cos(psi)^2)/(omg*muo)-omg*
    epso*(sin(gamma)^2)*(epsb*cos(chi)^2+epsa*sin(chi)^2)+(omg*epso
    *((epsa-epsb)^2)*(cos(chi)^2)*(sin(gamma)^2)*(sin(chi)^2))/(epsa*
    cos(chi)^2+epsb*sin(chi)^2);
pa_33=(q*(epsa-epsb)*cos(chi)*sin(gamma)*sin(chi)*sin(psi))/(epsa*
    cos(chi)^2+epsb*sin(chi)^2);
pa_34=(q*(-epsa+epsb)*cos(chi)*sin(gamma)*sin(chi)*cos(psi))/(epsa*
    cos(chi)^2+epsb*sin(chi)^2);
pa_41=omg*epso*epsc*sin(gamma)^2+(omg*epso*epsa*epsb*cos(gamma)^2)/(
    epsa*cos(chi)^2+epsb*sin(chi)^2)-q^2*sin(psi)^2/(omg*muo);
pa_42=(omg*epso*(2*epsa*epsb-epsa*epsc-epsb*epsc-(epsa-epsb)*epsc*
    cos(2*chi))*sin(2*gamma))/(4*(epsa*cos(chi)^2+epsb*sin(chi)^2))
    +((q^2)*cos(psi)*sin(psi))/(omg*muo);
pa_43= (q*(-epsa+epsb)*cos(gamma)*sin(chi)*sin(psi)*cos(chi))/(epsa*
    cos(chi)^2+epsb*sin(chi)^2);
```

```matlab
pa_44=(q*(epsa-epsb)*cos(gamma)*cos(chi)*cos(psi)*sin(chi))/(epsa*
    cos(chi)^2+epsb*sin(chi)^2);
pa=[pa_11 pa_12 pa_13 pa_14; pa_21 pa_22 pa_23 pa_24; pa_31 pa_32
    pa_33 pa_34; pa_41 pa_42 pa_43 pa_44];
%*** Selection of Eigenvalues and Eigenvectors  for z<0 ****%
[Ga, Da]=eig(pa);
        D2a=diag(Da);
        Da_imag=imag(D2a);
        Da_real=real(D2a);
        [D3a, sortindex3]=sort(Da_imag,'descend');
        Da_real1=Da_real(sortindex3);
        Da=Da_real1+1i*D3a;
        Dam=diag(Da);
        tna=Ga(:,sortindex3);
        t1=tna(1:4,1);
t2=tna(1:4,2);
%%
%****** Selection of eigenvalues and eigenvectors z>0 ********%
alpha_s=sqrt(knot^2*ns^2-q^2);
if imag(alpha_s)<0
    alpha_ss=-alpha_s;
    alpha_s=alpha_ss;
end
 fn=[-sin(psi) alpha_s*cos(psi)/knot; cos(psi) alpha_s*sin(psi)/knot
    ; alpha_s*cos(psi)/(knot*eta0) ns^2*sin(psi)/eta0;
    alpha_s*sin(psi)/(knot*eta0)  -ns^2*cos(psi)/eta0];
M=[t1 t2 -fn ];
 detr=det(M);
end
```

A.5   Finding q for High-Phase-Speed Dyakonov Surface Waves

```matlab
%****Canonical Solution for Uniaxial/Air Interface ****%
% **********z < 0 occupied by a air     **************%
% **********z > 0 occupied by  AZO/silicon   *************%
clc
clear all
close all
format long
%***************** Defining Inputs **************   %
```

105

```
nm=10^-9;
%************ Permittivity at different wavelengths    ********%
%  lambdao = 2.0000*10^-6;
% epba=7.0227+0.5299*1i;
% epbb=0.8999+2.0437*1i;
% epbc= epba;
%%
%* Permittivity of uniaxial material at lambdao= 2.8928*10^-6*%
%  lambdao = 2.8928*10^-6;
% epba=5.7128+1.6085*1i;
% epbb=-0.9819+6.5875*1i;
% epbc= epba;
%%
%* Permittivity of uniaxial material at lambdao=3.7855*10^(-6)*%
lambdao=3.7855*10^(-6);
epba=4.4029+3.0573*1i;
epbb=0.6351+13.0825*1i;
epbc=epba;
%%
%* Permittivity of uniaxial material at lambdao=8.9797*10^(-6)*%
% lambdao=8.9797*10^(-6);
% epba=-1.7747+16.0555*1i;
% epbb=16.9301+19.9579*1i;
% epbc=epba;
%%
knot=(2*pi)/lambdao;
delta=10^(-14);
 error=10^(-10);
 %***************** End Defining Inputs **************   %
 q=(1+0.1*1i)*knot;
 for i=1:20
detM=can_azo(q,  epba, epbb, epbc, lambdao,knot);
detMd=can_azo(q+delta*q,  epba, epbb, epbc, lambdao, knot);
 dff=(detMd-detM)/(delta*q);
 f=q-detM/dff ;
err=abs(detM);
%*********checking the amount of error at each iteration *********%
if err<=error
break
```

```matlab
end
q=f;
disp(q/knot);
disp(i);
 end

%*** Function for Solving the Dispersion Equation ***%
function detr_azo= can_azo(q, epba, epbb, epbc, lambdao, knot)
muo=4*pi*10^-7;
epso = 8.854*10^-12;
etao =sqrt(muo/epso);
omg=knot/sqrt(muo*epso);
psi=22*pi/180;
%************* Permittivity for AZO/Silicon **************%
epb=[epbb 0 0; 0 epbc 0; 0 0 epba];

%** [P] Matrix for AZO/Silicon **%
pb_11=(q*(epsa-epsb)*cos(gamma)*cos(chi)*cos(psi)*sin(chi))/(epsa*
    cos(chi)^2+epsb*sin(chi)^2);
pb_12=(q*(epsa-epsb)*cos(chi)*cos(psi)*sin(gamma)*sin(chi))/(epsa*
    cos(chi)^2+epsb*sin(chi)^2);
pb_13=((q^2)*cos(psi)*sin(psi))/(epso*omg*(epsa*cos(chi)^2+epsb*sin(
    chi)^2));
pb_14=omg*muo-(q^2*cos(psi)^2)/(omg*epso*(epsa*cos(chi)^2+epsb*sin(
    chi)^2));
pb_21=(q*(epsa-epsb)*cos(gamma)*cos(chi)*sin(chi)*sin(psi))/(epsa*
    cos(chi)^2+epsb*sin(chi)^2);
pb_22=(q*(epsa-epsb)*cos(chi)*sin(gamma)*sin(chi)*sin(psi))/(epsa*
    cos(chi)^2+epsb*sin(chi)^2);
pb_23=-omg*muo+(q^2*sin(psi)^2)/(omg*epso*(epsa*cos(chi)^2+epsb*sin(
    chi)^2));
pb_24=-((q^2)*cos(psi)*sin(psi))/(omg*epso*(epsa*cos(chi)^2+epsb*sin
    (chi)^2));
pb_31 = (omg*epso*cos(gamma)*((epsb*epsc)+(epsa*(epsc-2*epsb))+(epsa
    -epsb)*epsc*cos(2*chi))*sin(gamma))/(2*(epsa*cos(chi)^2+epsb*sin(
    chi)^2))-((q^2)*cos(psi)*sin(psi))/(omg*muo);
pb_32=-omg*epso*epsc*cos(gamma)^2+((q^2)*cos(psi)^2)/(omg*muo)-omg*
    epso*(sin(gamma)^2)*(epsb*cos(chi)^2+epsa*sin(chi)^2)+(omg*epso
    *((epsa-epsb)^2)*(cos(chi)^2)*(sin(gamma)^2)*(sin(chi)^2))/(epsa*
    cos(chi)^2+epsb*sin(chi)^2);
```

```matlab
pb_33=(q*(epsa-epsb)*cos(chi)*sin(gamma)*sin(chi)*sin(psi))/(epsa*
    cos(chi)^2+epsb*sin(chi)^2);
pb_34=(q*(-epsa+epsb)*cos(chi)*sin(gamma)*sin(chi)*cos(psi))/(epsa*
    cos(chi)^2+epsb*sin(chi)^2);
pb_41=omg*epso*epsc*sin(gamma)^2+(omg*epso*epsa*epsb*cos(gamma)^2)/(
    epsa*cos(chi)^2+epsb*sin(chi)^2)-q^2*sin(psi)^2/(omg*muo);
pb_42=(omg*epso*(2*epsa*epsb-epsa*epsc-epsb*epsc-(epsa-epsb)*epsc*
    cos(2*chi))*sin(2*gamma))/(4*(epsa*cos(chi)^2+epsb*sin(chi)^2))
    +((q^2)*cos(psi)*sin(psi))/(omg*muo);
pb_43= (q*(-epsa+epsb)*cos(gamma)*sin(chi)*sin(psi)*cos(chi))/(epsa*
    cos(chi)^2+epsb*sin(chi)^2);
pb_44=(q*(epsa-epsb)*cos(gamma)*cos(chi)*cos(psi)*sin(chi))/(epsa*
    cos(chi)^2+epsb*sin(chi)^2);
pb=[pb_11 pb_12 pb_13 pb_14; pb_21 pb_22 pb_23 pb_24; pb_31 pb_32
    pb_33 pb_34; pb_41 pb_42 pb_43 pb_44];
% ************* End [P] Matrix for AZO/Silicon ***************%
%** Selection of Eigenvalues and Eigenvectors for z<0 ***%
[Gb,Db] = eigs(pb);
        D1b=diag(Db);
        Db_imag=imag(D1b);
        Db_real=real(D1b);
     [D2b, sortindex2]=sort(Db_imag,'descend');
        Db_real1=Db_real(sortindex2);
        Db=Db_real1+1i*D2b;
        Db_m=diag(Db);
        tnb=Gb(:,sortindex2);
t1=tnb(1:4,3);
t2=tnb(1:4,4);
%*** Selection of Eigenvalues and Eigenvectors  for z<0 **%
ns=1;
alpha_s=sqrt(knot^2*ns^2-q^2);
if imag(alpha_s)>0
    alpha_ss=-alpha_s;
    alpha_s=alpha_ss;
end
 fn=[-sin(psi) alpha_s*cos(psi)/knot; cos(psi) alpha_s*sin(psi)/knot
    ; alpha_s*cos(psi)/(knot*etao) ns^2*sin(psi)/etao;
    alpha_s*sin(psi)/(knot*etao)  -ns^2*cos(psi)/etao];
M=[t1 t2 -fn ];
```

```matlab
  detr_azo=det(M);
end
```

A.6   Forward Bruggemann Homogenization Formalism

```matlab
clc
clear all
close all
format long
%% defining input parameters
mu0 = 4*pi*10^-7;                    %  permebility of free space
ep0 = 8.854*10^-12;                  %  permitivety of free space
% lmda0 = 650*10^-9;                 % wave length
% chiv= 15*(pi/180);                 %  vapor deposition angle
% chi = atan(3.1056*tan(chiv));      %  angle of inclination
%% Nanoscale parameters for Bruggeman homogenization
eps=(2.2999)^2; % permitivity for solid region
epv=(1.85)^2;   % permitivity for void region
fs=0.4439;      %  solid volume fraction
fv=1-fs;        %  void volume fraction
gts=15;         % shape parameter
gbs=2.4322;
gtv=1;
gbv=1;
gt=15;          % shape parameter minor axis for void
%% Bruggemann Homogenization
%******** intialization of permitivity  ********%
ident = eye(3,3);
epr1 = ident*(epv*fv + eps*(1 - fv));
it=1;
%******** using jacobi iteration method ********%
for m1=1:20
    it=it+1
    %%
%******** depolarization dyadic for void region   ********%
    Dv = fun_void(epr1, gbv, gtv,gt);
    %%
%******** Depolarization dyadic for solid region   ********%
    Ds = fun_solid(epr1, gbs,  gts, gt);
    %%
```

```matlab
%********* main algorithm of iterated function  *********%

    As = ident + Ds.*(eps*ident − epr1);          % factor for solid
    Av = ident + Dv.*(epv*ident − epr1);          % factor for void
    epBR = (inv(fs*Av + fv*As)).*(fs*eps*Av + fv*epv*As);
    epr = epBR;
    %%
 %********* depolarization dyadic for void region  *********%
    Dv1 = fun_void(epr, gbv, gtv, gt);
    %%
 %*********Depolarization dyadic for solid region  *********%
    Ds1 = fun_solid(epr, gbs,  gts, gt);
    %%
 %*********    main algorithm of iterated function   *********%
    As1 = ident + Ds1.*(eps*ident − epr);        % factor for solid
    Av1 = ident + Dv1.*(epv*ident − epr);        % factor for void
    epBR1 = (inv(fs*Av1 + fv*As1)).*(fs*eps*Av1 + fv*epv*As1);
    epr1 = epBR1;
 if abs(epr1(1,1))−abs(epr(1,1))<=10^(−20) && abs(epr1(2,2))−abs(epr
    (2,2))<=10^(−20) && abs(epr1(3,3))−abs(epr(3,3))<=10^(−20)
     disp("Got the solution")
        break
    end
display(it)
end
epa = epr1(1,1);
epb = epr1(2,2);
epc = epr1(3,3);

%%
%** depolarization dyadic for solid region of CTF ***%
function Ds=fun_solid(epr, gbs, gts, gt)
format long
iter=24;
%%
%******** calculation of Depolarization dyadic ********%
% gts=15;
[nds, wts]=leg(−1,1,iter); %function for finding weights and nodes
%******** points on which function evaluate  ********%
for n=1:iter
```

```matlab
    twt(n)=(pi/4)*wts(n);        % theta weights for different
        interval
    tnd(n)=(pi/4)*(nds(n)+1);    % theta x-points for different
        interval
    pwt(n)=(pi/4)*wts(n);        % phi weights for different
        interval
    pnd(n)=(pi/4)*(nds(n)+1);    % phi x-points for different
        interval
end
for p=1:iter
    for q=1:iter
        %% inplementation of depolarization dyadic equation
        %% for the solid region
        den2(p,q)=epr(1,1)*(cos(pnd(m))^2)*(sin(tnd(n))^2)+epr(2,2)
            *(cos(tnd(n))^2)/(gts^2)+epr(3,3)*(sin(pnd(m))^2)*(sin(
            tnd(n))^2)/(gbs^2);
        fn2(p,q)=(cos(pnd(m))^2)*(sin(tnd(n))^3)/(den2(p,q));
        ft2(p,q)=(cos(tnd(n))^2)*(sin(tnd(n)))/((gts^2)*(den2(p,q)))
            ;
        fb2(p,q)=(sin(pnd(m))^2)*(sin(tnd(n))^3)/((gbs^2)*den2(p,q))
            ;
        d3n2(p,q)=twt(n)*pwt(m)*fn2(p,q);
        d3t2(p,q)=twt(n)*pwt(m)*ft2(p,q);
        d3b2(p,q)=twt(n)*pwt(m)*fb2(p,q);
    end
end
d3n_2=sum(sum(d3n2));
d3t_2=sum(sum(d3t2));
d3b_2=sum(sum(d3b2));
Ds=(8*[d3n_2 0 0; 0 d3t_2 0; 0 0 d3b_2])/(4*pi); % depolarization
    dyadic
end

%%
%******** depolarization dyadic for CTF  ********%
function Dv=fun_void(epr, gbv, gtv, gt)
format long

   % shape parameter major axis for void
iter=24;
```

```matlab
%% calculation of Depolarization dyadic
% gts=15;
[nds, wts]=leg(-1,1,iter); %function for finding weights and nodes
%********  points on which function evaluate ********%
for n=1:iter
    twt(n)=(pi/4)*wts(n);              % theta weights for different
        interval
    tnd(n)=(pi/4)*(nds(n)+1);          % theta x-points for different
        interval
    pwt(n)=(pi/4)*wts(n);              % phi weights for different
        interval
    pnd(n)=(pi/4)*(nds(n)+1);          % phi x-points for different
        interval
end
for p=1:iter
  for q=1:iter

 %%
 %** inplementation of depolarization dyadic equation   **%
 %%
 %********   for the void region    ********%
        den1(p,q)=epr(1,1)*(cos(pnd(m))^2)*(sin(tnd(n))^2)+epr(2,2)
            *(cos(tnd(n))^2)/(gtv^2)+epr(3,3)*(sin(pnd(m))^2)*(sin(
            tnd(n))^2)/(gbv^2);
        fn1(p,q)=(cos(pnd(m))^2)*(sin(tnd(n))^3)/(den1(p,q));
        ft1(p,q)=(cos(tnd(n))^2)*(sin(tnd(n)))/((gtv^2)*(den1(p,q)))
            ;
        fb1(p,q)=(sin(pnd(m))^2)*(sin(tnd(n))^3)/((gbv^2)*den1(p,q))
            ;
        d3n1(p,q)=twt(n)*pwt(m)*fn1(p,q);
        d3t1(p,q)=twt(n)*pwt(m)*ft1(p,q);
        d3b1(p,q)=twt(n)*pwt(m)*fb1(p,q);
    end
end
d3n_1=sum(sum(d3n1));
d3t_1=sum(sum(d3t1));
d3b_1=sum(sum(d3b1));
Dv=(8*[d3n_1 0 0; 0 d3t_1 0; 0 0 d3b_1])/(4*pi); % depolarization
    dyadic
```

end

A.7 Absorptance A_{p} in the Grating-Coupled Configuration for Optical Sensor

```matlab
clc
clear all
global ECTF epm d2 d1 L L1 d3 z1 z2 z3 N_t  ;
mu_0=4*pi*10^-7;
ep_0 = 8.854* 10^-12;
nm=10^(-9);
lambda_0 = 650*nm;
eta_0 =sqrt(mu_0/ep_0);
epm=(0.05096+1i*3.92451)^2;
L = 500*nm;
for fr=1:4
    if fr==1
      d1 = 1000*nm;
    elseif fr==2
        d1 = 2000*nm;
    elseif fr==3
        d1 = 3000*nm;
    else
        d1 = 4000*nm;
    end
d2 = d1 + 20*nm;
d3 = d2 + 30*nm;
L1 = 0.5*L;
N_t = 15;
Nd = 30;
Ng = 30;
Nm=10;
Ns = Nd + Ng;
gamma_deg = (30*pi)/180;
sz = [cos(gamma_deg) -sin(gamma_deg) 0 ; sin(gamma_deg) cos(
   gamma_deg) 0; 0 0 1];
chiv=15*pi/180;
        chi=atan(3.1056*tan(chiv));
        v=2*chiv/pi;
        sy= [cos(chi) 0 -sin(chi); 0 1 0; sin(chi) 0  cos(chi)];
```

```
%% nl=1.33
epa=2.845219423;
epb=3.17749538;
epc=3.17749538;
%%
    epref=[epb 0 0; 0 epc 0; 0 0 epa];
  ECTF=sz*sy*epref*inv(sy)*inv(sz);
knot=(2*pi)/lambda_0;
vv=1;
psi=0*pi/180;
% ********** End Defining Variables  *****************%
%%
di=0;
dt=0.1;
df=89;
for NN=di:dt:df
    theta = NN*pi/180;
    disp(NN);
    y1=0;
    for n1=-N_t:1:N_t
     y1=y1+1;
    kxnn(y1)=knot*cos(psi)*sin(theta)+(n1*2*pi)/L;
   ky=knot*sin(psi)*sin(theta);
   kxy(y1)=sqrt(kxnn(y1)^2+ky^2);
    if knot^2 >= kxy(y1)^2
     kzn(y1) = sqrt(knot^2 - kxy(y1)^2);
    elseif knot^2 < kxy(y1)^2
     kzn(y1) = 1i*sqrt(-knot^2 + kxy(y1)^2);
      end
   end
kx = diag(kxnn);
%*************** End Finding kzn  *********************%
%%
%************** Finding Y Matrices ****************%
 yph=[-diag((1/knot).*kzn.*kxnn./kxy)  diag(ky./kxy); -diag((1/knot)
     .*kzn.*ky./kxy)  -diag(kxnn./kxy) ];
ynh=[ diag((1/knot).*kzn.*kxnn./kxy)  diag(ky./kxy); diag((1/knot).*
    kzn.*ky./kxy)   -diag(kxnn./kxy) ];
```

```matlab
ype=[-diag(ky./kxy)        -diag((1/knot).*kzn.*kxnn./kxy); diag(kxnn./
    kxy)   -diag((1/knot).*kzn.*ky./kxy)];
yne=[-diag(ky./kxy)  diag((1/knot).*kzn.*kxnn./kxy); diag(kxnn./kxy)
      diag((1/knot).*kzn.*ky./kxy)];
 ypos=[ype;yph];
 yneg=[yne;ynh];
 Z1=[ype;yph];
 temp1=(Ns+Nm+1:-1:1);
 mm=length(temp1);
 matrix_zz{Nd+Ng+Nm+1} = Z1;
 for n=Ns+Nm:-1:1
%%
%******************** Permittivity For metal Region
    *************%
 if n > Ns
    delta(n)=(d3-d2)/Nm;
        x1 = d2- (d2 - d3)*(n - Ns)/Nm;
         x2 = d2 - (d2 - d3)*(n - 1 - Ns)/Nm;
         z1 = 0.5*(x1 + x2);
for n3=0:2*N_t
    eparxx(n3+1)=functf(z1,n3,0,epm,d1,d2,L,L1);
    eparxxn(n3+1)=functf(z1,-n3,0,epm,d1,d2,L,L1);
    eparxy(n3+1)=functf(z1,n3,0,0,d1,d2,L,L1);
    eparxyn(n3+1)=functf(z1,-n3,0,0,d1,d2,L,L1);
    eparxz(n3+1)=functf(z1,n3,0,0,d1,d2,L,L1);
    eparxzn(n3+1)=functf(z1,-n3,0,0,d1,d2,L,L1);
    eparyx(n3+1)=functf(z1,n3,0,0,d1,d2,L,L1);
    eparyxn(n3+1)=functf(z1,-n3,0,0,d1,d2,L,L1);
    eparyy(n3+1)=functf(z1,n3,0,epm,d1,d2,L,L1);
    eparyyn(n3+1)=functf(z1,-n3,0,epm,d1,d2,L,L1);
    eparyz(n3+1)=functf(z1,n3,0,0,d1,d2,L,L1);
    eparyzn(n3+1)=functf(z1,-n3,0,0,d1,d2,L,L1);
    eparzx(n3+1)=functf(z1,n3,0,0,d1,d2,L,L1);
    eparzxn(n3+1)=functf(z1,-n3,0,0,d1,d2,L,L1);
    eparzy(n3+1)=functf(z1,n3,0,0,d1,d2,L,L1);
    eparzyn(n3+1)=functf(z1,-n3,0,0,d1,d2,L,L1);
    eparzz(n3+1)=functf(z1,n3,0,epm,d1,d2,L,L1);
    eparzzn(n3+1)=functf(z1,-n3,0,epm,d1,d2,L,L1);
end
```

```matlab
        exx=toeplitz(eparxx,eparxxn);
        exy=toeplitz(eparxy,eparxyn);
      exz=toeplitz(eparxz,eparxzn);
      eyx=toeplitz(eparyx,eparyxn);
       eyy=toeplitz(eparyy,eparyyn);
       eyz=toeplitz(eparyz,eparyzn);
      ezx=toeplitz(eparzx,eparzxn);
      ezy=toeplitz(eparzy,eparzyn);
      ezz=toeplitz(eparzz,eparzzn);
%*************** End Metal Permittivity ********************%
elseif   n <= Nd+Ng && n > Nd
% ********** Start Grating Permittivity **************%%%
        delta(n)=(d2-d1)/Ng;
      x3 = d1 - (d1 - d2)*(n - Nd)/Ng;
       x4 = d1 - (d1 - d2)*(n - 1 - Nd)/Ng;
       z2 = 0.5*(x3 + x4);
          for q3=0:2*N_t
    eparxx(q3+1)=functf(z2,q3,ECTF(1,1),epm,d1,d2,L,L1);
    eparxxn(q3+1)=functf(z2,-q3,ECTF(1,1),epm,d1,d2,L,L1);
     eparxy(q3+1)=functf(z2,q3,ECTF(1,2),0,d1,d2,L,L1);
    eparxyn(q3+1)=functf(z2,-q3,ECTF(1,2),0,d1,d2,L,L1);
     eparxz(q3+1)=functf(z2,q3,ECTF(1,3),0,d1,d2,L,L1);
    eparxzn(q3+1)=functf(z2,-q3,ECTF(1,3),0,d1,d2,L,L1);
     eparyx(q3+1)=functf(z2,q3,ECTF(2,1),0,d1,d2,L,L1);
    eparyxn(q3+1)=functf(z2,-q3,ECTF(2,1),0,d1,d2,L,L1);
    eparyy(q3+1)=functf(z2,q3,ECTF(2,2),epm,d1,d2,L,L1);
    eparyyn(q3+1)=functf(z2,-q3,ECTF(2,2),epm,d1,d2,L,L1);
     eparyz(q3+1)=functf(z2,q3,ECTF(2,3),0,d1,d2,L,L1);
    eparyzn(q3+1)=functf(z2,-q3,ECTF(2,3),0,d1,d2,L,L1);
     eparzx(q3+1)=functf(z2,q3,ECTF(3,1),0,d1,d2,L,L1);
    eparzxn(q3+1)=functf(z2,-q3,ECTF(3,1),0,d1,d2,L,L1);
    eparzy(q3+1)=functf(z2,q3,ECTF(3,2),0,d1,d2,L,L1);
    eparzyn(q3+1)=functf(z2,-q3,ECTF(3,2),0,d1,d2,L,L1);
    eparzz(q3+1)=functf(z2,q3,ECTF(3,3),epm,d1,d2,L,L1);
    eparzzn(q3+1)=functf(z2,-q3,ECTF(3,3),epm,d1,d2,L,L1);
end
exx=toeplitz(eparxx,eparxxn);
exy=toeplitz(eparxy,eparxyn);
exz=toeplitz(eparxz,eparxzn);
```

```matlab
eyx=toeplitz(eparyx,eparyxn);
eyy=toeplitz(eparyy,eparyyn);
eyz=toeplitz(eparyz,eparyzn);
ezx=toeplitz(eparzx,eparzxn);
ezy=toeplitz(eparzy,eparzyn);
ezz=toeplitz(eparzz,eparzzn);
    %%
%************* Permittivity for  CTF %%%%%%%%%%%%%%%%%%%%%%%%

  elseif  n <= Nd
              delta(n)=d1/Nd;
            x5 = (d1)*n/Nd;
          x6 = (d1)*(n- 1)/Nd;
          z3 = 0.5*(x5 + x6);
              for j1 =0:2*N_t
    eparxx(j1+1)=functf(z3,j1,ECTF(1,1),0,d1,d2,L,L1);
    eparxxn(j1+1)=functf(z3,-j1,ECTF(1,1),0,d1,d2,L,L1);
    eparxy(j1+1)=functf(z3,j1,ECTF(1,2),0,d1,d2,L,L1);
    eparxyn(j1+1)=functf(z3,-j1,ECTF(1,2),0,d1,d2,L,L1);
     eparxz(j1+1)=functf(z3,j1,ECTF(1,3),0,d1,d2,L,L1);
    eparxzn(j1+1)=functf(z3,-j1,ECTF(1,3),0,d1,d2,L,L1);
    eparyx(j1+1)=functf(z3,j1,ECTF(2,1),0,d1,d2,L,L1);
    eparyxn(j1+1)=functf(z3,-j1,ECTF(2,1),0,d1,d2,L,L1);
    eparyy(j1+1)=functf(z3,j1,ECTF(2,2),0,d1,d2,L,L1);
    eparyyn(j1+1)=functf(z3,-j1,ECTF(2,2),0,d1,d2,L,L1);
     eparyz(j1+1)=functf(z3,j1,ECTF(2,3),0,d1,d2,L,L1);
    eparyzn(j1+1)=functf(z3,-j1,ECTF(2,3),0,d1,d2,L,L1);
      eparzx(j1+1)=functf(z3,j1,ECTF(3,1),0,d1,d2,L,L1);
    eparzxn(j1+1)=functf(z3,-j1,ECTF(3,1),0,d1,d2,L,L1);
    eparzy(j1+1)=functf(z3,j1,ECTF(3,2),0,d1,d2,L,L1);
    eparzyn(j1+1)=functf(z3,-j1,ECTF(3,2),0,d1,d2,L,L1);
    eparzz(j1+1)=functf(z3,j1,ECTF(3,3),0,d1,d2,L,L1);
    eparzzn(j1+1)=functf(z3,-j1,ECTF(3,3),0,d1,d2,L,L1);
end
exx=toeplitz(eparxx,eparxxn);
exy=toeplitz(eparxy,eparxyn);
exz=toeplitz(eparxz,eparxzn);
eyx=toeplitz(eparyx,eparyxn);
eyy=toeplitz(eparyy,eparyyn);
```

```matlab
eyz=toeplitz(eparyz,eparyzn);
ezx=toeplitz(eparzx,eparzxn);
ezy=toeplitz(eparzy,eparzyn);
ezz=toeplitz(eparzz,eparzzn);
  end
%%
%*********   Calculating P Matrix  **************%
p_11=-kx*inv(ezz)*ezx;
 p_12=-kx*inv(ezz)*ezy;
 p_13=(ky/knot)*kx*inv(ezz);
 p_14=knot*eye(2*N_t+1)-(1/knot)*kx*inv(ezz)*kx;
 p_21=-ky*inv(ezz)*ezx;
 p_22=-ky*inv(ezz)*ezy;
 p_23=-knot*eye(2*N_t+1)+(ky^2/knot)*inv(ezz);
 p_24=-(ky/knot)*inv(ezz)*kx;
 p_31=-knot*eyx+knot*eyz*inv(ezz)*ezx-(ky/knot)*kx;
 p_32=(1/knot)*kx^2-knot*eyy+knot*eyz*inv(ezz)*ezy;
 p_33=-ky*eyz*inv(ezz);
 p_34=eyz*inv(ezz)*kx;
 p_41=knot*exx-knot*exz*inv(ezz)*ezx-(ky^2/knot)*eye(2*N_t+1);
 p_42=knot*exy-knot*exz*inv(ezz)*ezy+(ky/knot)*kx;
 p_43=ky*exz*inv(ezz);
 p_44=-exz*inv(ezz)*kx;
 p=[p_11 p_12 p_13 p_14; p_21 p_22 p_23 p_24; p_31 p_32 p_33 p_34;
    p_41 p_42 p_43 p_44];
%*********     End P Matrix      ******************%
%%
   [G1,D1] = eig(p);
        D2=diag(D1);
        D_imag=imag(D2);
        D_real=real(D2);
        [D3, sortindex3]=sort(D_imag,'descend');
        D_real1=D_real(sortindex3);
        D=D_real1+1i*D3;
        Dm=diag(D);
        Du{n}=diag(D(1:(4*N_t)+2));
        Dl{n}=diag(D((4*N_t)+3:(8*N_t)+4));
        G=G1(:,sortindex3);
            if  n==Ns+Nm
```

```matlab
                W=inv(G)*Z1;
            else
                W=inv(G)*Z;
                end
        wu{n}=W(1:4*N_t+2,1:4*N_t+2);
        wl{n}=W(4*N_t+3:8*N_t+4,1:4*N_t+2);
  Z=G*[eye(4*N_t+2);expm(-1i*delta(n)*Dl{n})*wl{n}*inv(wu{n})* expm
     (1i*delta(n)*Du{n})];
      matrix_zz{n} = [Z];
  end
    %%
% ***************** Finging T0 and R  for  Incidence Ap
    *******************%
Ap=zeros(4*N_t+2,1);
     Ap(3*N_t+2,1)=1;
     zu=Z(1:4*N_t+2, 1:4*N_t+2);
    zl=Z(4*N_t+3:8*N_t+4,1:4*N_t+2);
    f1=[zu  -yne; zl  -ynh];
    YP=[ype;yph];
    TR=inv(f1)*YP*Ap;
    T0=TR(1:4*N_t+2,1);
    R=TR(4*N_t+3:8*N_t+4,1);
    matrix_tt{1}=T0;
   %%
  T=T0;
   %******* calculating T matrix   *********************%
  for  nnn=1:Nd+Ng+Nm
      T=inv(wu{nnn})*expm(1i*delta(nnn)*Du{nnn})*T;
  matrix_tt{nnn+1}=T;
end
  %********************* End T Matrix   *****************%
    %%
    rs=R(1:2*N_t+1,1);
    rp=R(2*N_t+2:4*N_t+2,1);
    ts=T(1:2*N_t+1,1);
    tp=T(2*N_t+2:4*N_t+2,1);
   sumR=0;
    sumT=0;
    for  n1=1:2*N_t+1
```

```matlab
        kzr=real(kzn./(knot*cos(theta)));
        Rsp=(abs(rs(n1)')^2)*kzr(n1);
        Rpp=(abs(rp(n1)')^2)*kzr(n1);
        Tsp=(abs(ts(n1)')^2)*kzr(n1);
        Tpp=(abs(tp(n1)')^2)*kzr(n1);
        sumR=sumR+Rpp+Rsp;
        sumT=sumT+Tpp+Tsp;
     end
      App(vv)=1-(sumR+sumT);
     vv=vv+1;
end
if fr==1;
h1= plot(di:dt:df,   App, 'k','linewidth',4);
elseif fr==2;
h2= plot(di:dt:df,   App, '-.b','linewidth',4);
elseif fr==3;
h3= plot(di:dt:df,   App, '-.b','linewidth',4);
else
h4= plot(di:dt:df,   App, ':r','linewidth',4);
end
hold all

end
xlabel('\theta (deg)', 'FoN_tSize', 16);
 ylabel('A_{p}','FoN_tSize', 16);
 ax=gca;
 ax.FoN_tSize=16;
h = legend([h1,h2,h3,h4],{'L_{c}= 1000 nm','L_{c}= 2000 nm','L_{c}=
    3000 nm', 'L_{c}= 4000 nm'}, 'location' ,'north');
h.IN_terpreter = 'latex'
set(h,'IN_terpreter','latex')
legend show


function epsn_ctf= functf(z,n,epd,epm,d1,d2,L,L1)
CD=d2-d1;
y=(L1/pi)*asin((d2-z)/CD);
B=epm-epd;
 %% Permittivity for n=0
        if n == 0
```

```matlab
        if z<=d1
            epsn_ctf=epd;
        elseif z<d2 && z>d1
            epsn_ctf =(epd*(L - L1 + 2*y) +epm*(L1 - 2*y))/L;
        elseif z>=d2
        epsn_ctf=epm;
        end
    end
%% Permittivity for n~=0
    if n~= 0
        if z<d2 && z>d1
            epsn_ctf = (B*exp(-1i*n*(L1 - y)*2*pi/L) -B*exp(-1i*
                n*y*2*pi/L))* 1i/(n*2*pi);
        elseif z<=d1
            epsn_ctf =0;
        elseif z>=d2
            epsn_ctf =0;
        end
    end
    end
```

Bibliography

[1] J. Homola (editor), *Surface Plasmon Resonance Based Sensors*, Springer, Heidelberg, Germany (2006).

[2] I. Abdulhalim, "Surface plasmon TE and TM waves at the anisotropic film–metal interface," *J. Opt. A: Pure Appl. Opt.* **11**(1), 015002 (2009).

[3] J. A. Polo, Jr., T. G. Mackay, and A. Lakhtakia, *Electromagnetic Surface Waves: A Modern Perspective*, Elsevier, Waltham, Massachusetts, MA, USA (2013).

[4] S. A. Maier, *Plasmonics: Fundamentals and Applications*, Springer, New York, NY, USA (2007).

[5] S. J. Elston and J. R. Sambles, "Surface plasmon-polaritons on an anisotropic substrate," *J. Mod. Opt.* **37**(12), 1895–1902 (1990).

[6] M. Faryad, J. A. Polo, Jr., and A. Lakhtakia, "Multiple trains of same-color surface plasmon-polaritons guided by the planar interface of a metal and a sculptured nematic thin film. Part IV: Canonical problem," *J. Nanophoton.* **4**(1), 043505 (2010).

[7] F. Chiadini and A. Lakhtakia, "Gaussian model for refractive indexes of columnar thin films and Bragg multilayers," *Opt. Commun.* **231**(1-6), 257–261 (2004).

[8] M. W. Horn, M. D. Pickett, R. Messier, and A. Lakhtakia, "Blending of nanoscale and microscale in uniform large-area sculptured thin-film architectures," *Nanotech.* **15**(3), 303–310 (2004).

[9] E. D. Walsby, E. D. Walsby, M. Arnold, Q.-h. Wu, I. J. Hodgkinson, and R. J. Blaikie, "Growth and characterisation of birefringent films on textured silicon substrates," *Microelectron. Eng.* **78-79**, 436–441 (2005).

[10] C. Patzig, C. Patzig, B. Rauschenbach, B. Fuhrmann, and H. S. Leipner, "Growth of Si nanorods in honeycomb and hexagonal-closed-packed arrays using glancing angle deposition," *J. Appl. Phys.* **103**(2), 024313 (2008).

[11] R. J. Martín-Palma, R. J. Martín-Palma, M. Manso-Silván, A. Lakhtakia, and C. G. Pantano, "Ordered arrays of nanocolumns grown by the oblique angle deposition technique on a self-assembled layer of polystyrene spheres," *Mater. Lett.* **63**(2), 197–199 (2009).

[12] J. A. Polo, Jr., S. R. Nelatury, and A. Lakhtakia, "Propagation of surface waves at the planar interface of a columnar thin film and an isotropic substrate," *J. Nanophoton.* **1**(1), 013501 (2007).

[13] F. Chiadini, V. Fiumara, A. Scaglione, and A. Lakhtakia, "Multiple excitations of a surface-plasmon-polariton wave guided by a columnar thin film deposited on a metal grating," *Opt. Eng.* **53**(12), 127106 (2014).

[14] E. N. Glytsis and T. K. Gaylord, "Rigorous three-dimensional coupled-wave diffraction analysis of single and cascaded anisotropic gratings," *J. Opt. Soc. Am. A* **4**(11), 2061–2080 (1987).

[15] E. N. Glytsis and T. K. Gaylord, "Three-dimensional (vector) rigorous coupled-wave analysis of anisotropic grating diffraction," *J. Opt. Soc. Am. A* **7**(8), 1399–1420 (1990).

[16] A. M. Shrivastav, U. Cvelbar, and I. Abdulhalim, "A comprehensive review on plasmonic-based biosensors used in viral diagnostics," *Commun. Biol.* **4**(1), 70 (2021).

[17] S. S. Jamaian and T. G. Mackay, "On columnar thin films as platforms for surface-plasmonic-polaritonic optical sensing: higher-order considerations," *Opt. Commun.* **285**(24), 5535–5542 (2012).

[18] S. E. Swiontek, M. Faryad, and A. Lakhtakia, "Surface plasmonic polaritonic sensor using a dielectric columnar thin film," *J. Nanophoton.* **8**(1), 083986 (2014).

[19] H. Maab, M. Faryad, and A. Lakhtakia,"Surface electromagnetic waves supported by the interface of two semi-infinite rugate filters with sinusoidal refractive-index profiles," *J. Opt. Soc. Am. B* **28**(5), 1204–1212 (2011).

[20] T. G. Mackay, C. Zhou, and A. Lakhtakia, "High-phase-speed Dyakonov surface waves," *J. Nanophoton.* **15**(1), 010501 (2021).

[21] K. Uller, *Beiträge zur Theorie der Elektromagnetischen Strahlung*, Ph.D. thesis, Universität Rostock, Chap. XIV, (1903)

[22] J. Zenneck, "Über die Fortpflanzung ebener elektromagnetischer Wellen längs einer ebenen Lieterfläche und ihre Beziehung zur drahtlosen Telegraphie," *Ann. Phys. Lpz.* **23**(10), 846–866 (1907).

[23] A. Otto, "Excitation of nonradiative surface plasma waves in silver by the method of frustrated total reflection," *Z. Phys.* **216**(4), 398–410 (1968).

[24] E. Kretschmann and H. Raether, "Radiative decay of nonradiative surface plasmons excited by light," *Z. Naturforsch. A* **23**(12), 2135–2136 (1968).

[25] G. I. Stegeman, R. F. Wallis, and A. A. Maradudin, "Excitation of surface polaritons by end-fire coupling," *Opt. Lett.* **8**(7), 386–389 (1983).

[26] G. Ruffato and F. Romanato, "Grating-coupled surface plasmon resonance in conical mounting with polarization modulation," *Opt. Lett.* **37**(13), 2718–2720 (2012).

[27] L. Liu, M. Faryad, A. S. Hall, G. D. Barber, S. Erten, T. E. Mallouk, A. Lakhtakia, and T. S. Mayer, "Experimental excitation of multiple surface-plasmon-polariton waves and waveguide modes in a one-dimensional photonic crystal atop a two-dimensional metal grating," *J. Nanophoton.* **9**(1), 093593 (2015).

[28] C. J. Bouwkamp, and T. S. Mayer, "On Sommerfeld's surface wave," *Phys. Rev.* **80**(2), 294 (1950).

[29] A.D. Boardman (editor), *Electromagnetic Surface Modes*, Wiley, New York, NY, USA, (1982).

[30] M. G. Blaber, M. D. Arnold, and M. J. Ford, and T. S. Mayer, "Designing materials for plasmonic systems: the alkali–noble intermetallics," *J. Phys.: Condens. Matter* **22**(9), 095501 (2010).

[31] P. R. West, S. Ishii, G. V. Naik, N. K. Emani, V. M. Shalaev, and A. Boltasseva, "Searching for better plasmonic materials," *Laser Photon. Rev.* **4**(6), 795–808 (2010).

[32] R. H. Ritchie, "Plasma losses by fast electrons in thin films," *Phys. Rev.* **106**(5), 874–881 (1957).

[33] J. J. Hopfield, "Theory of the contribution of excitons to the complex dielectric constant of crystals," *Phys. Rev.* **112**(5), 1555 (1958).

[34] R. A. Depine and M. L. Gigli, "Excitation of surface plasmons and total absorption of light at the flat boundary between a metal and a uniaxial crystal," *Opt. Lett.* **20**(21), 2243–2245 (1995).

[35] H. Wang, "Excitation of surface plasmon oscillations at an interface between anisotropic dielectric and metallic media," *Opt. Mater.* **4**(5), 651–656 (1995).

[36] R. A. Depine and M. L. Gigli, "Resonant excitation of surface modes at a single flat uniaxial–metal interface," *J. Opt. Soc. Am. A* **14**(2), 510–519 (1997).

[37] J. A. Polo, Jr. and A. Lakhtakia, "On the surface plasmon polariton wave at the planar interface of a metal and a chiral sculptured thin film," *Proc. R. Soc. Lond. A* **465**(2101), 87–107 (2009).

[38] J. A. Polo, Jr. and A. Lakhtakia, "Energy flux in a surface-plasmon-polariton wave bound to the planar interface of a metal and a structurally chiral material," *J. Opt. Soc. Am. A* **26**(7), 1696–1703 (2009).

[39] G. J. Sprokel, R. Santo, and J. D. Swalen, "Determination of the surface tilt angle by attenuated total reflection," *Mol. Cryst. Liq. Cryst.* **68**(1), 29–38 (1981).

[40] G. J. Sprokel, "The reflectivity of a liquid crystal cell in a surface plasmon experiment," *Mol. Cryst. Liq. Cryst.* **68**(1), 39–45 (1981).

[41] J. A. Polo, Jr. and A. Lakhtakia, "Surface electromagnetic waves: A review," *Laser Photon. Rev.* **5**(2), 234–246 (2011).

[42] M. Faryad and A. Lakhtakia, "Grating-coupled excitation of multiple surface plasmon-polariton waves," *Phy. Rev. A* **84**(3), 033852 (2011).

[43] M. I. D'yakonov, "New type of electromagnetic wave propagating at an interface," *Sov. Phys. JETP* **67**(4), 714–716 (1988).

[44] O. Takayama, L.-C. Crasovan, S. K. Johansen, D. Mihalache, D. Artigas, and L. Torner, "Dyakonov surface waves: a review," *Electromagnetics* **28**(3), 126–145 (2008).

[45] A. N. Furs, V. M. Galynsky, and L. M. Barkovsky, "Surface polaritons in symmetry planes of biaxial crystals," *J. Phys. A: Math. Gen.* **38**(37), 8083–8101 (2005).

[46] N. S. Averkiev and M. I. Dyakonov, "Electromagnetic waves localized at the interface of transparent anisotropic media," *Opt. Spectrosc. (USSR)* **68**(5), 653–655(1990).

[47] J. A. Polo Jr., S. Nelatury, and A. Lakhtakia, "Surface electromagnetic wave at a tilted uniaxial bicrystalline interface," *Electromagnetics* **26**(8), 629–642 (2006).

[48] S. R. Nelatury, J. A. Polo Jr., and A. Lakhtakia, "Surface waves with simple exponential transverse decay at a biaxial bicrystalline interface," *J. Opt. Soc. Am. A* **24**(3), 856–865 (2007); Errata: **24**(7), 2102 (2007).

[49] A. N. Furs and L. M. Barkovsky, "Surface polaritons at the planar interface of twinned dielectric gyrotropic media," *Electromagnetics* **28**(3), 146–161 (2008).

[50] O. Takayama, L. Crasovan, D. Artigas, and L. Torner, "Observation of Dyakonov surface waves," *Phys. Rev. Lett.* **102**(4), 043903 (2009).

[51] O. Takayama, D. Artigas, and L. Torner, "Lossless directional guiding of light in dielectric nanosheets using Dyakonov surface waves," *Nature Nanotechnol.* **9**(6), 419–424 (2014).

[52] S. R. Nelatury, J. A. Polo, Jr., and A. Lakhtakia, "On widening the angular existence domain for Dyakonov surface waves using the Pockels effect," *Microwave Opt. Technol. Lett.* **50**(9), 2360–2362 (2008).

[53] C. J. Zapata-Rodríguez, J. J. Miret, J. A. Sorni, and S. Vuković, "Propagation of Dyakonon wave-packets at the boundary of metallodielectric lattices," *IEEE J. Sel. Top. Quantum Electron.* **19**(3), 4601408 (2013).

[54] T. G. Mackay and A. Lakhtakia, "Temperature–mediated transition from Dyakonov surface waves to surface–plasmon–polariton waves," *IEEE Photon. J.* **8**(5), 1–13 (2016).

[55] M. Faryad and F. Abbas, "On the Dyakonov waves guided by the interface with a columnar thin film," *12th International Congress on Artificial Materials for Novel Wave Phenomena–Metamaterials*, Espoo, Finland, Aug. 27–Sept. 1 (2018).

[56] J. A. Sorni, M. Naserpour, C. J. Zapata-Rodríguez, and J. J. Miret, "Dyakonov surface waves in lossy metamaterials," *Opt. Commun.* **355**, 251–255 (2015).

[57] F. Tian, D. Guo, B. Liu, Q. Zhang, Q. Tian, R. Ullah, and X. Xin, "A novel concatenated coded modulation based on GFDM for access optical networks," *IEEE Photonics J.* **10**(2), 1–8 (2018).

[58] T. G. Mackay and A. Lakhtakia, "Simultaneous existence of amplified and attenuated Dyakonov surface waves," *Opt. Commun.* **427**(1), 175–179 (2018).

[59] L.-C. Crasovan, D. Artigas, D. Mihalache, and L. Torner, "Optical Dyakonov surface waves at magnetic interfaces," *Opt. Lett.* **30**(22), 3075–3077 (2005).

[60] L.-C. Crasovan, O. Takayama, D. Artigas, S. K. Johansen, D. Mihalache, and L. Torner, "Enhanced localization of Dyakonov-like surface waves in left-handed materials," *Phys. Rev. B* **74**(15), 155120 (2006).

[61] D. Artigas and L. Torner, "Dyakonov surface waves in photonic metamaterials," *Phys. Rev. Lett.* **94**(1), 013901 (2005).

[62] O. Takayama et al., "Dyakonov surface wave resonant transmission," *Opt. Exp.* **19**(7), 6339–6347 (2011).

[63] O. Takayama, D. Artigas, and L. Torner, "Practical dyakonons," *Opt. Lett.* **37**(20), 4311–4313 (2012).

[64] L. Torner et al., "Nonlinear hybrid waves guided by birefringent interfaces," *Electron. Lett.* **29**(13), 1186–1188 (1993).

[65] L. Torner, J. P. Torres, and D. Mihalache, "New type of guided waves in birefringent media," *IEEE Photon. Technol. Lett.* **5**(2), 201–203 (1993).

[66] L. Torner et al., "Hybrid waves guided by ultrathin films," *J. Lightwave Technol.* **13**(10), 2027–2033 (1995).

[67] S. Pancharatnam, "The propagation of light in absorbing biaxial crystals—I. Theoretical," *Proc. Ind. Natl Sci. Acad.* **42**(2), 86–109 (1955).

[68] J. Gerardin and A. Lakhtakia, "Conditions for Voigt wave propagation in linear, homogeneous, dielectric mediums," *Optik* **112**(10), 493–495 (2001).

[69] T. G. Mackay, C. Zhou, and A. Lakhtakia, "Dyakonov–Voigt surface waves," *Proc. R. Soc. A* **475**(2228), 20190317 (2019).

[70] C. Zhou, T. G. Mackay, and A. Lakhtakia, "Singular existence of a Dyakonov–Voigt surface wave: Proof," *Results Phys.* **24**, 104140 (2021).

[71] P. Yeh, A. Yariv, and C.-S. Hong, "Electromagnetic propagation in periodic stratified media. I. General theory," *J. Opt. Soc. Am.* **67**(4), 423–438 (1977).

[72] P. Yeh, A. Yariv, and A. Y. Cho, "Optical surface waves in periodic layered media," *Appl. Phys. Lett.* **32**(2), 104–105 (1978).

[73] W. M. Robertson and M. S. May, "Surface electromagnetic wave excitation on one-dimensional photonic band-gap arrays," *Appl. Phys. Lett.* **74**(13), 1800–1802 (1999).

[74] V. N. Konopsky and E. V. Alieva, "Photonic crystal surface waves for optical biosensors," *Anal. Chem.* **79**(12), 4729–4735 (2007).

[75] D. P. Pulsifer, M. Faryad, and A. Lakhtakia, "Grating-coupled excitation of Tamm waves," *J. Opt. Soc. Am. B* **29**(9), 2260–2269 (2012).

[76] J. Martorell, D. W. L. Sprung, and G. V. Morozov, "Surface TE waves on 1D photonic crystals," *J. Opt. A: Pure Appl. Opt.* **8**(8), 630 (2006).

[77] F. Villa-Villa, J. A. Gaspar-Armenta, and A. Mendoza-Suárez, "Surface modes in one dimensional photonic crystals that include left handed materials," *J. Electromagn. Waves Appl.* **21**(4), 485–499 (2007).

[78] A. Lakhtakia and J. A. Polo, Jr., "Dyakonov-Tamm wave at the planar interface of a chiral sculptured thin film and an isotropic dielectric material," *J. Eur. Opt. Soc.–Rapid Pub.* **2**(1), 07021 (2007).

[79] K. Agarwal, J. A. Polo, Jr., and A. Lakhtakia, "Theory of Dyakonov–Tamm waves at the planar interface of a sculptured nematic thin film and an isotropic dielectric material," *J. Opt. A: Pure Appl. Opt.* **11**(7), 074003 (2009).

[80] J. Gao, A. Lakhtakia, and M. Lei, "On Dyakonov-Tamm waves localized to a central twist defect in a structurally chiral material," *J. Opt. Soc. Am. B* **26**(12), B74–B82 (2009).

[81] J. Gao, A. Lakhtakia, and M. Lei, "Synoptic view of Dyakonov-Tamm waves localized to the planar interface of two chiral sculptured thin films," *J. Nanophoton.* **5**(1), 051502 (2011).

[82] M. Faryad and A. Lakhtakia, "Propagation of surface waves and waveguide modes guided by a dielectric slab inserted in a sculptured nematic thin film," *Phys. Rev. A* **83**(1), 013814 (2011).

[83] M. Faryad and A. Lakhtakia, "Dyakonov–Tamm waves guided by a phase–twist combination defect in a sculptured nematic thin film," *Opt. Commun.* **284**(1), 160–168 (2011).

[84] D. M. Mattox, *The Foundations of Vacuum Coating Technology*, Noyes Publications, Norwich, NY, USA (2003).

[85] A. Lakhtakia and J. B. Geddes III, *Thin-Film Metamaterials Called Sculptured Thin Films*, Trends in Nanophysics, Springer, Heidelberg, Germany, (2010).

[86] I. J. Hodgkinson, Q. h. Wu, and J. Hazel, "Empirical equations for the principal refractive indices and column angle of obliquely deposited films of tantalum oxide, titanium oxide, and zirconium oxide," *Appl. Opt.* **37**(13), 2653–2659 (1998).

[87] L. Wei, P. Parhi, E. A. Vogler, T. M. Ritty, and A. Lakhtakia, "Thickness-controlled hydrophobicity of fibrous Parylene-C films," *Mater. Lett.* **64**(9), 1063–1065 (2010).

[88] V. C. Venugopal, A. Lakhtakia, R. Messier, and J.-P. Kucera, "Low-permittivity nanocomposite materials using sculptured thin film technology," *J. Vac. Sci. Technol. B* **18**(1), 32–36 (2000).

[89] T. G. Mackay and A. Lakhtakia, "Modeling columnar thin films as platforms for surface-plasmonic-polaritonic optical sensing," *Photonics Nanostructures—Fundam. Appl.* **8**(3), 140–149 (2010).

[90] A. Lakhtakia and R. Messier, *Sculptured Thin Films: Nanoengineered Morphology and Optics*, SPIE Press, Bellingham, WA, USA, (2005).

[91] I. J. Hodgkinson and Q.-h. Wu, *Birefringent Thin Films and Polarizing Elements*, World Scientific, Singapore (1997).

[92] T. Turbadar, "Complete absorption of light by thin metal films," *Proc. Phys. Soc.* **73**(1), 40 (1959).

[93] T. Turbadar, "Complete absorption of plane polarized light by thin metallic films," *Opt. Acta* **11**(3), 207–210 (1964).

[94] J. Fahrenfort, "Attenuated total reflection: A new principle for the production of useful infra-red reflection spectra of organic compounds," *Spectrochim. Acta* **17**(7), 698–709 (1961).

[95] M. Faryad and A. Lakhtakia, "Prism-coupled excitation of Dyakonov–Tamm waves," *Opt. Commun.* **294**, 192–197 (2013).

[96] R. Kronig, "A collective description of electron interactions," *Phys. Rev.* **86**(5), 795 (1952).

[97] D. Maystre, editor, *Selected Papers on Diffraction Gratings*, SPIE Press, Bellingham, WA, USA (1993).

[98] P. T. Worthing and W. L. Barnes, "Efficient coupling of surface plasmon polaritons to radiation using a bi-grating," *Appl. Phys. Lett.* **79**(19), 3035–3037 (2001).

[99] W. L. Barnes, A. Dereux, and T. W. Ebbesen, "Surface plasmon subwavelength optics," *Nature* **424**(6950), 824–830 (2003).

[100] G. Flätgen, K. Krischer, and G. Ertl, "Spatio-temporal pattern formation during the reduction of peroxodisulfate in the bistable and oscillatory regime: a surface plasmon microscopy study," *J. Electroanal. Chem.* **409**(1-2), 183–194 (1996).

[101] A. W. Peterson, M. Halter, A. Tona, and A. L. Plant, "High resolution surface plasmon resonance imaging for single cells," *BMC Cell Biol.* **15**(1), 35 (2014).

[102] J. S. Sekhon and S. Verma, "Plasmonics: the future wave of communication," *Curr. Sci.* **101**(4), 484–488 (2011).

[103] R. Agrahari, A. Lakhtakia, and P. K. Jain, "Information transfer by near-infrared surface-plasmon-polariton waves on silver/silicon interfaces," *Sci. Rep.* **9**(1), 12095 (2019).

[104] F. Ahmad, T. H. Anderson, P. B. Monk, and A. Lakhtakia, "Efficiency enhancement of ultrathin CIGS solar cells by optimal bandgap grading," *Appl. Opt.* **58**(22), 6067–6078 (2019).

[105] X. D. Hoa, A. G. Kirk, and M. Tabrizian, "Towards integrated and sensitive surface plasmon resonance biosensors: a review of recent progress," *Biosens. Bioelectron.* **23**(2), 151–160 (2007).

[106] F. Romanato, K. H. Lee, H. K. Kang, G. Ruffato, and C. C. Wong, "Sensitivity enhancement in grating coupled surface plasmon resonance by azimuthal control," *Opt. Exp.* **17**(14), 12145–12154 (2009).

[107] F. Romanato, K. H. Lee, H. K. Kang, G. Ruffato, and C. C. Wong, "Phase-detection-sensitivity enhancement of grating-coupled surface plasmon resonance sensor with light incident at nonzero azimuth angle," *J. Nanophoton.* **6**(1), 063524 (2012).

[108] E. Yeatman and E. A. Ash, "Surface plasmon microscopy," *Electron. Lett.* **23**(20), 1091–1092 (1987).

[109] A. V. Zayats, I. I. Smolyaninov, and A. A. Maradudin, "Nano-optics of surface plasmon polaritons," *Phys. Rep.* **408**(3–4), 131–314 (2005).

[110] A. Drezet, D. Koller, A. Hohenau, A. Leitner, F. R. Aussenegg, and J. R. Krenn, "Surface plasmon polariton microscope with parabolic reflectors," *Opt. Lett.* **32**(16), 2414–2416 (2007).

[111] V. Kanda, P. Kitov, D. R. Budle, and M. T. McDermott, "Surface plasmon resonance imaging measurements of the inhibition of Shiga-like toxin by synthetic multivalent inhibitors," *Anal. Chem.* **77**(23), 7497–7504 (2005).

[112] S. A. Maier, M. L. Brongersma, P. G. Kik, S. Meltzer, A. A. G. Requicha, and H. A. Atwater, "Plasmonics— A route to nanoscale optical devices," *Adv. Mater.* **13**(19), 1501–1505 (2001).

[113] L. Berguiga, T. Roland, K. Monier, J. Elezgaray, and F. Argoul, "Amplitude and phase images of cellular structures with a scanning surface plasmon microscope," *Opt. Exp.* **19**(7), 6571–6586 (2011).

[114] G. Stabler, M. G. Somekh, and C. W. See, "High-resolution wide-field surface plasmon microscopy," *J. Microsc.* **214**(3), 328–333 (2004).

[115] S. P. Frisbie, C. F. Chesnutt, M. E. Holtz, A. Krishnan, L. Grave de Peralta, and A. A. Bernussi, "Image formation in wide-field microscopes based on leakage of surface plasmon-coupled fluorescence," *IEEE Photon. J.* **1**(2), 153–162 (2009).

[116] J. T. Kim, J. J. Ju, S. Park, M.-s. Kim, S. K. Park, and M.-H. Lee, "Chip-to-chip optical interconnect using gold long-range surface plasmon polariton waveguides," *Opt. Exp.* **16**(17), 13133–13138 (2008).

[117] K. F. MacDonald and N. I. Zheludev, "Active plasmonics: current status," *Laser Photon. Rev.* **4**(4), 562–567 (2010).

[118] R. J. Walters, R. V. A. van Loon, I. Brunets, J. Schmitz, and A. Polman, "A silicon-based electrical source of surface plasmon polaritons," *Nature Mater.* **9**(1), 21–25 (2010).

[119] P. Berini, "Long-range surface plasmon polaritons," *Adv. Opt. Photon.* **1**(3), 484–588 (2009).

[120] F. Flory, L. Escoubas, and G. Berginc, "Optical properties of nanostructured materials: a review," *J. Nanophoton.* **5**(1), 052502 (2011).

[121] D. Mihalache, "Recent trends in micro-and nanophotonics: A personal selection," *J. Optoelectron. Adv. Mater.* **13**(9), 1055–1066 (2011).

[122] J. A. Polo, Jr., and A. Lakhtakia, "Morphological effects on surface-plasmon-polariton waves at the planar interface of a metal and a columnar thin film," *Opt. Commun.* **281**(21), 5453–5457 (2008).

[123] A. Yu. Nikitin, D. Artigas, L. Torner, F. J. García-Vidal, and L. Martín-Moreno, "Polarization conversion spectroscopy of hybrid modes," *Opt. Lett.* **34**(24), 3911–3913 (2009).

[124] M. Born and E. Wolf, *Principles of Optics, 6th ed.*, Pergamon Press, New York, NY, USA (1980); Sec. 14.3.3.

[125] H. C. Chen, *Theory of Electromagnetic Waves: A Coordinate-Free Approach*, McGraw–Hill, New York, NY, USA (1983).

[126] M. Born and E. Wolf, *Principles of Optics, 6th ed.*, Pergamon Press, New York, NY, USA (1980); Sec. 14.3.3.

[127] M. Faryad, J. A. Polo, Jr., and A. Lakhtakia, "Multiple trains of same-color surface plasmon-polaritons guided by the planar interface of a metal and a sculptured nematic thin film. Part IV: Canonical problem," *J. Nanophoton.* **4**(1), 043505 (2010).

[128] H. Hochstadt, *Differential Equations: A Modern Approach*, Dover Press, New York, NY, USA (1975)

[129] F. Wang, M. W. Horn, and A. Lakhtakia, "Rigorous electromagnetic modeling of near-field phase-shifting contact lithography," *Microelectron. Eng* **71**(1), 34–53 (2004).

[130] T. G. Mackay, "On the identification of surface waves in numerical studies," *Plasmonics* **14**(1), 1–2 (2019).

[131] J. Dutta, S. A. Ramakrishna, and A. Lakhtakia, "Characteristics of surface plasmon-polariton waves excited on 2D periodically patterned columnar thin films of silver," *J. Opt. Soc. Am. A* **33**(9), 1697–1704 (2016).

[132] T. G. Mackay and A. Lakhtakia, "Nonreciprocal Dyakonov-wave propagation supported by topological insulators," *J. Opt. Soc. Am. B* **33** (6), 1266–1270 (2016).

[133] T. Khaleque and R. Magnusson, "Light management through guided-mode resonances in thin-film silicon solar cells," *J. Nanophoton.* **8**(1), 083995 (2014).

[134] D. G. Peterson and A. Yariv, "Interferometry and laser control with solid Fabry–Perot etalons," *Appl. Opt.* **5**(5), 985–992 (1966).

[135] K. Mujeeb, M. Faryad, J. V. Urbina, and A. Lakhtakia, "Effect of orientation on excitation of surface-plasmon-polariton waves guided by a columnar thin film deposited on a metal grating," *Opt. Eng.* **59**(5), 055103 (2019); errata: **59**(6), 069801 (2020).

[136] Y. Jaluria, *Computer Methods for Engineering*, Taylor & Francis, Washington, DC, USA (1996).

[137] M. Mrozowski, *Guided Electromagnetic Waves: Properties and Analysis*, Research Studies Press, (1997).

[138] O. Takayama, A. A. Bogdanov, and A. V. Lavrinenko, "Photonic surface waves on meta-material interfaces," *J. Phys.: Condens. Matter* **29**(46), 463001 (2017).

[139] J. A. Kong, *Electromagnetic Wave Theory*, Wiley-Interscience, (1990).

[140] A. Lakhtakia and T. G. Mackay, "From unexceptional to doubly exceptional surface waves," *J. Opt. Soc. Am. B* **37**(8), 2444–2451 (2020).

[141] C. Zhou, T. G. Mackay, and A. Lakhtakia, "Theory of Dyakonov–Tamm surface waves featuring Dyakonov–Tamm–Voigt surface waves," *Optik* **211**, 164575 (2020).

[142] J. M. Pitarke, V. M. Silkin, E. V. Chulkov, and P. M. Echenique,"Theory of surface plasmons and surface-plasmon polaritons," *Rep. Prog. Phys.* **70**(1), 1 (2006).

[143] R. F. Wallis, J. J. Brion, E. Burstein, and A. Hartstein, "Theory of surface polaritons in anisotropic dielectric media with application to surface magnetoplasmons in semiconductors," *Phys. Rev. B* **9**(8), 3424–3437 (1974).

[144] F. N. Marchevskiĭ, V. L. Strizhevskiĭ, and S. V. Strizhevskiĭ, "Singular electromagnetic waves in bounded anisotropic media," *Sov. Phys. Solid State* **26**(5), 911–912 (1984).

[145] Y. Li, J. Sun, Y. Wen, and J. Zhou, "Controllable selective coupling of Dyakonov surface waves at a liquid-crystal-based interface," *Phys. Rev. Appl.* **13**(2), 024024 (2020).

[146] O. Takayama, P. Dmitriev, E. Shkondin, O. Yermakov, M. Panah, K. Golenitskii, F. Jensen, A. Bogdanov, and A. Lavrinenko, "Experimental observation of Dyakonov plasmons in the mid-infrared," *Semiconductors* **52**(4), 442–446 (2018).

[147] K. Mujeeb, M. Faryad, A. Lakhtakia, and J. V. Urbina, "Theory of grating-coupled excitation of Dyakonov surface waves," *Opt. Eng.* **59**(7), 070503 (2020); errata: **60**(6), 069801 (2021).

[148] A. Hartstein, E. Burstein, J. J. Brion, and R. F. Wallis, "Surface polaritons on semi-infinite anisotropic media," *Surf. Sci.* **34**(1), 81–89 (1973).

[149] J. J. Brion, R. F. Wallis, A. Hartstein, and E. Burstein, "Interaction of surface magneto-plasmons and surface optical phonons in polar semiconductors," *Surf. Sci.* **34**(1), 73–80 (1973).

[150] O. Takayama, E, Shkondin, A. Bodganov, M. E. Aryaee Panah, K. Golenitskii, P. Dmitriev, T. Repän, R. Malureanu, P. Belov, F. Jensen, and A. V. Lavrinenko, "Midinfrared surface waves on a high aspect ratio nanotrench platform," *ACS Photonics* **4**(11), 2899–2907 (2017).

[151] T. G. Mackay and A. Lakhtakia, textitElectromagnetic Anisotropy and Bianisotropy, 2nd ed., World Scientific, (2020); Sec. 1.7.2.2.

[152] J. R. Wait, *Electromagnetic Waves in Stratified Media, 2nd ed.*, Pergamon, (1970).

[153] K. Uller, *Beiträge zur Theorie der Elektromagnetischen Strahlung Ph.D. Thesis, Universität Rostock*, Germany, (1903); Chapter XIV.

[154] M. Faryad and A. Lakhtakia, "Grating-coupled excitation of the Uller–Zenneck surface wave in the optical regime," *J. Opt. Soc. Am. B* **31**(7), 1706–1711 (2014).

[155] M. Faryad and A. Lakhtakia, "Observation of the Uller–Zenneck surface waves," *Opt. Lett.* **39**(17), 5204–5207 (2014).

[156] J. Dostálek, J. Homola, and M. Miler, "Rich information format surface plasmon resonance biosensor based on array of diffraction gratings," *Sensors Actuators B: Chem.* **107**(1), 155–161 (2005).

[157] D. W. Unfricht, S. L. Colpitts, S. M. Fernandez, and M. A. Lynes, "Grating-coupled surface plasmon resonance: A cell and protein microarray platform," *Proteomics* **5**(17), 4432–4442 (2005).

[158] F.-C. Chien, C.-Y. Lin, J.-N. Yih, K.-L. Lee, C.-W. Chang, P.-K. Wei, C.-C. Sun, and S.-J. Chen, "Coupled waveguide–surface plasmon resonance biosensor with subwavelength grating," *Biosens. Bioelectron.* **22**(11), 2737–2742 (2007).

[159] C. Thirstrup, W. Zong, M. Borre, H. Neff, H. C. Pedersen, and G. Holzhueter, "Diffractive optical coupling element for surface plasmon resonance sensors," *Sensors Actuators B: Chem.* **100**(3), 298–308 (2004).

[160] P. Adam, J. Dostálek, and J. Homola, "Multiple surface plasmon spectroscopy for study of biomolecular systems," *Sensors Actuators B: Chem.* **113**(2), 774–781 (2006).

[161] T. G. Mackay and A. Lakhtakia, "Determination of constitutive and morphological parameters of columnar thin films by inverse homogenization," *J. Nanophoton.* **4**(1), 041535 (2010).

[162] M. G. Moharam and T. K. Gaylord, "Rigorous coupled-wave analysis of metallic surface-relief gratings," *J. Opt. Soc. Am. A* **3**(11), 1780–1787 (1986).

[163] M. G. Moharam, E. B. Grann, D. A. Pommet, and T. K. Gaylord, "Formulation for stable and efficient implementation of the rigorous coupled-wave analysis of binary gratings," *J. Opt. Soc. Am. A* **12**(5), 1068–1076 (1995).

[164] M. F. Iskander, *Electromagnetic Fields and Waves, 2nd ed.* Waveland, Long Grove, IL, USA, (2013).

[165] L. Ward, *The Optical Constants of Bulk Materials and Films, 2nd ed.*, Institute of Physics, Bristol, United Kingdom, (2000).

[166] A. Lakhtakia, editor, *Selected Papers on Linear Optical Composite Materials*, SPIE Optical Engineering Press, Bellingham, WA, USA, (1996).

[167] T. G. Mackay and A. Lakhtakia, *Modern Analytical Electromagnetic Homogenization with Mathematica®*, IOP Publishing, Bristol, United Kingdom, (2020).

[168] M. A. Motyka and A. Lakhtakia, "Multiple trains of same-color surface plasmon-polaritons guided by the planar interface of a metal and a sculptured nematic thin film," *J. Nanophoton.* **2**(1), 021910 (2008).

[169] F. Hao and P. Nordlander, "Efficient dielectric function for FDTD simulation of the optical properties of silver and gold nanoparticles," *Chem. Phys. Lett.* **446**(1–3), 115–118 (2007).

[170] P. D. McAtee, S. T. S. Bukkapatnam, and A. Lakhtakia, "Artificial neural network to estimate the refractive index of a liquid infiltrating a chiral sculptured thin film," *J. Nanophoton.* **13**(4), 046006 (2019).

[171] A. W. Snyder and J. D. Love, *Optical Waveguide Theory*, Chapman and Hall, New York, NY, USA, (1983).

Turnitin Originality Report

Surface Waves Guided by Anisotropic Dielectric Materials in the Grating-Coupled
Configuration   by Kiran Mujeeb .

turnitin

From CL QAU (DRSML)

- Processed on 28-Jun-2022 09:44 PKT
- ID: 1864014078
- Word Count: 42789

Similarity Index
19%
Similarity by Source

Internet Sources:
    16%
Publications:
    12%
Student Papers:
    3%

sources:

1 3% match (Internet from 19-Dec-2021)
http://Ndl.ethernet.edu.et/bitstream/123456789/32110/1/John%20A.%20Polo.pdf

2 1% match (Internet from 13-May-2020)
https://www.spiedigitallibrary.org/journals/Journal-of-Nanophotonics/volume-5/issue-
01/053527/Multiple-trains-of-same-color-surface-plasmon-polaritons-guided-
by/10.1117/1.3663210.full

3 1% match (Internet from 24-Dec-2021)
https://sbasse.lums.edu.pk/sites/default/files/2020-
12/Muhammad%20Kamran_Final%20Thesis.pdf

4 1% match (student papers from 27-Jun-2020)
Submitted to Higher Education Commission Pakistan on 2020-06-27

5 1% match (publications)
John A. Polo, Tom G. Mackay, Akhlesh Lakhtakia. "Surface Waves", Elsevier BV, 2013

6 1% match (publications)
Muhammad Faryad, Akhlesh Lakhtakia. "Excitation of multiple surface-plasmon-polariton
waves using a compound surface-relief grating", Journal of Nanophotonics, 2012

7 < 1% match (Internet from 23-Nov-2021)
https://www.spiedigitallibrary.org/journals/optical-engineering/volume-59/issue-05?SSO=1

8 < 1% match (Internet from 26-Mar-2019)
https://www.spiedigitallibrary.org/journals/Journal-of-Nanophotonics/volume-8/issue-
01/083986/Surface-plasmonic-polaritonic-sensor-using-a-dielectric-columnar-thin-
film/10.1117/1.JNP.8.083986.full

9 < 1% match (Internet from 23-Sep-2019)
https://www.spiedigitallibrary.org/profile/Muhammad.Faryad-105636

10 < 1% match (Internet from 15-Nov-2021)
https://www.spiedigitallibrary.org/proceedings/Download?
SSO=1&fullDOI=10.1117%2F12.2022273&isResultClick=True

11 < 1% match (Internet from 18-Nov-2021)
https://www.spiedigitallibrary.org/proceedings/Download?
SSO=1&fullDOI=10.1117%2F12.2038632&isResultClick=True

12 < 1% match (Internet from 03-Mar-2022)
https://www.spiedigitallibrary.org/journals/optical-engineering/volume-57/issue-
5/057101/Optimization-approach-for-optical-absorption-in-three-dimensional-structures-
including/10.1117/1.OE.57.5.057101.full?SSO=1

13 < 1% match (Internet from 20-Nov-2021)
https://www.spiedigitallibrary.org/proceedings/Download?
SSO=1&fullDOI=10.1117%2F12.2062713&isResultClick=True

14 < 1% match (Internet from 15-Nov-2021)